

# Dual-Axis Tilting Quadrotor Aircraft

An investigation into the overactuatedness and control thereof



**Nicholas Von Klemperer**

Department of Electrical Engineering  
University of Cape Town  
Rondebosch, Cape Town  
South Africa

**January 2017**

MSc thesis submitted in fulfilment of the requirements for the degree of Masters of Science in the  
Department of Electrical Engineering at the University of Cape Town

*Keywords:* Non-linear, control, allocation, quadrotor, UAV



*”We’re gonna have a superconductor turned up full blast and pointed at you for the duration of this next test. I’ll be honest, we’re throwing science at the wall here to see what sticks. No idea what it’ll do.*

*Probably nothing. Best-case scenario, you might get some superpowers...”*

Cave Johnson -Founder & CEO of Aperture Science

# Declaration

I, Nicholas Von Klemperer, hereby:

1. grant the University of Cape Town free license to reproduce the above thesis in whole or in part, for the purpose of research only;
2. declare that:
  - (a) This thesis is my own unaided work, both in concept and execution, and apart from the normal guidance from my supervisor, I have received no assistance except as stated below:
  - (b) Neither the substance nor any part of the above thesis has been submitted in the past, or is being, or is to be submitted for a degree at this University or at any other university, except as stated below.
  - (c) Unless otherwise stated or cited, any and all illustrations or diagrams demonstrated in this work are my own productions.
  - (d) All the content used to compile this report and complete the investigation revolving around the whole project is collectively hosted on the following GIT repositories:
    - LATEXreport: <https://github.com/nickvonklemp/Masters-Report>
    - STM32F303 Projects: <https://github.com/nickvonklemp/Code>
    - Design Files & Blue Prints: <https://github.com/Design>
    - Hardware Schematics: <https://github.com/nickvonklemp/visio &>
    - EagleCad Schematics <https://github.com/nickvonklemp/Eagle>
    - MatLab Simulink Code: <https://github.com/nickvonklemp/Simulink>
    - Results & Simulation Data: <https://github.com/nickvonklemp/results>

---

Nicholas Von Klemperer  
Department of Electrical Engineering  
University of Cape Town  
Tuesday 24<sup>th</sup> January, 2017

# Abstract

## Dual-Axis Tilting Quadrotor Aircraft

Nicholas Von Klemperer

Tuesday 24<sup>th</sup> January, 2017

The aim of this project is to design, simulate and control a novel quadrotor platform which can articulate all 6 Degrees of Freedom by vectoring each propeller's directional thrust. To achieve this the structure of the air-frame must redirect those thrust vectors to any desired orientation. This means it has to transform its configuration during flight, redirecting lift actuators whilst still maintaining stable attitude & position control, despite of such relative motion. In view of this required articulation the proposal is to add 2 axes (degrees) of extra actuation to each propeller. As a result each lift propeller can then be pitched or rolled relative to the body frame. This adaptation, to what is an otherwise well covered and highly researched platform, produces an over-actuated control problem. Actuator control allocation in the context of aerospace platforms is the primary contribution of this paper, with novel elements of non-linear (*state-space*) attitude control and plant uncertainty compensation.

The structure of the dissertation first presents the design which the subsequent dynamics and control are derived with respect to. Following that, the kinematics associated with rigid bodies are derived. Any unique effects that could apply to the design like gyroscopic, inertial and aerodynamic responses are investigated and then incorporated into the dynamics. Position and attitude control algorithms are first derived, then simulated and compared based on the plant's dynamics (*which include discretionary effects on the system*). The relative performance of the controllers are evaluated but regular performance metrics for attitude and position control are ill-suited for such a system. Some time is spent discussing the consequence of this and how the controllers are actually evaluated. Finally the design is built and tested using readily available RC components and conclusions drawn on the success or failure of the design.

The purpose of the investigation is the practicality and feasibility of such a design, most importantly whether the complexity of the mechanical design is a decent compromise for the added degrees of control actuation. The outcome of the build is to ascertain if it's economically feasible (cost and controller effort) to use such a prototype to expand the range of a quadrotor's motion. The design and control treatment presented here are by no means optimal nor the most exhaustive solutions, focus is placed on the system as a whole and not just one aspect of it.

*This dissertation report is presented in a logical progression of concepts and information. In some cases the research and results were completed in a different order from how they're listed here...*

# Acknowledgements

# Nomenclature

In order of appearance:

DOF - Degree of Freedom(s)

$\mu$ C - micro-controller

UAV - Unmanned aerial vehicle

SISO - Single input single output, control loop

MEMS - Micro-electromechanical system

DIY - Do it yourself

VTOL - Vertical takeoff/landing

IMU - Inertial measurement unit

BLDC - Brushless direct current, motor type

KV - Kilo-volt, BLDC motor rating

$\mu$ C - Micro-controller shorthand

PWM - Pulse width modulation

CH - Channel, radio control & PWM signals typically

RC - Radio control

OAT - Opposed active tilting

dOAT - Dual axis opposed active tilting

PD - Proportional derivative, control law

PID - Proportional integral derivative, control law

IBC - Ideal backstepping control

ABC - Adaptive backstepping control

PSO - Particle swarm optimization, gradient free genetic algorithm

BEM - Blade element theory

ESC - Electronic speed controller

MPC - Model predictive control

LQR - Linear quadratic regulator

LCF - Lyupanov candidate function

ITAE - Integral time additive error

TSK - Takagi-Sugeno-kang

I/O - Input/Output

RPM - Revolution Per Minute

RPS - Revolution Per Second

W.R.T - With respect to

LCF - Lyupanov Candidate Function

*iff* - If and only if

P.D - Positive definite, NOT proportional derivative

S.T - such that

# Symbols

Propeller Rotational Speed:  $\Omega_i$  [rpm] for motors:  $i \in [1, 2, 3, 4]$

*Rotational speeds in [RPS] are used for Blade Element Theory Calculations in Chapter:3*

Net body torque:  $\mu \vec{\tau} = [\tau_\phi \ \tau_\theta \ \tau_\psi]^T \in \mathcal{F}^b$

Net body thrust:  $\mu \vec{T} = [T_x \ T_y \ T_z]^T \in \mathcal{F}^b$

Body Position:  $\vec{E} = [x \ y \ z]^T \in \mathcal{F}^I$

Euler Angles:  $\vec{\mathcal{E}} = [\phi \ \theta \ \psi]^T \in \mathcal{F}^{I,v1,b}$

Servo 1 Position:  $\lambda_i$  [rad]

Servo 2 Position:  $\alpha_i$  [rad]

Motor module actuator positions:  $[\Omega_i \ \lambda_i \ \alpha_i]^T \in \mathcal{F}^{M_i}$

Actuator matrix:  $u = [M_1 \ \dots \ M_4]^T \in \mathbb{U}^{12}$

Motor module displacement arm:  $\vec{L}_{arm} = 195.16$  [mm]

Euler Rates:  $\frac{d}{dt} \vec{\eta} = \dot{\vec{\eta}} = \Phi(\eta) \dot{\omega}_b = [\dot{\phi} \ \dot{\theta} \ \dot{\psi}]^T \in \mathcal{F}^{v1,v2,I}$

Angular Velocity:  $\omega = [p \ q \ r]^T \in \mathcal{F}^b$

Linear Velocity:  $\nu = [u \ v \ w]^T \in \mathcal{F}^b$

# Contents

<b>Declaration</b>	ii
<b>Abstract</b>	iii
<b>Acknowledgements</b>	iv
<b>Nomenclature</b>	v
<b>Symbols</b>	vi
<b>1 Introduction</b>	1
1.1 Foreword . . . . .	1
1.1.1 A Brief Background to the Study . . . . .	1
1.1.2 Research Questions & Hypotheses . . . . .	2
1.1.3 Significance of Study . . . . .	3
1.1.4 Scope and Limitations . . . . .	3
1.2 Literature Review . . . . .	6
1.2.1 Existing & Related Work . . . . .	6
1.2.2 Notable Quadrotor Control Implementations . . . . .	9
<b>2 Prototype Design</b>	13
2.1 Design . . . . .	13
2.1.1 Actuation Functionality . . . . .	14
2.2 Conventions Used . . . . .	16
2.2.1 Reference Frames Convention . . . . .	16
2.2.2 Motor Axis Layout . . . . .	19
2.3 Inertial Matrices & Masses . . . . .	21

2.4 Electronics . . . . .	26
2.4.1 Actuator Transfer Functions . . . . .	30
<b>3 Kinematics &amp; Dynamics</b>	<b>34</b>
3.1 Rigid Body Dynamics . . . . .	34
3.1.1 Lagrange Derivation . . . . .	34
3.1.2 Rotation Matrix Singularity . . . . .	37
3.1.3 Quaternion Dynamics . . . . .	38
3.1.4 Quaternion Unwinding . . . . .	39
3.2 Multibody Nonlinearities . . . . .	40
3.2.1 Relative Rotational Gyroscopic & Inertial Torques . . . . .	41
3.3 Aerodynamics . . . . .	43
3.3.1 Propeller Torque and Thrust . . . . .	44
3.3.2 Hinged Propeller Conning & Flapping . . . . .	49
3.3.3 Drag . . . . .	50
3.4 Consolidated Model . . . . .	51
<b>4 Controller Development</b>	<b>52</b>
4.1 Control Loop . . . . .	52
4.2 Control Plant Inputs . . . . .	53
4.3 Lyapunov Stability Theorem . . . . .	55
4.4 Attitude Control . . . . .	56
4.4.1 The Attitude Control Problem . . . . .	56
4.4.2 Linear Controllers . . . . .	56
4.4.3 Non-linear Controllers . . . . .	61
4.5 Position Control . . . . .	64
4.5.1 PD Controller . . . . .	65
4.5.2 Adaptive Backstepping Controller . . . . .	66
4.6 Controller Allocation . . . . .	68
4.6.1 Pseudo Inverse Allocator . . . . .	71
4.6.2 Weighted Pseudo Inverse Allocator . . . . .	71
4.6.3 Priority Norm Inverse Allocator . . . . .	71

<b>CONTENTS</b>	<b>ix</b>
4.6.4 Non-linear Plant Control Allocation . . . . .	71
4.6.5 Online Optimized Secondary Goal Allocator . . . . .	71
<b>5 Simulations &amp; Results</b>	<b>72</b>
5.1 Controller Tuning . . . . .	72
5.1.1 Partical Swarm Based Optimization . . . . .	72
5.1.2 Performance Metric . . . . .	72
5.1.3 Global & Local Minima . . . . .	72
5.1.4 Fmincon Differences . . . . .	72
5.2 Simulation Block . . . . .	72
5.3 State Estimation . . . . .	72
5.4 Optimized Controller Comparisons . . . . .	72
5.4.1 Allocator Performance . . . . .	72
5.4.2 Attitude Control Results . . . . .	72
5.4.3 Autopilot Outcome . . . . .	72
<b>6 Prototype Flight Results</b>	<b>73</b>
<b>7 Conclusion</b>	<b>74</b>
<b>A Expanded Equations</b>	<b>75</b>
A.1 Standard Quadrotor Dynamics . . . . .	75
A.2 Blade-Element Momentum Expansion . . . . .	77
A.3 Euler-Angles from Quaternions . . . . .	77
<b>B Design Bill of Materials</b>	<b>78</b>
B.1 Parts List . . . . .	78
B.2 F3 Deluxe Schematic Diagram . . . . .	83
<b>C System ID Test Data</b>	<b>84</b>
C.1 Thrust and Torque Test Data . . . . .	84
C.2 Cobra CM2208-200KV Thrust Data . . . . .	85
<b>D Inertias</b>	<b>86</b>

# List of Figures

1.1	Mechanical actuators . . . . .	5
1.2	General structure for opposed tilting platform . . . . .	6
1.3	DJI Inspire1 . . . . .	7
1.4	Tilt-rotor mechanisms . . . . .	8
1.5	Dual-axis tilt-rotor mechanism . . . . .	9
1.6	ArduCopter PI Euler angle attitude control loop . . . . .	10
2.1	Isometric view of the prototype design . . . . .	13
2.2	Tilting rotor design . . . . .	14
2.3	Difference between propeller and motor planes . . . . .	15
2.4	Motor module assembly . . . . .	15
2.5	Inertial and body reference frames . . . . .	16
2.6	Aligned motor frame axes . . . . .	19
2.7	Intermediate motor frames . . . . .	19
2.8	Body frame axes layout . . . . .	20
2.9	Inertial measurement references . . . . .	21
2.10	Body structure's center of mass . . . . .	22
2.11	Inertial center & mass center . . . . .	24
2.12	Hardware schematic diagram . . . . .	26
2.13	SPRacing F3 deluxe layout . . . . .	27
2.14	SBUS converter & 6CH receiver . . . . .	27
2.15	S.BUS data stream . . . . .	28
2.16	RPM sensor calibration plots . . . . .	29
2.17	BLDC electronic speed controllers . . . . .	29
2.18	Servo transfer function test rig . . . . .	30

2.19 Unloaded servo transfer characteristics . . . . .	31
2.20 Servo block diagram . . . . .	31
2.21 Inner ring servo characteristics . . . . .	32
2.22 Middle ring servo characteristics . . . . .	32
2.23 BLDC rpm speed calibration and transfer function rig . . . . .	33
2.24 BLDC motor characteristics . . . . .	33
3.1 Mechanical gimbal lock . . . . .	37
3.2 Torque response rig . . . . .	42
3.3 Torque responses for inner and middle rings . . . . .	43
3.4 Disc Actuator Propeller Planar Flow . . . . .	44
3.5 Blade element profile at radius r . . . . .	45
3.6 Power & thrust coefficients . . . . .	47
3.7 Static propeller tests . . . . .	48
3.8 Propeller blade flapping . . . . .	49
3.9 Propeller coning . . . . .	50
4.1 Generalized control loop with allocation . . . . .	53
4.2 Abstracted control block . . . . .	54
B.1 Bearing Bracket Inner Ring Assembly . . . . .	80
B.2 Servo Bracket Inner Ring Assembly . . . . .	80
B.3 Servo Bracket Middle Ring Assembly . . . . .	80
B.4 Bearing Holder Middle Ring Assembly . . . . .	80
B.5 Servo Mount Middle Ring Assembly . . . . .	80
B.6 Bearing Shaft Middle Ring Assembly . . . . .	80
B.7 Bearing Holder Damping Assembly . . . . .	81
B.8 Servo Mount Damping Assembly . . . . .	81
B.9 Servo Mount Damping Bracket . . . . .	81
B.10 Bearing Holder Damping Bracket . . . . .	81
B.11 Arm Mount Damping Bracket . . . . .	81
B.12 Frame Brackets . . . . .	81
B.13 F3 Deluxe Flight Controller Hardware Schematic . . . . .	83

C.1	Clockwise and counterclockwise rotation tests . . . . .	84
C.2	Official Test Results for Cobra Motors . . . . .	85

# List of Tables

1.1	A breakdown of common attitude controllers . . . . .	10
2.1	Analogue & digital timing signals . . . . .	15
B.1	Parts List . . . . .	78
B.2	3D Printed Parts . . . . .	79
B.3	Inner & Middle Ring Assemblies . . . . .	80
B.4	Damping Assemblies . . . . .	81
B.5	Laser Cut Damping Brackets . . . . .	81
B.6	Laser Cut Parts . . . . .	82

# Chapter 1

## Introduction

### 1.1 Foreword

#### 1.1.1 A Brief Background to the Study

A popular topic for current control and automation research is that of quadrotor UAVs. Attitude control of a quadrotor poses a unique 6-DOF control problem, to be solved with an under-actuated 4-DOF system. As a result the pitch,  $\phi$ , and roll,  $\theta$ , plants aren't directly controllable. The attitude plant is often simplified around a stable operating point. The trimmed operating region is always at the inertial frame's origin; resulting in a zero-set point tracking problem. The highly coupled non-linear dynamics of a rigid body's translational and angular motions arise from gyroscopic torques and Coriolis accelerations (Sec: 3.2.1). Such effects are mostly negligible around the origin, hence the origin trim point decouples the system's nonlinearities. The control system can therefore reduce<sup>1</sup> each state variable,  $\vec{x}_b = [x \ y \ z \ \phi \ \theta \ \psi]^T$ , to individual SISO plants.

As almost every recent quadrotor research paper mentions, the late interest in the platform is due to recent emergence in the availability of MEMS and low-cost microprocessor systems. These technical advancements accommodate onboard state estimation and control algorithm processes in real time. Developmental progress in quadrotors and, to a lesser extent UAVs in general, has led to rapidly growing enthusiast communities. For example; HobbyKing [45] is now a name synonymous with providing custom DIY hobbyist quadrotor assembly kits & frames, no longer just a retailer for prebuilt commercial products like DJI Phantom [29] or ParrotAR [1] drones.

The avenue for potential application of both fixed wing and VTOL UAVs is expansive; supporting civil [79], agricultural [84] and security [60] industries and not just recreational hobbyists. The quadrotor design provides a mechanically simple platform on which to test advanced aerospace control algorithms. Commercial drone usage in industry is already emerging as a prolific sector; especially in Southern Africa. Subsequently following the 8<sup>th</sup> amendment of civil aviation laws [87], commercial use of UAVs has been both legalized and regulated. Research into any non-trivial aspect of the field will therefore be extremely valuable to the field as a whole. Large scale quadrotor, hexrotor and even octocopter UAVs are popular intermediate choices for aerial cinematography and other high payload capacity applications. The cost of a commercial drone like the SteadiDrone Maverik [67] is significantly less than a chartered helicopter used to achieve the same panoramic aerial scenes or on-site inspections. One foreseeable issue which may hinder commercial drone progress in the agricultural and civil sectors is the consequential inertial effects from scaling up the aerial structures. When increasing the size of any vehicle, its performance is adversely affected if actuation rates aren't proportionately increased.

---

<sup>1</sup>Those simplifications are expanded in Appendix:A.1.

### 1.1.2 Research Questions & Hypotheses

The difficulty with quadrotor control is that fundamentally they're unstable and under-actuated<sup>2</sup>. A quadrotor has only four controllable inputs, namely each propeller's rotational speed,  $\Omega_{1,2,3,4}$ , which is then abstracted to a net virtual control input net torque,  $\mu\vec{\tau} = [\tau_\phi \tau_\theta \tau_\psi]^T$ , and a perpendicular heave thrust  $\mu\vec{T} = \sum_{i=1}^4 T(\Omega_i)$  in the  $\hat{Z}_b$  direction. Those four inputs have to effect both the translational X-Y-Z positions,  $\vec{\mathcal{E}} = [x \ y \ z]^T$ , and angular pitch, roll and yaw attitude rotations,  $\vec{\eta} = [\phi \ \theta \ \psi]^T$ . Pitch and roll torques,  $\tau_\phi$  &  $\tau_\theta$ , are induced from differential thrusts of each opposing propeller. Yaw torque,  $\tau_\psi$ , is dependent on net aerodynamic torque about the rotational axes of each propeller. Aerodynamic responses are highly non-linear (Sec:3.3.1) and fluctuating sources of control torques, as such the body's yaw control is depreciated. A result of the under-actuation is that the attitude control problem then becomes a zero set point problem, any other attempt to track attitude is ill-posed.

The aim of this dissertation is to implement attitude and position dynamic set point tracking on a quadrotor UAV by solving the problem of its inherent under-actuation. Inspired by Boeing/Bell Helicopter's V22 Osprey and the tilting articulation of its propellers, the prototype design proposed here (presented in Sec:2.1) introduces two additional actuators for each of the four quadrotor's lift propellers. Specifically, adding rotations about the  $\hat{X}$  and  $\hat{Y}$  axes for each motor/propeller pair. The resultant is an articulated 3-dimensional thrust vector instead of a bound perpendicular heave force. The control problem is then posed as the design and allocation of net forces,  $\vec{F}_{net} = [F_x \ F_y \ F_z]^T$ , and torques,  $\vec{\tau}_{net} = [\tau_\phi \ \tau_\theta \ \tau_\psi]^T$ , for a general 6-DOF body such that for any given trajectory,  $\mathbf{X}_d(t) = [x \ y \ z \ \psi \ \theta \ \phi]^T$ , the error state  $\mathbf{x}_e(t) = \mathbf{x}_d(t) - \mathbf{x}_b(t)$  asymptotically tends to  $\vec{0}$ .

$$\lim_{t \rightarrow \infty} \mathbf{x}_e(t) = \vec{0} \quad \forall \mathbf{x} \in \mathbb{R}^n \quad (1.1)$$

Where  $n$  is the degree of freedom the system has, typically a 6-DOF plant for rigid bodies. The over-actuation brings about the need for a control allocation scheme which distributes the 6 commanded system inputs (net torques and forces) among the actuator set (12 actuators) in order to optimize some objective function secondary to that of Eq:1.1. The potential improvement(s) for exploiting those over-actuated elements is the most novel outcome which the project could yield. A cost function aimed at optimizing some aspect unique to aerospace bodies is going to be a completely unique contribution.

Part of the control research question is the multivariable treatment of the system; making as few assumptions or simplifications as possible to the non-linear dynamics involved in the quadrotors motion and its operational conditions. Standard linearizations applied to the quadrotor's control plant won't hold true for the more aggressive manoeuvres; they're dependent on small angle approximations and negligible 2<sup>nd</sup> order effects. A stabilizing control law solution will need to expand and simulate the existing kinematic model of an aerial body and apply it to a quadrotor's motion. Following this there must be design, development and control of the new actuator suite which is to be implemented on a quadrotor platform. Final key outcomes for the project are the control paradigm, simulation analysis and prototype design for over-actuating the body and the conclusions drawn thereon.

Introducing relative motion within an unconstrained body will produce a lot of unwanted dynamics like inertial and gyroscopic responses, amongst others. A rotating propeller will respond to pitching much like a Control Moment Gyroscope [115] or a flywheel, producing a precipitation torque cross product. A less trivial aspect which is occasionally considered are the aerodynamic effects produced from the propeller's aerofoil profile. Such induced responses occur in planes perpendicular to whatever the propeller's rotation exists in. These aspects aren't normally compensated for due to a quadrotor's fundamental co-planar propeller counter-rotating pairs which negate such effects. It's self-evident that a plant dependent control solution will have to compensate for these dynamics, which if left unaccounted for would cause instability.

---

<sup>2</sup>Subsequently empirically proven using Layupanov Theorem in Chapter:4

### 1.1.3 Significance of Study

Owing to the huge popularity of quadrotor platforms as research tools, any work that expands the UAV & quadrotor general body of knowledge will prove to be valuable. With that being said, there is already a vast amount of existing research on linear and non-linear control techniques for regular quadrotor platforms. The attitude loop is the most common topic for control research, requiring an ingenious under-actuated solution and mostly linearized around the origin (Appendix:A.1). Far less common is the application of optimal flight path and trajectory planning to quadrotor control. The uniqueness and difficulty of the quadrotor attitude control does not hold true for its position control plant, so standard techniques can be used for way point planning and the like once the attitude control problem has been answered.

The most significant aspect of this project is the attitude control, discussed later in Sec:4.4. The over-actuation of the proposed design and, more critically, the manner in which the controller's commanded (virtual) output is distributed among those control effectors would, at the time of writing, appear to be the first of its kind. Otherwise known as control allocation, the requirements of the distribution algorithm(s) are outlined in Sec:4.6. Dynamic set point attitude control for aerospace bodies is not a subject heavily researched outside the field of satellite attitude control. Even papers which propose similarly complicated mechanical over-actuation (expanded upon in next in the literature review, Sec:1.2) hardly broach the topic of tracking attitude set points away from the origin.

Whilst the control plant (developed in Chapter:4) does indeed close both the position and attitude control loops, there is no consideration of trajectory generation nor flight path planning. Such topics are well discussed elsewhere in a far more concise and deliberate way than this project could ever hope to achieve. Once closed loop position and attitude control have been achieved, the control algorithms can be adjusted to account for higher order state derivative (acceleration, jerk and jounce) tracking needed for nodal way point planning. The heuristics involved with flight path planning are well documented and their implementation is a relatively academic task.

Where possible the system identification and control (design and allocation) for this project is kept both modular and generally applicable. The intention of which is that its pertinence falls not only within the UAV field but also to any aerospace or free body attitude control. Hopefully this investigation can be expanded upon with more in-depth research on one of the subsystems without compromising the stability of the whole plant. Provisionally, an obvious outcome which the investigation could yield is improved yaw control of a quadcopter's attitude. However, if the express purpose was just to improve yaw control, it could be done with a dramatically less complicated design...

Furthermore, the project could provide greater insight into high bandwidth actuation and thus a faster control response for larger aerospace bodies. Any standard quadrotor uses differential thrust to develop a torque about its body. Such actuation suffers a second order inertial response when the propellers accelerate or decelerate,  $\vec{\tau}_p = \mathbb{I}_p \dot{\Omega}_i$ . Prioritizing pitching the propeller's principle axis of rotation rather than changing the it's rotational speed could potentially improve the virtual control response. This is entirely dependent on how the allocator block is prioritized (presented in Sec:4.6). The exact effects of different actuator prioritization and distribution in the context of aerospace control are wholly unique to this research.

### 1.1.4 Scope and Limitations

#### Scope

Critical to this project is the conceptualized design and prototyping of a novel actuation suite to be used on a quadrotor platform. The precise requirement of which is to apply dynamic set point attitude control to the body. Stemming from this is an investigation into the kinematics that are

potentially influenced by the design *changes* and the structure's relative motion. In order to apply correct control theory to achieve the attitude tracking on the physical prototype, plant dynamics must first be identified for input responses to be approximated with confidence. Aspects of the mechanical design are covered next in Sec:2.1 but, beyond the cursory investigation, there is no scope for materials analysis or stress testing of the design. To the detriment of the project, the design will either produce an over-engineered or catastrophically under-engineered solution. The scope focuses mainly on the control application and embedded systems design, not the structural integrity of a proposed frame given the forces it may undergo. Physical measurements are only made for critical kinematics; such as inertial measurements for the second order gyroscopic and inertial dynamic responses.

As mentioned in the antecedent Sec:1.1.3; trajectory & flight path planning are not ubiquitous with this dissertation. Derivations for the differential equations which dictate a 6-DOF body's movement are wholly applicable to any dynamic (rigid or otherwise) aerospace body. Although some particular standards are used *sic* Z-Y-X Euler Aerospace rotational sequence, Sec:2.2. Similarly the control plant is stabilized with non-linear state space control techniques, aided and justified by Lyapunov Theorem. Alternative solutions using Model Predictive Control or Quantitative Feedback Theory could provide more refined or effective controllers, however they aren't presented and remain open to further investigation. Quadrotor attitude control is commonly stabilized with feedback linearizations, decoupling the plant around a trim point so that SISO techniques can be applied. A derivation of such a linearization is included in Appendix:A.1 but beyond that there are no further discussions. Any comparison between non-zero and zero-set point attitude controller efficacy for quadrotors is difficult as the fundamental objectives are in stark contrast with one another.

Arguably the most important and indeed novel aspect of this project is the control allocation. The system has 12 plant inputs and 6 output variables to be controlled. There is then a family of actuator set solutions,  $u \in \mathbb{U}$ , which exist for each commanded input. Such a plant is classified as over-actuated. Ergo, there must be some logical process as to how those 12 inputs are articulated to achieve the desired 6 control plant inputs. Appropriate techniques are first investigated in Sec:4.6 then simulated and compared before a final solution is implemented in Section:5.4. It is by no means a comprehensive investigation of every possible allocation scheme but rather an analysis of the sub-set of problems and design of what is regarded as a logical and pertinent approach.

With regards to the actual prototype design, in Sec:2.1, it's assumed that certain aspects are a given certainty. Particularly the state estimation, updated through a 4-camera positioning system fused with a 6-axis IMU through Kalman Filtering (Sec:5.3), is assumed to precise and readily disposable at a consistent 50 Hz. Hence state estimation is included but is bereft of intricate detail, this is another topic which remains open to further investigation.

## Limitations

The biggest constraint faced by the design is the net weight of the assembled frame. Lift thrusts which are required to keep the body aloft and oppose the net gravitational force are obviously dependent on the all up weight. Conventional wisdom has it that steady state actuator rates ought to be far less than saturation conditions. For stability to be guaranteed at all feasible operating conditions, the actuators must have sufficient headroom to still effect the desired control inputs. Conversely the structure's net weight is mostly dependent on the lift motors, often being the heaviest part of the vehicle (*batteries included*). A trade-off between net weight and actuator effectiveness makes designing the prototype a balancing act of compromise; added actuation is needed to produce the desired thrust vectoring. That added actuation is going to increase the weight which then requires more thrust force to ensure the vehicle remains airborne. Larger motors then need stronger actuators to effect the relative motion and overcome the bodies inertial response. It's a compromise between the weight of the body and the strength/quality of the actuation.

To forego the deliberation detailed above, reducing the possibility of unbounded scope creep, a limitation is self-imposed on the prototype design. Restricting the propeller diameter, and hence maximum thrust/frame size, will provide a constraint upon which all other design considerations must adhere to. Smaller propellers require far greater rotational speeds to produce similar levels of thrust that their larger diameter counterparts could provide. Electing to use 3 bladed 6X4.5 inch small diameter propellers is going to reduce the overall dimensions of the prototype, but as a consequence will require very high RPM motor. Specifically a set of four Cobra-2208/2000KV [26] brushless DC motors are to be used for lift actuation (Fig:1.1a)<sup>3</sup>. A direct consequence of this decision is that, provisionally based upon test data<sup>4</sup>, the net thrust disposable for actuation is limited to around  $950g \approx 9.5N$ , per motor at 14.1v (Sec:3.3.1). It's critical to ensure the control block doesn't induce over-saturation of the motor actuation, so the frame weight needs to be under 50% of the maximum available thrust, or roughly below 2 Kg. Saturation conditions are detailed later in Sec: 4.6.

Another aspect of limitations produced by design decisions made, mostly to reduce prototype costs and weight, is to use of  $180^\circ$  rotation servo motors. Here Corona DS-339MG metal gear digital servos (Fig:1.1b)<sup>5</sup> are used. The servos are for each individual motor's  $\hat{X}_{M_i}$  and  $\hat{Y}_{M_i}$  axial pitch and roll actuations respectively. The servos act in lieu of either continuous BLDC (gimbal) or stepper motors. Any non-servo rotations beyond  $2\pi$  will require closed loop position control and, unlike servos, would need slip rings to transmit power throughout rotational movement. However the logistics of implementing such a design whilst maintaining an acceptable weight is almost impossible. Such an implementation is going to dramatically increase the size of the prototype to accommodate for weight increases. Commercial camera stabilizing gimbals already make use of similar configurations but the I/O requirements from the flight controller  $\mu$ C already constricts the amount of expansion available.



(a) Cobra CM2208/2000KV BLDC motor

(b) Corona DS-339MG digital servo

**Figure 1.1:** Mechanical actuators

Discrete elements for the whole system could potentially limit performance but are mitigated where possible. For example analogue servos have an associated  $1ms$  dead time from their  $50Hz$  refresh rate. That can be addressed by using faster, albeit more expensive, digital servos which samples at  $330Hz$ . The prototype's flight controller needs to provide 12 PWM output compare channels for the 8 servos and 4 BLDC speed controllers. State updates from a ground control station and a fail safe 6CH RC receiver module also needs to be processed by the  $\mu$ C system. Particular attention is paid to the embedded system design and layout in Sec:2.4.

<sup>3</sup>Image cited from: <http://www.getfpv.com/cobra-cm-2208-2000kv-motor.html>

<sup>4</sup>Official test data from [26] included in Appendix:C.2 and verified independently through testing in Sec:3.3.1

<sup>5</sup>From the DS-339MG product page, HobbyKing [45]

## 1.2 Literature Review

### 1.2.1 Existing & Related Work

The field of transformable aerospace frames is not necessarily a new one, with many commercial examples having seen a lot of success over their operational life span. The most notable tilting-rotor vehicle is that of the Boeing/Bell V22 Osprey [34] aircraft. First introduced into the field in 2007, the Osprey has the ability to pitch its two lift propellers forward to aid translational flight after vertically taking off or landing. In addition to this there have been many papers published on similar tilting bi-rotor UAVs for research purposes.

#### Birotors

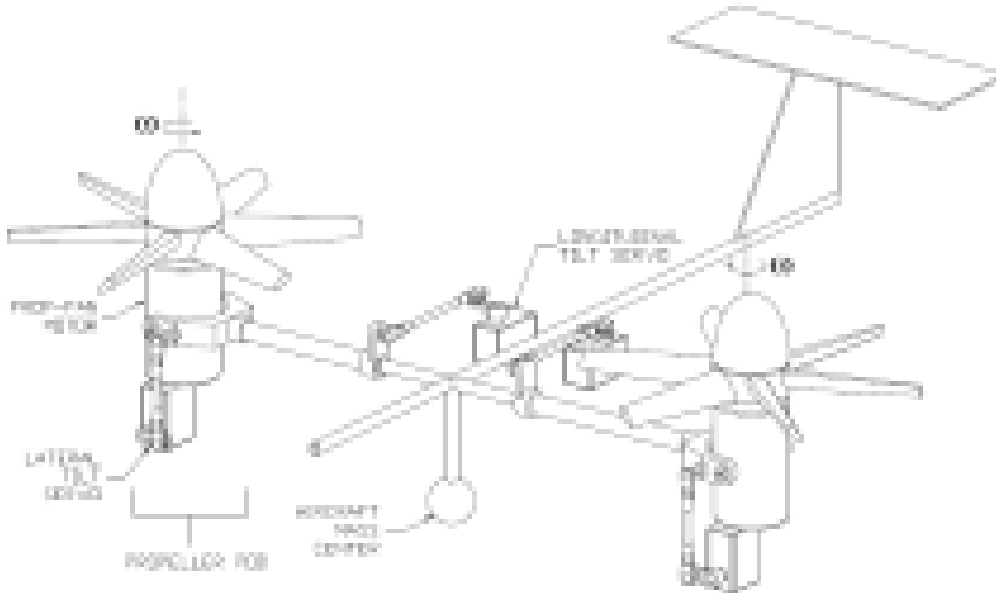


**Figure 1.2:** General structure for opposed tilting platform

Research into birotor vehicles (Fig:1.2)<sup>6</sup> with ancillary lift propeller actuation is oft termed *Opposed Active Tilting* or *OAT*. Such a rotorcraft's mechanical design applies either a single *oblique*  $45^\circ$  tilting axis relative to the body; [12, 38, 55], or a *lateral* tilting axis, adjacent to the body; [22, 57, 83, 98]. Leading research is currently focussed on applying doubly actuated tilting axes to birotor UAVs. *Dual axis Opposed Active Tilting* or *dOAT* introduces vectored thrust with propeller pitch and roll motions to further expand the actuation suite, [3, 37]. A birotor is sometimes considered preferable to higher order multirotor platforms due to their reduced controller effort. However the controller plant abstraction, typically requiring feedback linearization, often detracts from the quality and effectiveness of its stability solution as a result of the birotor's underactuation.

Birotor attitude control typically incorporates plant independent PD [12] and PID [83] controller schemes. Occasionally more computationally intensive and plant dependent Ideal and Adaptive backstepping controllers (*IBC* or *ABC*) are implemented, presented in [55, 98] and [57] respectively. The cross-coupling of a birotor vehicle's attitude system is more pronounced than that of a quadrotor, derived in Sec:3.2, and so feedback linearisation is almost always used. In an interesting progression from the norm, Lee et al. [2007] [62] proposed a PID co-efficient selection algorithm for a bi-rotor control block. Using a Particle Swarm Optimization technique, similar to [118], the coefficients were globally optimized around a given performance metric. However their performance criterion is a basic

<sup>6</sup>Image taken from G. Gress [2007] [37]

ITAE<sup>†</sup> term and nothing more appropriate involving effects unique to flight systems was used. PSO algorithms iteratively search for a globally optimized solution and offer independent, gradient free based optimization. Later on non-linear controller coefficient are also optimized in this paper using a PSO algorithm, shown in Sec:5.1.

## Quadruplets

Expanding on multirotor vehicles, the quadrotor UAV is a popular and well researched multirotor platform due to its mechanical simplicity. What would appear to be one of the first quadrotor research implementations, in 2002, is the X4-Flyer quadrotor [40,89]. Alternative iterations like the Microraptor [93] and STARMAC [46] quadcopters have subsequently been built and tested. A plethora of literature exists around quadrotor kinematics & control [5, 15, 25, 68, 92], however dedicated rigid body 6-DOF dynamic papers [70, 85] offer better explanations of the kinematics. Often the plant's dynamics are simplified around an origin trim point and assumed to reduce into 6 SISO plants for each degree of freedom (Appendix:A.1). Lately research projects have begun to incorporate non-linear aerodynamic effects like drag and propeller BEM theory into the plant model [19,46,95]. Although mostly negligible under standard operating conditions, the higher fidelity models offer more precision by making fewer linearisations and assumptions, [7,46].

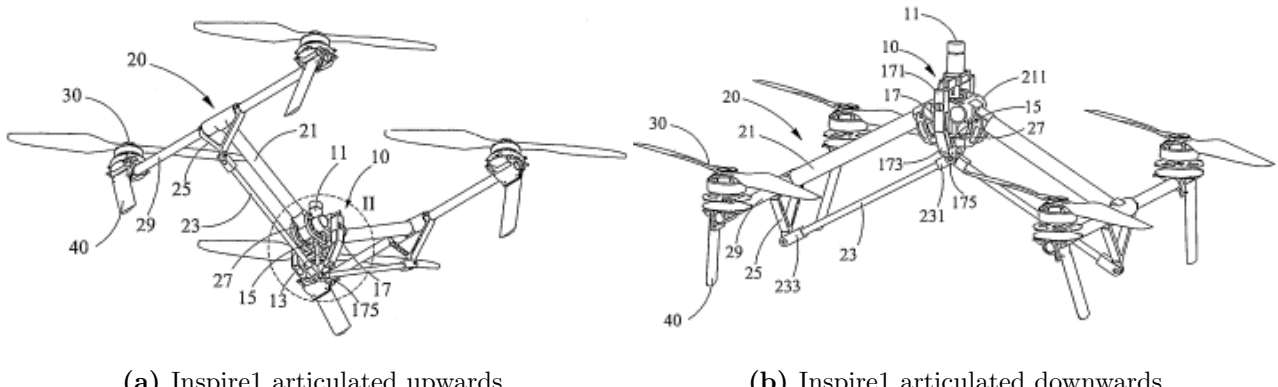


**Figure 1.3:** DJI Inspire1

At the time of writing, the only commercial UAV multirotor capable of structural transformation is the DJI Inspire1 quadrotor [28], manufactured by Shenzhen DJI Technologies (best known for their hugely successful DJI Phantom drone [29]). The Inspire1 can articulate its supporting arms up and down as shown in Fig:1.3<sup>7</sup>. The aim of such transformations is to both alter the center of gravity and to further expose a belly mounted camera gimbal for panoramic viewing angles. This change alters the moment of inertia about the body's center of gravity, in turn affecting the inertial torque response induced by angular velocities, an otherwise detrimental effect which makes researchers apprehensive of transformable aerospace frames. The range of transformations which the frame can undergo is limited to just articulating the arms up and down.

In a similar fashion to the progression seen in birotor state-of-the-art, quadrotor research is engaging the topics of single and dual axis tilting articulations. First conceptualized and implemented on a prototype related to an ongoing project covered in two reports, [96, 97]. The authors M. Ryll et al. [2012, 2013] modified and tested a QuadroXL four rotor helicopter, produced by MikroKopter [35], to actuate a single axis of tilting aligned with the frame's arms (Fig:1.4a)<sup>8</sup>. Their proposed control solution, detailed next in Sec:1.2.2, assumes no nominal linearised conditions around hover flight, unlike a similar single axis tilting quadrotor prototype designed by Nemati, et al. [2012] [76]. The latter remains simulated but as yet untested.

<sup>7</sup>Both images were sourced from the drone's patent; held by SZ DJI Tech Co [116]

<sup>8</sup>Image cited from Modelling and Control of a Quadrotor UAV with tilting propellers, [96]

One approach to improving quadrotor flight response is to alter the manner in which the thrust is mechanically actuated, potentially improving the actuator bandwidth. Drawing from helicopter design, a project by Napsholm, [2013] [75], purported a novel quadrotor UAV prototype that used swash-plates for varying the propeller pitch and generating torque moments. The aim was a design which wasn't dependent on rotational speed controlling power electronics (*ESCs*) to actuate variable thrust forces. Petrol motors were intended for use in place of BLDC motors. Furthermore, the design proposed a single axis of tilt actuation to each of the four motor modules. Whilst mechanically complex, Napsholm made use of existing off-the-shelf RC helicopter components to design a rotor actuation bracket (Fig:1.4b). The cyclic-pitch swashplate used [77] could apply torques,  $\tau_\phi$  and  $\tau_\theta$ , about each propeller's hub, its *principle axis of rotation*, by altering the blades angle of attack throughout the rotational cycle. The actuation rate of such a configuration is far greater than that of a differential torque produced rolling/pitching motion.

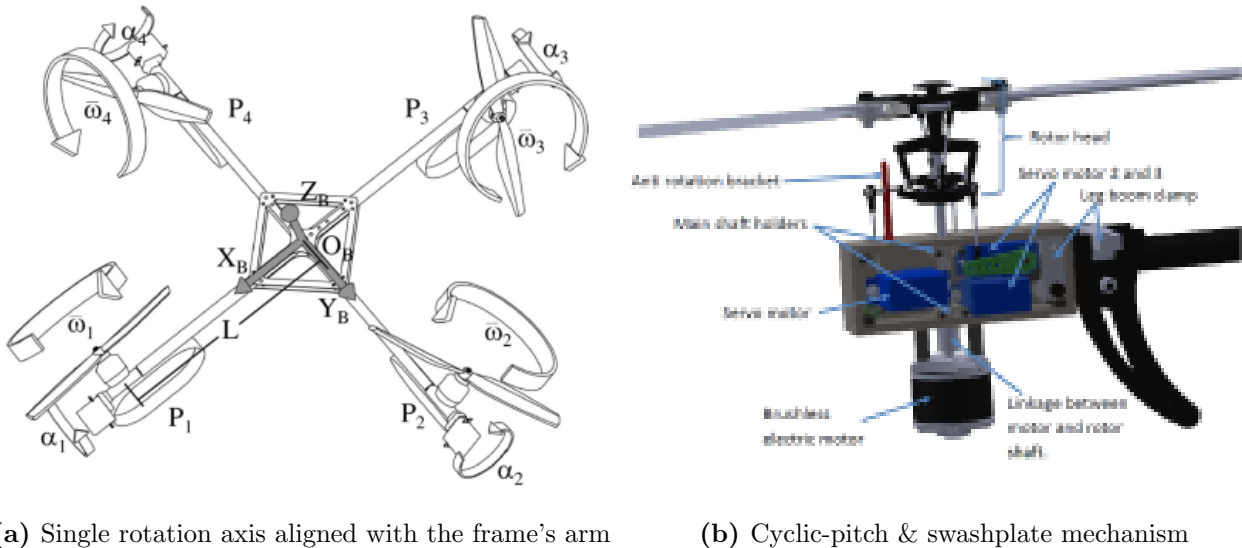


**Figure 1.4:** Tilt-rotor mechanisms

Irrespective of the strong initial design in the early stages of his project, it would appear that Napsholm's research suffered due to time constraints. The introductory derivation on aerodynamic effects and deliberation over the design provide clear insight into the projects goals. However the control solution and system architecture, electronic and software, are severely lacking. A brief introductory proposal of an MPC attitude control system detracted from the comprehensive dynamics discussed. The project ended before testing, simulation or results could be obtained. Unfortunately, despite the novel over-actuated design, there was no discussion given on how that actuator allocation, being the most unique aspect, would be achieved.

Finally, the most crucial research to mention is a project completed by Pau Segui Gasco [33], which was a dual presented MSc project with Yazan Al-Rihani [2]. At the time of writing, this would appear to be the only project published pertaining to *over-actuation* in aerospace bodies implemented on a quadrotor platform. The research was split between the two authors who completed the electronic/control design and the mechanical design for their respective MSc dissertations. Shown in Fig:1.5<sup>9</sup>, the dual-axis articulation is achieved using an RC helicopter tail bracket and servo push-rod mechanism; reducing the mass of the articulated component but limiting the range of its actuation. Considering the propellers as a spinning flywheel, the induced gyroscopic response was then treated as an additional controllable actuator plant. Their commanded virtual control is distributed by weighted inversion amongst the actuator set, Sec: 1.2.2. The whole project justifies the extra actuation as fault tolerance redundancy but doesn't necessarily prove how such a redundancy could be beneficial.

<sup>9</sup>Image from Development of a Dual Axis Tilt Rotorcraft UAV: Modelling, Simulation and Control [33]



**Figure 1.5:** Dual-axis tilt-rotor mechanism

### 1.2.2 Notable Quadrotor Control Implementations

#### Quadcopter Attitude Control

Attitude control of a 6-DOF body, quadrotor or otherwise, is best described by *The Attitude Control Problem* [110]. A rigid body that currently has an attitude state<sup>10</sup>  $\vec{\eta}_b$  and a desired state  $\vec{\eta}_d$ , the problem is to then find a torque control law for some error state  $\vec{\eta}_e$ :

$$\mu\tau = h(\vec{\eta}_e, t) \quad (1.2)$$

Such that both the angular position  $\lim \vec{\eta}_b \rightarrow \vec{\eta}_d$  and that angular rates  $\lim \dot{\vec{\eta}}_b \rightarrow \dot{\vec{\eta}}_d$  asymptotically stabilize as  $t \rightarrow \infty$ . A distinction must be made between angular rate vector,  $\dot{\vec{\eta}}_b = [\dot{\phi} \ \dot{\theta} \ \dot{\psi}]^T$  and the angular velocity vector  $\vec{\omega}_b = [p \ q \ r]^T$ . Depending on how the attitude is posed; with rotation matrices [59, 70, 85], quaternions [32, 36, 39, 59] or otherwise (Direct Cosine Matrix etc ...) the error state<sup>11</sup>  $\vec{\eta}_e = \vec{\eta}_d - \vec{\eta}_b$  could then differ to a (Hamilton) multiplicative relationship.

Note that here  $\vec{\eta}$  is not necessarily an Euler angle set but any attitude representative state variable.

Simulation and modelling papers often rely on Euler angle based rotation matrices for attitude representation, [14, 15, 69, 76, 94] without addressing the inherent singularity associated with such an attitude representation (*sic* Gimbal Lock, [101], Sec:3.1.2). The alternative quaternion attitude representation, first implemented on a quadrotor UAV in 2006 [107], is often used in lieu of rotation matrices but has its own caveat of *unwinding*, (Sec:3.1.4), as a result of quaternions dual-coverage [72] in  $\mathbb{R}^3$  space. Quaternions are  $\in \mathbb{R}^4$  variables for attitude representations and so a mapping  $\mathbb{R}^4 \rightarrow \mathbb{R}^3$  produces a dual coverage for each unique attitude state.

Quadrotor plant dynamics, as mentioned previously, are often simplified; especially when represented with a 3-variable Euler angle set,  $\vec{\eta} = [\phi \ \theta \ \psi]^T$ . The cross-coupled gyroscopic and Coriolis responses are both neglected when the angular velocity<sup>12</sup> is small,  $\vec{\omega}_b \approx 0$ , and the inertial matrix is diagonal,  $rk(\mathbb{I}_b) = x$  for  $\in \mathbb{R}^x$ . The consequence of which is the ineffectual deterioration of both the gyroscopic term,  $\vec{\tau}_{gyro} = -\vec{\omega}_b \times \mathbb{I}_b \vec{\omega}_b \approx 0$  and the Coriolis force term,  $\vec{F}_{cor} = -\vec{\omega}_b \times m\vec{v}_b \approx 0$  in the bodies dynamics (Chapter:3 for context). Once the coupled cross-product terms are no longer of consequence, the 6 DOF trajectory,  $\mathbf{x} = [x \ y \ z \ \phi \ \theta \ \psi]^T$ , can be treated as a series of independent SISO plants each controlled with an appropriate technique. Quaternion represented attitude plants cannot easily be decomposed into individual single-input-single-output systems (quaternion dynamics in Sec:3.1.3). So a quaternion combined four variable attitude state-space vector is then used,  $Q_b = [q_0 \ \vec{q}]^T$ , for the abstracted major loop plant.

<sup>10</sup>Quaternion attitude states will later replace Euler angles

<sup>11</sup>*The Attitude Control* [110] describes these conventionally different error states

<sup>12</sup>Angular velocity and angular rates are fundamentally different,  $\vec{\omega}_b \neq \dot{\vec{\eta}}$

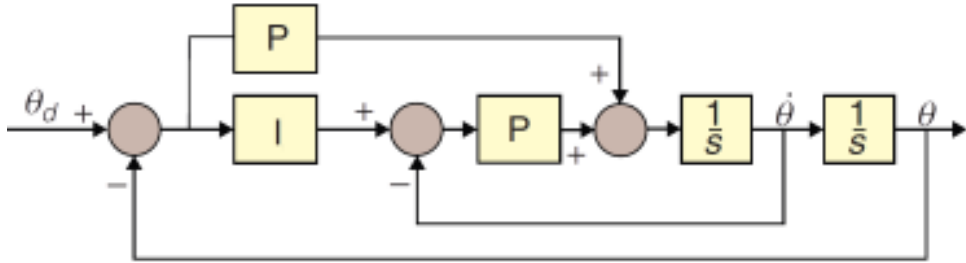


**Figure 1.6:** ArduCopter PI Euler angle attitude control loop

Commercial flight controller's software (Arducopter [4], Openpilot [63]<sup>13</sup>, CleanFlight [23], BetaFlight [10], etc ...) for custom fabricated UAV platforms all apply their own flavour of structured attitude controllers and state estimation algorithms, based on onboard hardware sensor fusion. The article *Build Your Own Quadrotor* [64] summarizes the control structures implemented on a range of popular flight controllers. The most popular of which, ArduCopter, implements a feed-forward PI compensation controller (Fig:1.6)<sup>14</sup>. PI, PD and PID controllers are all popular and effective plant independent control solutions for general attitude plants. Table:1.1 collectively lists the common attitude control blocks (not exclusively quadrotors UAVs but MAVs too) and which projects they've been implemented in, after which a critique on the more unique adaptations is given.

Controller Type	Independent	Dependent	Total
PI	[110]	[110]	2
PD	[2, 68]	[32, 76]	4
PID	[14, 16, 92, 96, 110]	[46, 94, 110]	8
Lead	[25, 89]	N/A	2
IBC	[69, 98] <sup>15</sup>	[69]	3
ABC	[9, 27, 57, 74]		4
LQR	[16]	N/A	1

**Table 1.1:** A breakdown of common attitude controllers

In a collection of papers, written by Bouabdallah, et al.[2003,2004,2007]..., arguably the most prolific early quadrotor authors, a range of different control implementations are derived and reviewed. Their last paper, *Full Control of a Quadrotor*[2007] [15], derived and practically tested an Integral Backstepping attitude controller on an OS4 quadrotor platform. It builds on their research from an earlier paper, [2003] [16], wherein an analysis of PID vs LQR attitude controllers in the context of quadrotors is posed. LQR controllers aim to optimize the controller effort (with  $u \in \mathbb{U}$ , controller effort is then  $\|u\|$  or the  $L_2$  norm of the plant input). Although, in theory, solving the associated Riccati<sup>†</sup> cost function may produce an optimal, stable and efficient control law it needs exact plant matching. In reality, exact plant matching is difficult to achieve for a quadcopter or any aerospace body for that matter. The resultant controller in [16] achieved asymptotic stability but had poor steady state performance due to low accuracy of the identified actuator dynamics and poor confidence inertial measurements.

Adaptive Backstepping Control [114](any of the examples in Table:1.1) builds on nominal IBC fundamentals by introducing an additional disturbance state term in the LCF used for the backstepping iteration. The drawback with this form of Backstepping approach is that, from the Lyapunov control theorem, a derivative for the estimated disturbance (or an *update law*) is needed. Disturbance approximation has been investigated thoroughly but, for a signal without *a priori* information, some heuristic needs to be adopted with the approximation, which usually involves some compromise.

<sup>13</sup>NOTE: OpenPilot's firmware software stack is now maintained by LibrePilot

<sup>14</sup>Image sourced from *Build your own Quadrotor* [2012] [64]

<sup>15</sup> [98] applies an IBC algorithm derived through Hurwitz polynomials, not lyapunov theorem.

In one example, [27], the authors implemented a statistical *proj(.)* operator based technique. Which, when used in adaptive control, the projection operator [21], *proj(.)*, ensures a derivative based estimator is bounded for adaptive regression approximation [88].

Although the control implementation isn't backstepping based, in [119], a sliding mode controller was used to compensate for the disturbances in an Unmanned Submersible Vehicle attitude plant. The underwater current disturbances were approximated using a fuzzy logic system, specifically a *zero-order TSK* fuzzy controller. The TSK system has been proven to act in the same way as an Artificial Neural Network approximator [71]; where the fuzzy TSK system is more comprehensible than the latter. Statistical analysis and investigation of approximators without *a priori* knowledge of a system are well beyond the scope of this research but are worth mentioning.

### Single/Dual Axis Control & Allocation

The extra actuation introduced with single and dual axis articulation provides room for more control goals to be achieved as the order of actuation increases. Of the few papers published on tilting-axis quadrotors, PD controllers (Nemati et al.[2014] [76] and again in Gasco [2012] [33] & Rihani [2012] [2]) and PID controllers (Ryll, et al. [2012,2013] [96, 97]) are the norm for attitude control blocks. For either of these systems there needs to be an allocation rule to distribute a commanded input amongst the actuator set. In [50], Johansen, et al. [2012] describes<sup>16</sup> the control allocation problem for a dynamic plant:

$$\dot{\mathbf{x}} = f(\mathbf{x}, t) + g(\mathbf{x}, t)\vec{\nu} \quad (1.3a)$$

$$y = c(\mathbf{x}, t) \quad (1.3b)$$

Note in the state space Equation:1.3a, it's assumed the plant input,  $\vec{\nu}$ , has a linear multiplicative relationship with the input response,  $g(\mathbf{x}, t, \vec{\nu}) \Rightarrow g(\mathbf{x}, t)\vec{\nu}$ .

With a state  $\mathbf{x} \in \mathbb{R}^n$  and  $f(\mathbf{x}, t)$  &  $g(\mathbf{x}, t)$  being the plant's dynamics and input response respectively. In set point tracking, the output is then *tracking* the state  $y = c(\mathbf{x}, t) = \mathbf{x}$ , and hence  $y \in \mathbb{R}^n$ . In an ideal well posed system the number of actuator inputs equals the number of controllable variable outputs; that being  $\dim(\mathbf{x}) = \dim(\nu) \in \mathbb{R}^n$ . In the case where the control input  $\nu \in \mathbb{R}^m$ , if  $m > n$  the problem is then over-actuated and a level of abstraction is needed; an asymptotically stabilizing virtual control input  $\nu_d$  is designed by a control law  $\nu_d = h(\mathbf{x}_e, t)$  to affect dynamics. The goal is to then find a function that maps  $\mathbb{R}^m \rightarrow \mathbb{R}^n$  for an actuator matrix  $u \in \mathbb{U}^m$ . An over-actuated plant can be described in state-space as:

$$\dot{\mathbf{x}} = f(\mathbf{x}, t) + g(\mathbf{x}, t)\nu_d \quad \nu_d \in \mathbb{R}^n \quad (1.4a)$$

$$\nu_c = B(\mathbf{x}, u, t) \Rightarrow B(\mathbf{x}, t)u \quad u \in \mathbb{U}^m, \quad \nu_c \in \mathbb{R}^n \quad (1.4b)$$

$$y = c(\mathbf{x}, t) = \mathbf{x} \quad (1.4c)$$

$B(\mathbf{x}, u, t)$  is the effectiveness function which quantifies how the actuator inputs  $u$  relate to the virtual commanded input  $\nu_c$ .  $B(\mathbf{x}, t, u)$  can be abstracted to a multiplicative relationship  $B(\mathbf{x}, t)u$  if the plant's dynamics permit it, such that;  $B(\mathbf{x}, t) \in \mathbb{R}^{n \times m}$ . For generic set point tracking the control law will design a desired virtual control input  $\nu_d$ , the allocation rule then has to solve  $u$  for  $\nu_c$  such that for some slack variable  $s = \nu_c - \nu_d$  is minimized:

$$\min_{u \in \mathbb{U}^m, s \in \mathbb{R}^n} \|Q_s\| \text{ subject to } B(\mathbf{x}, u, t) - h(\mathbf{x}_e, t) = \nu_c - \nu_d = s \quad u \in \mathbb{U} \quad (1.5)$$

Which ensures the commanded input  $\nu_c$  tracks the desired control input  $\nu_d$ ;  $\nu_c \rightarrow \nu_d$  as per some cost function of the slack variable  $Q_s$ . Mostly the L2 norm,  $\|Q_s\|$ , is used. In an over-actuated system it then follows that there is a whole set of possible inputs for each  $\nu_c$ . A unique actuator solution (rather than a family of solutions) to Eq:1.5 needs a secondary objective function,  $J(\mathbf{x}, u, t)$ . Eq:1.5 then becomes;

$$\min_{u \in \mathbb{U}^m, s \in \mathbb{R}^n} (\|Q_s\| + J(\mathbf{x}, u, t)) \text{ subject to } \nu_c - \nu_d = s \quad u \in \mathbb{U} \quad (1.6)$$

---

<sup>16</sup>State variable representations of [50] were changed to match this dissertation's conventions.

Those same authors, Johansen and Tjønnås [2004,2005,2008], proposed multiple control allocation solutions to a variety of systems. Following [50]; in a subsequent paper [2005] [51], Johansen and Tjønnås introduce a secondary cost function, driving the solution away from the typical quadratic programming direct or weighted inversion solution. Aiming for optimal efficiency and not just actuator saturation. In a followup paper, [2008] [52], they propose an online adaptive algorithm approach. Using a Lyapunov energy function the minimization adaptive law always settles to a feasible solution.

Over-actuation is not something often applied to quadrotors and rather than providing a comprehensive literature review of associated papers here (which are all mostly theoretical derivation), the contextual application and solutions are expanded upon later in Sec:4.6. The only overactuated quadrotor<sup>17</sup> literature which covers allocation of the extra actuators is [2,33], where the authors apply a weighted pseudo inverse (sic Moore Penrose Inverse [61]) allocation rule. A prerequisite for pseudo inversion is a multiplicative *linear* control effectiveness relationship for Eq:1.4b.

Gasco, et al. [2012] [2, 33] applied weighted inversion, relying on some very specific assumptions to achieve that linearity relationship in Eq:1.4b. For the net torque response the authors assumed the extra actuators pitch and roll angular rates,  $\dot{\phi}$  and  $\dot{\theta}$  respectively, were proportionally related as follows:

$$\dot{\phi} \approx \frac{\phi}{t_{rise}} \quad (1.7)$$

In which  $t_{rise}$  is the actuators rise time to a set-point. As a result the gyroscopic first order torque  $\tau_{gyro} = -\vec{\omega}_b \times \mathbb{I}_b \vec{\omega}_b$  and second order inertial torque  $\tau = \mathbb{I}_b \ddot{\omega}_b$  are functions of position  $\phi$  or  $\theta$ , not their derivatives. The extent of that consequence is contrasted with the allocation solution in Sec:4.6.

## Satellite Attitude Control

Unconstrained attitude set-point tracking for 6-DOF bodies, quaternion represented or otherwise, is a topic well covered in the field of satellite attitude control; [49, 58, 112]. The *status quo* for recent research is on non-linear adaptive attitude backstepping control systems, wherein the adaptive update rule is the novel contribution. Often plant uncertainty affects the inertial tensor of a satellite. In [49], the authors Wang Jia, et al. [2010], proposed applying adaptive backstepping to compensate for steady state errors of (asymmetric) inertial estimations. Alternatively, instead of deliberating on costly non-orbital prelaunch inertial measurements Bodrany, et al.[2000] [13] developed an algorithm for estimating the inertial tensor based on controlled single axis perturbations. Such an approach does assume any initial estimates are sufficiently close to true body values such that they will settle and stability can be ensured, irrespective of how unacceptable the transient performance may be.

Satellite actuator suites mostly include additional redundant effectors, to ensure fault tolerance, and thus require control allocation. Often the extra allocators are CMG actuators, flywheels driven by DC motors, to produce rotational torques. Fuel burning can only actuate for a certain period of time and so thrusters are scheduled to have a lower priority. Seen in the paper [58]; the authors, Kristiansen et al. [2005], address the over-actuation with direct and well-matched inversion before applying quaternion based backstepping for attitude control. A direct inversion solves Eq:1.6 such that:

$$u = B^\dagger(\vec{\tau}_a^b - D\vec{\omega}_{ib}^b) \quad (1.8a)$$

$$B^\dagger = B^T(BB^T)^{-1} \quad (1.8b)$$

Where  $B$  is the effectiveness matrix and  $B^\dagger$  is such that  $BB^\dagger = \mathbb{I}$ . Specifically  $B^\dagger$  is the general *pseudo* inverse of  $B$  (more on inversions in Sec:4.6). It's assumed there's a multiplicative relationship between the input,  $u \in \mathbb{U}$ , and the input effectiveness matrix in Eq:1.4b. The controller designed actuator torque  $\vec{\tau}_a^b$  then dictates the input  $u$  as in Eq:1.8a. Much like the over-actuation previously discussed W.R.T quadcopters; the pseudo inversion method of actuator distribution applies quadratic optimization to the allocation slack cost function, Eq:1.5.

---

<sup>17</sup>Birotor dual-axis tilting makes the system critically actuated and so requires no allocation.

# Chapter 2

## Prototype Design

### 2.1 Design

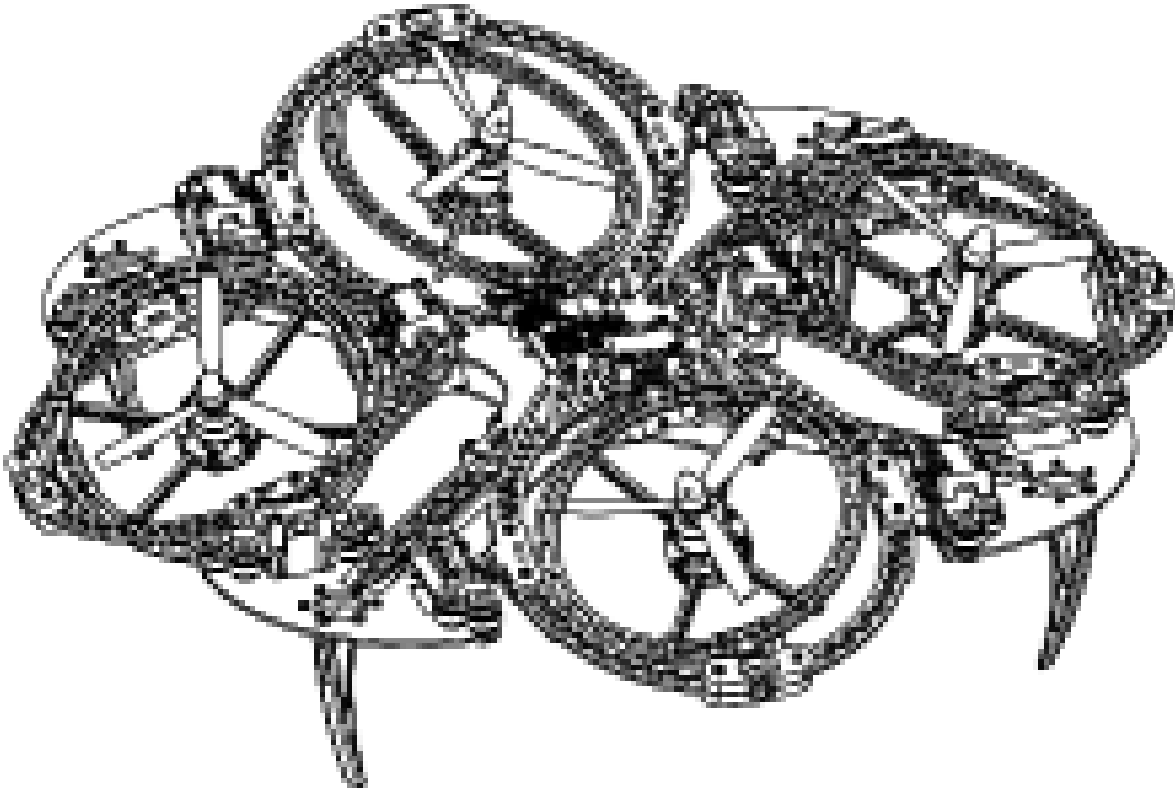


**Figure 2.1:** Isometric view of the prototype design

The final prototype (Fig:2.1) went through a series of different design iterations, all aimed at optimizing engineering time spent on construction and reducing the associated component costs thereof. A significant aspect of consideration for the design process was the net weight whose upper limit, as mentioned before, is inherently limited by the thrust produced from lift motors. Some of the more important design factors, like inertias & masses (Sec:2.3), are discussed here in order to give context for the dynamics derived later in Chapter:3. The reference frame orientations which those dynamics are developed with respect to are detailed here. A brief overview of the electrical systems layout is then given with the components associated and their electrical characteristics included. Finally the actuator suite's functionality and transfer characteristics are also quantified. A review of the physical prototype realized and control loop(s) implemented is detailed in Chapter:6 along with actual flight test results.

### 2.1.1 Actuation Functionality

The novel component of the design is the manner of articulation for each concentric gimbal ring which forms the four motor module structures. The control objective is to produce a thrust vectoring actuation set for a quadrotor's control plant. The outcome was a module which independently redirects the thrust generated by the lift propellers (Fig:2.2a). Within each module are servos affixed onto sequential support rings to pitch and roll the substructure's axes. The gyroscope-like frame that surrounds each motor/propeller pair accommodates that relative movement. Aligned with each servo is a coaxial support bearing. The bearing and actuator servos have a mass disparity which results in an eccentric center of mass, producing a gravitational torque arm. Unfortunately, due to weight constraints, counter balance measures cannot be introduced. Consequences from the center of mass variations must be either compensated for (*plant dependent solution*) or exploited in the dynamics (*additional non-linear actuator plants*). The precise effects are quantified numerically later in Sec:2.3.

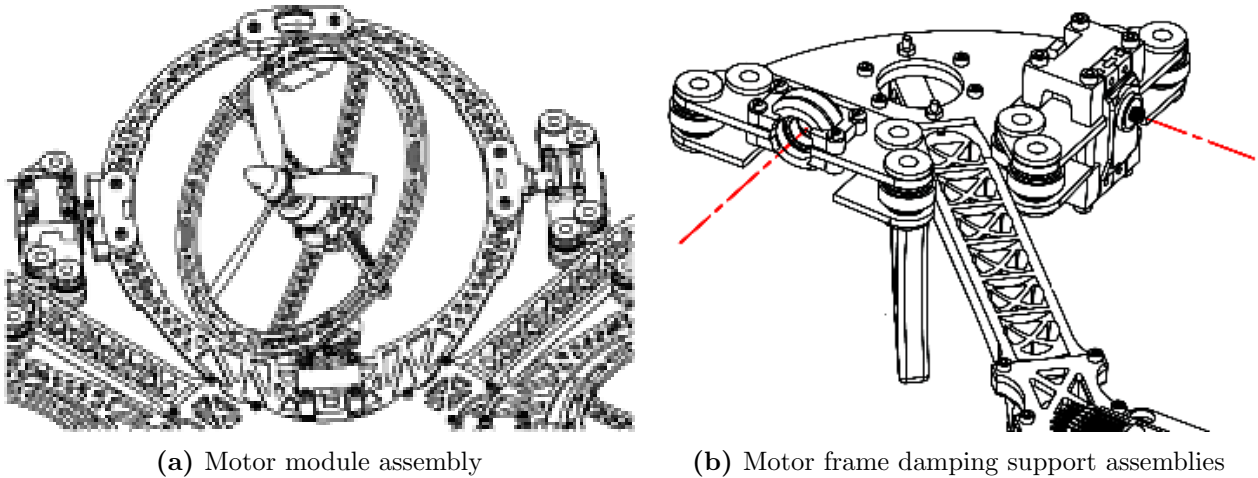


**Figure 2.2:** Tilting rotor design

Each motor module is positioned such that its produced thrust vector coincides with the intersection of its two rotational axes. As a result, there's only a perpendicular displacement,  $L_{arm} = 195.16$ , co-planar to the body frames X-Y-Z origin  $\vec{O}_b$  (see subsequent Fig:2.7). That length directly effects the differential torque plant;  $\vec{\tau}_{diff} = \sum \vec{L}_i \times \vec{T}_i$ . An eccentric thrust vector line would make that arm displacement a non-orthogonal vector. The center of gravity for each module is time varying and depends on its two servo rotational positions. It's more prudent to ensure intersection of the thrust vector with the rotational center than to balance the masses undergoing rotation. A thrust varying torque is harder to approximate and hence compensate for than a gravitational torque, given the complexity with modelling a propeller's aerodynamic thrust (Sec:3.3.1).

The primary body structure is similar to a traditional quadcopter '+' configuration with adjacent propellers spinning in opposite directions. Each motor module's rotational assembly is suspended by silicon damping balls (Fig:2.2b). A smaller damping assembly in the center of the frame houses all the electronics and power distribution circuitry. All the mounting brackets affixing the motor module rings are 3D printed from CAD models using an Ultimaker V2+ [113]. A complete bill of materials for all parts used, including working drawings for each 3D printed bracket and the laser cut frame(s), is presented in Appendix:B.

The propellers rotational plane is not aligned exactly with the plane made by the  $\hat{X}_{M_i}$  and  $\hat{Y}_{M_i}$  rotational servo axes (Fig:2.3). The offset is approximately 23.39 mm and must be considered when evaluating pitch/roll inertial and gyroscopic torque responses later in Sec:3.2.1. The propellers are 6 inch ( $6 \times 4.5$ ) 3-Blade plastic Gemfam propellers, powered by Cobra CM2208-2000KV Brushless DC motors (Fig:2.4a). The thrust produced as a function of angular velocity (in RPS) for the propellers is derived in Sec:3.3.1.

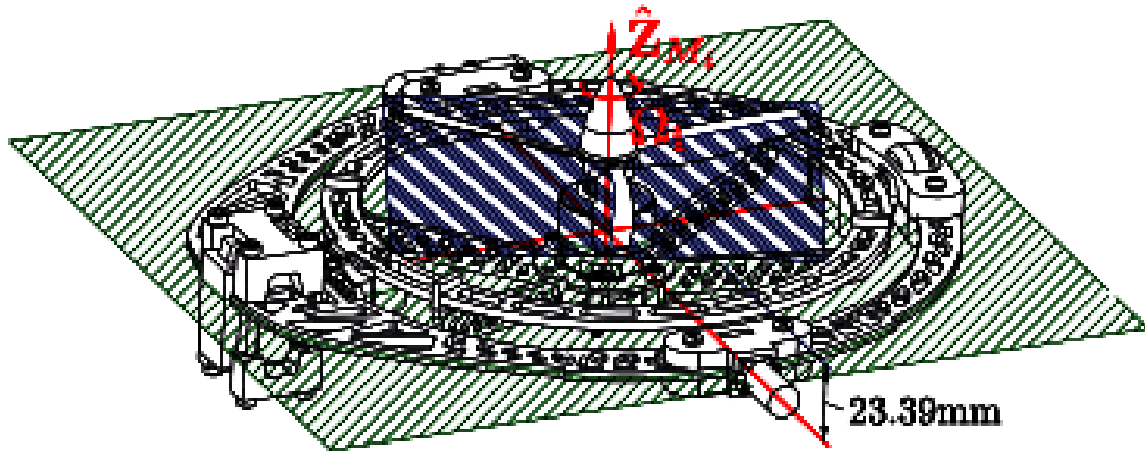
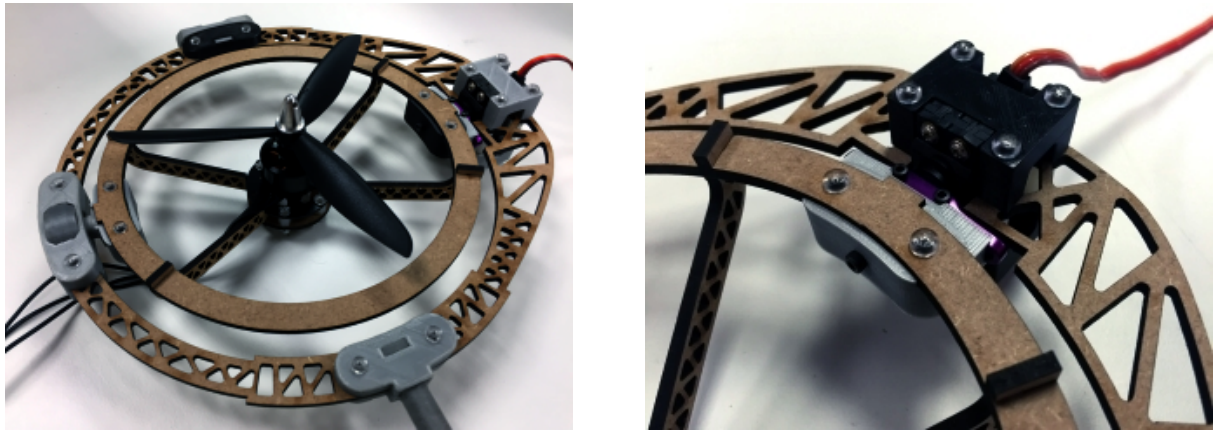


**Figure 2.3:** Difference between propeller and motor planes

The BLDC motors are controlled with LDPower 20A ESC<sup>1</sup> modules with an in-line OrangeRx RPM Sensor. The transfer function for the combined unit is presented next in Sec:2.4.1. Power for the quadrotor is supplied not from a battery bank but from a power tether. Tethered power will ensure consistent flight time and reduce the concern of payload restriction on the available lift actuation. Power lines to both the BLDC motors and servos are supplied through conventional wiring, however an ideal construction would see slip-rings for each module's power supply.



(a) Cobra CM2208-2000KV BLDC motor module

(b) Corona DS-339MG servo bracket

**Figure 2.4:** Motor module assembly

Metal gear Corona DS-339MG digital servos are used for the two axes of rotation (Fig:2.4b). Each servo has a rotational range of  $\approx \pi$ , positioned such that a zero<sup>th</sup> offset aligns the motor modules, adjacent to the body frame, and has a  $\pm \pi/2$  range. A digital servo updates at 330 Hz, faster than a 50 Hz analogue servo equivalent (Table:2.1). This means the otherwise 20ms zero-order "analogue" sampling becomes a less significant 3.30ms zero-order holding time. Both the  $\hat{X}_{M_i}$  and  $\hat{Y}_{M_i}$  axis servos will be rotating a large loading mass and as such their *open loop* plant dynamics are determined empirically in Sec:2.4.1.

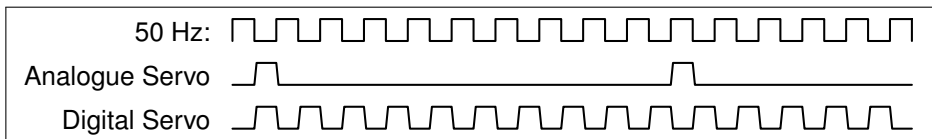


**Table 2.1:** Analogue & digital timing signals

<sup>1</sup>Flashed with BLHeli [11] firmware. The default firmware on the speed controllers had an unsatisfactory exponential approach (not linear) input speed curve. In contrast with the speed curve in Fig:2.16.

## 2.2 Conventions Used

Attitude conventions used for deriving the system's dynamics, in the next Chapter:3, are first briefly discussed here. Often these aspects are assumed to be obvious enough that they're omitted. It's important to clearly and unambiguously define a standard set of framing conventions to avoid uncertainty later. Rotation matrices are included but the focus is on the *contrast* between rotation and transformation operations. Both [39] and [85] provide an in depth and thorough explanation of rotation matrices and DCM attitude representation if such concepts are unfamiliar to the reader. Quaternions are introduced to replace rotation matrices in Sec:3.1.3.

### 2.2.1 Reference Frames Convention

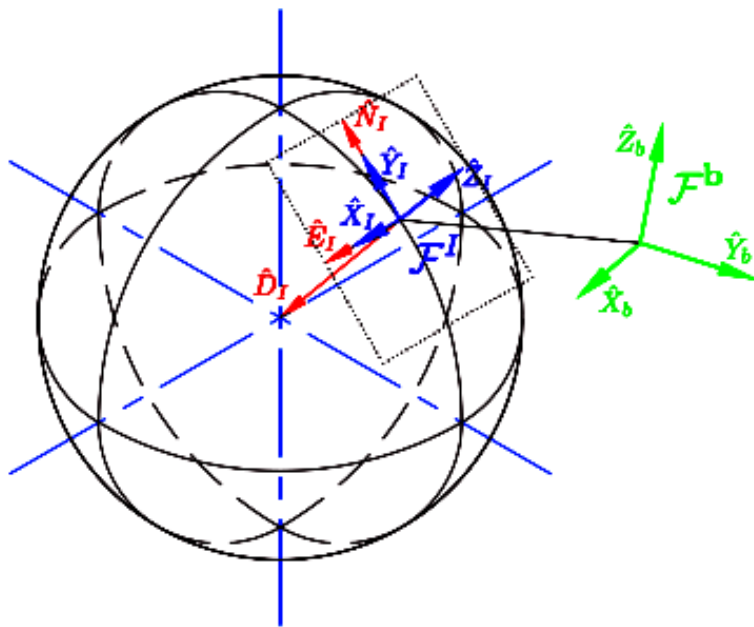


**Figure 2.5:** Inertial and body reference frames

NASA aerospace frames are used for principle cartesian inertial and body coordinate representation (Fig:2.5). The inertial frame,  $\mathcal{F}^I$ , is aligned such that the  $\hat{X}_I$  axis is in the  $\hat{N}$ orth direction,  $\hat{Y}_I$  is in the  $\hat{E}$ ast direction and  $-\hat{Z}_I$  is in the  $\hat{D}$ ownward direction<sup>2</sup>. The body frame,  $\mathcal{F}^b$ , then has both  $\hat{X}_b$  and  $\hat{Y}_b$  aligned obliquely between two perpendicular arms of the quadrotor's body and the  $\hat{Z}_b$  axis in the body's normal direction (illustrated in Fig:2.8). The body frame's axes and their relation to the prototype design are highlighted next in Sec:2.2.2. Frame superscripts  $I$  and  $b$  represent inertial and body frames respectively whilst vector subscripts imply the reference frame in which the vector's coordinates exists or taken relative to. In certain cases a preceding super-script

Relative angular displacement between two frames is commonly measured by the three angle Euler set. The Euler angles  $\vec{\eta} = [\phi \ \theta \ \psi]^T$  represent rotations about the  $\hat{X}, \hat{Y}$  and  $\hat{Z}$  axes respectively. Depending on how the rotation sequence is formulated, those angles can be used to construct rotation matrices which give relation to vectors or can transform coordinates. The generic equation to *rotate* a vector  $\vec{v}$  about some (normalized) axis  $\hat{n}$  through an angle  $\mu$  is given by<sup>3</sup>:

$$\vec{v}' = (1 - \cos(\mu))(\vec{v} \cdot \hat{n})\hat{n} + \cos(\mu)\vec{v} + \sin(\mu)(\hat{n} \times \vec{v}) \quad (2.1)$$

Which, when  $\hat{n}$  is either  $\hat{X}, \hat{Y}$  or  $\hat{Z}$  axes, can be simplified to produce the three fundamental rotation matrices;  $\mathbb{R}_x(\phi), \mathbb{R}_y(\theta)$  and  $\mathbb{R}_z(\psi)$ .

<sup>2</sup>In Euler orbital sequences this would be toward the Earth's center, sometimes referred to as the NED convention

<sup>3</sup>Derived and proven in *Quadrotor Dynamics and Control* [92]

Multiplication by a rotation matrix  $\mathbb{R}_n(\cdot)$  applies a left-handed *rotation* operator about some axis  $\hat{n}$ , the resultant vector still exists in the same reference frame. For example an  $\hat{X}$  axis rotation by  $\phi$  is given by;

$$\vec{v}' = \mathbb{R}_x(\phi)\vec{v} \quad (2.2a)$$

$$\vec{v}', \vec{v} \in \mathcal{F}^1 \quad (2.2b)$$

No subscripts are used in Eq: 2.2 to indicate reference frame ownership because all vectors are in the same frame

A vector *transformation* changes the resultant vector's reference frame. The transformation is then a rotation by an angle of the *difference* between the resulting and principle reference frames. A transformation from frame  $\mathcal{F}^1$  to  $\mathcal{F}^2$ , differing by an angle of  $\phi$  about the  $\hat{X}$  axis is then:

$$\vec{v}_2 = \mathbb{R}_x(-\phi)\vec{v}_1 \quad (2.3a)$$

$$\vec{v}_2 \in \mathcal{F}^2 \text{ and } \vec{v}_1 \in \mathcal{F}^1 \quad (2.3b)$$

The distinction between Eq:2.2 and Eq:2.3 is the directional sense of the angular operand  $\phi$ , and hence the effect it has on the argument vector. The transformation or rotation of a vector from  $\mathcal{F}^I$  to  $\mathcal{F}^b$  is the product of three sequential operations about each axis. Each subsequent rotation is applied relative to a new intermediate frame; hence each Euler angle is taken relative to a specific intermediate frame and not a global one. The order of those axial rotation operations does indeed effect the Euler set. Any consequences of that chosen order is something discussed indepth in *Quaternions and Rotation Sequence*, [59]. In this dissertation the Z-Y-X rotation sequence is used. A transformation of the vector  $\vec{v}$  from the inertial to the body frame,  $\mathcal{F}^I \rightarrow \mathcal{F}^b$ , is then applied by:

$$\mathbb{R}_I^b \triangleq \mathbb{R}_z(\psi)\mathbb{R}_y(\theta)\mathbb{R}_x(\phi) \quad (2.4a)$$

$$\vec{v}_b = \mathbb{R}_I^b(-\psi, -\theta, -\phi)\vec{v}_I \quad (2.4b)$$

$$\Rightarrow \vec{v}_b = \mathbb{R}_z(-\psi)\mathbb{R}_y(-\theta)\mathbb{R}_x(-\phi)\vec{v}_I \quad (2.4c)$$

$$\mathbb{R}_z(-\psi)\mathbb{R}_y(-\theta)\mathbb{R}_x(-\phi) \iff \mathbb{R}_x(\phi)\mathbb{R}_y(\theta)\mathbb{R}_z(\psi) = \mathbb{R}_b^I \quad (2.4d)$$

$$\mathbb{R}_I^b = (\mathbb{R}_b^I)^{-1} = (\mathbb{R}_b^I)^T \quad (2.4e)$$

The relationship in Eq:2.4e is an inversion property (*transpose*) of the rotation matrix. A rotation matrix's inverse can be used interchangeably with its negative counterpart to maintain a positive sense of the argument angle. To ensure clarity throughout this dissertation's mathematics, a negative angular sense implies a *transformation* to a different reference frame. Where applicable, the order of rotation will indicate the sequence direction and an angular signs differentiate the rotation and transformation operations.

The body frame's angular velocity is taken relative to the inertial frame, represented by  $\vec{\omega}_{b/I} \Rightarrow \vec{\omega}_b$ . Seeing that each Euler angle is measured with respect to an intermediary frame, a distinction must then be made between  $d\vec{\eta}/dt$  and  $\vec{\omega}_b$ . All three Euler angles need to be transformed to one common frame. Exploiting vehicle frames 1 & 2, or rather  $\mathcal{F}^{v1}$  &  $\mathcal{F}^{v2}$ , as intermediary frames to respectively describe post  $\mathbb{R}_x(\phi)$  and  $\mathbb{R}_y(\theta)$  operations.

$$\vec{\omega}_b = [p \quad q \quad r]^T = \frac{d}{dt}\vec{\eta} \quad \in \mathcal{F}^b \quad (2.5a)$$

$$= \frac{d\phi}{dt} \mathbb{R}_{v2}^b(\phi) \begin{bmatrix} \phi \\ 0 \\ 0 \end{bmatrix} + \frac{d\theta}{dt} \mathbb{R}_{v2}^b(\phi) \mathbb{R}_{v1}^{v2}(\theta) \begin{bmatrix} 0 \\ \theta \\ 0 \end{bmatrix} + \frac{d\psi}{dt} \mathbb{R}_{v2}^b(\phi) \mathbb{R}_{v1}^{v2}(\theta) \mathbb{R}_I^{v1}(\psi) \begin{bmatrix} 0 \\ 0 \\ \psi \end{bmatrix} \quad (2.5b)$$

The vehicle frames in Eq:2.5a and the subsequent rotations between each frame don't necessarily have to be in that order. The equation could change depending on what rotation sequence was used.

Which then simplifies to the formal relationship between two rotating frames, with  $\vec{\omega}_b = [p \ q \ r]^T$  in  $\text{rad.s}^{-1}$ :

$$\begin{bmatrix} p \\ q \\ r \end{bmatrix} = \begin{bmatrix} 1 & 0 & -\sin(\theta) \\ 0 & \cos(\phi) & \sin(\phi)\cos(\theta) \\ 0 & -\sin(\theta) & \cos(\phi)\sin(\theta) \end{bmatrix} \begin{bmatrix} \dot{\phi} \\ \dot{\theta} \\ \dot{\psi} \end{bmatrix} \quad (2.5c)$$

$$\Rightarrow \vec{\omega}_b = \Psi(\eta) \dot{\vec{\eta}} \in \mathcal{F}^b \quad (2.5d)$$

$$\Psi(\eta) = \begin{bmatrix} 1 & 0 & -\sin(\theta) \\ 0 & \cos(\phi) & \sin(\phi)\cos(\theta) \\ 0 & -\sin(\theta) & \cos(\phi)\sin(\theta) \end{bmatrix} \quad (2.5e)$$

$$\Rightarrow \dot{\vec{\eta}} = \Psi^{-1}(\eta) \vec{\omega}_b = \Phi(\eta) \vec{\omega}_b \in \mathcal{F}^{v1,v2,I} \quad (2.5f)$$

$$\Phi(\mathcal{E}) = \begin{bmatrix} 1 & \sin(\phi)\tan(\theta) & \cos(\phi)\tan(\theta) \\ 0 & \cos(\phi) & -\sin(\phi) \\ 0 & \sin(\phi)\sec(\theta) & \cos(\phi)\sec(\theta) \end{bmatrix} \quad (2.5g)$$

The termed *Euler* matrix,  $\Phi(\eta)$ , contains a well known and problematic singularity at  $\theta = \pm\pi/2$ ; because  $\tan(\theta), \sec(\theta) \rightarrow \infty$  as  $\theta \rightarrow \pi/2$ . The mathematical manifestation of the rotation matrix singularity and its practical implications are further explored later in Sec:3.1.2. The singularity is present in the middle rotation angle,  $\theta$ , which is a direct consequence of the chosen Z-Y-X rotation sequence adopted. Each Euler angle can potentially suffer a singularity depending on how the rotations are ordered. Indeed quaternions are used for kinematics later in lieu of Euler angles in later dynamics (Sec:3.1.3). Euler angular attitude representation is, however, easily understood and well suited to the conventional distinctions made in this Chapter.

Quaternion operations are similarly sequenced in the Z-Y-X order. Quaternion operations are additive and not commutative. The sequenced quaternion order will produce the same resultant frame rotation however the quaternion and its rotation path will differ. For a quaternion  $Q_b$  representing the body's attitude:

$$\mathbb{R}_I^b \iff Q_b \otimes (\cdot) \otimes Q_b^* \quad (2.6a)$$

$$Q_b \triangleq Q_z Q_y Q_x \text{ and it's inverse } Q_b^* \triangleq Q_x^* Q_y^* Q_z^* \quad (2.6b)$$

With  $\otimes$  being the Hamilton product<sup>4</sup> (or quaternion multiplication). Each quaternion<sup>5</sup>,  $Q_{\hat{i}}$ , is always a unit quaternion about that  $\hat{i}^{th}$  axis. It is important to note that a quaternion rotation operates on an argument vector with a zero quaternion scalar component. So then for some vector  $\vec{v}$ , the quaternion rotation operation in Eq:2.6a is equivalent to;

$$Q_{\vec{v}}' = Q \otimes (Q_{\vec{v}}) \otimes Q^* \quad (2.7a)$$

$$\text{Where } Q_{\vec{v}} = \begin{bmatrix} 0 \\ \vec{v} \end{bmatrix}, \quad Q_{\vec{v}}' = \begin{bmatrix} 0 \\ \vec{v}' \end{bmatrix} \quad (2.7b)$$

The quaternion representation in Eq:2.7b ensures that the operation is entirely in  $\mathbb{R}^4$  space. However it is typically omitted, despite  $\mathbb{R}^4$  being implied and as such, Eq:2.7a is then simply:

$$\vec{v}' = Q \otimes (\vec{v}) \otimes Q^* \quad (2.8)$$

Quaternion dynamics, and the quaternion operator, are later expanded upon to replace the use of Euler angles and Rotation matrices as a convention for attitude representation later in Chapter:3. Quaternion dynamics are widely regarded as the best choice for aerospace attitude representation due to their dual coverage and globally non-singular nature.

<sup>4</sup>Later used again for inertial tensor transformations

<sup>5</sup>For the body quaternion,  $Q_b$ , it's a unit quaternion rotation about the body's singular Euler axis.

### 2.2.2 Motor Axis Layout

Fundamentally the whole structure consists of multiple rigid bodies with only relative rotations between each body permitted, illustrated previously in the design description in Sec:2.1. Those rigid bodies are categorized into four inter-connected motor modules,  $M_{1 \rightarrow 4}$ , and a single body structure,  $\mathbb{B}$  (*frame* structure, not reference frame). Each module consists of two sequential gimbal rings, each with one degree of relative rotation between itself and the next subsequent ring. There needs to be distinct nomenclature used for describing these motor modules such that their dynamic derivations are contextually clear and logical.

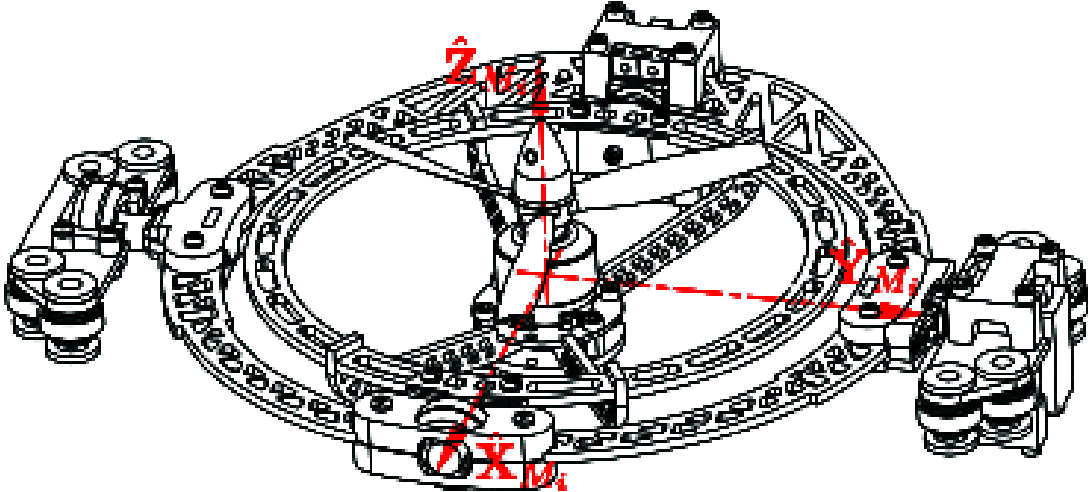


**Figure 2.6:** Aligned motor frame axes

Every propeller/motor pair is actuated by two servos. The  $i^{th}$  propeller, directly driven by the motor's rotor, has a rotational speed  $\Omega_i$  [RPS] about the  $\hat{Z}$  stator axis. Two servos are aligned *at rest* with the motor's  $\hat{Y}$  and  $\hat{X}$  axes to pitch and roll the propeller away from its principle frame. Each motor has its own reference frame,  $\mathcal{F}^{M_i}$ , aligned as shown in Fig:2.6 and highlighted with the rotational rings in Fig:2.7.

Motor frames, numbered  $1 \rightarrow 4$ , transform to the body frame first by an angle of  $\lambda_i$  about the  $\hat{X}_{M_i}$  axis. Then by  $\alpha_i$  about the  $\hat{Y}_{M'_i}$  axis in an intermediate  $M'_i$  frame. The first servo actuates  $\lambda_i$ , rotating  $\mathcal{F}^{M_i}$  to an intermediate  $\mathcal{F}^{M'_i}$  frame. Secondly, the next servo actuates  $\alpha_i$  to produce a second intermediate frame  $M''_i$ . That second servo is affixed in the  $M''_i$  frame. Lastly there's a relative orthogonal rotation about  $\hat{Z}_{M''_i}$  between  $\mathcal{F}^b$  and  $\mathcal{F}^{M''_i}$ . Each module's actuation state is fully described by  $[\Omega_i \ \lambda_i \ \alpha_i]^T$  for  $i \in [1 : 4]$ . The four motor modules are aligned relative to the body's XYZ axes as shown in Fig:2.8. Modules 1 and 3 have their X-axes in the positive and negative  $\hat{X}_b$  directions of the body frame respectively. Similarly Modules 2 and 4 have their X-axes in the positive and negative  $\hat{Y}_b$  directions of the body frame.

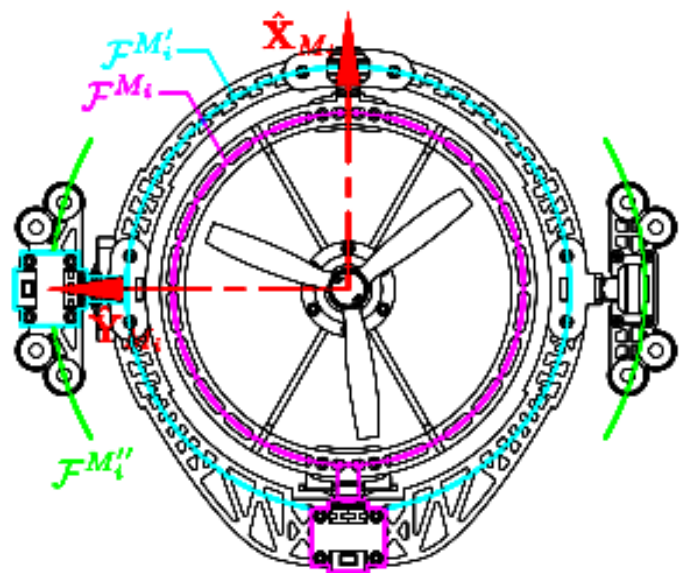


**Figure 2.7:** Intermediate motor frames

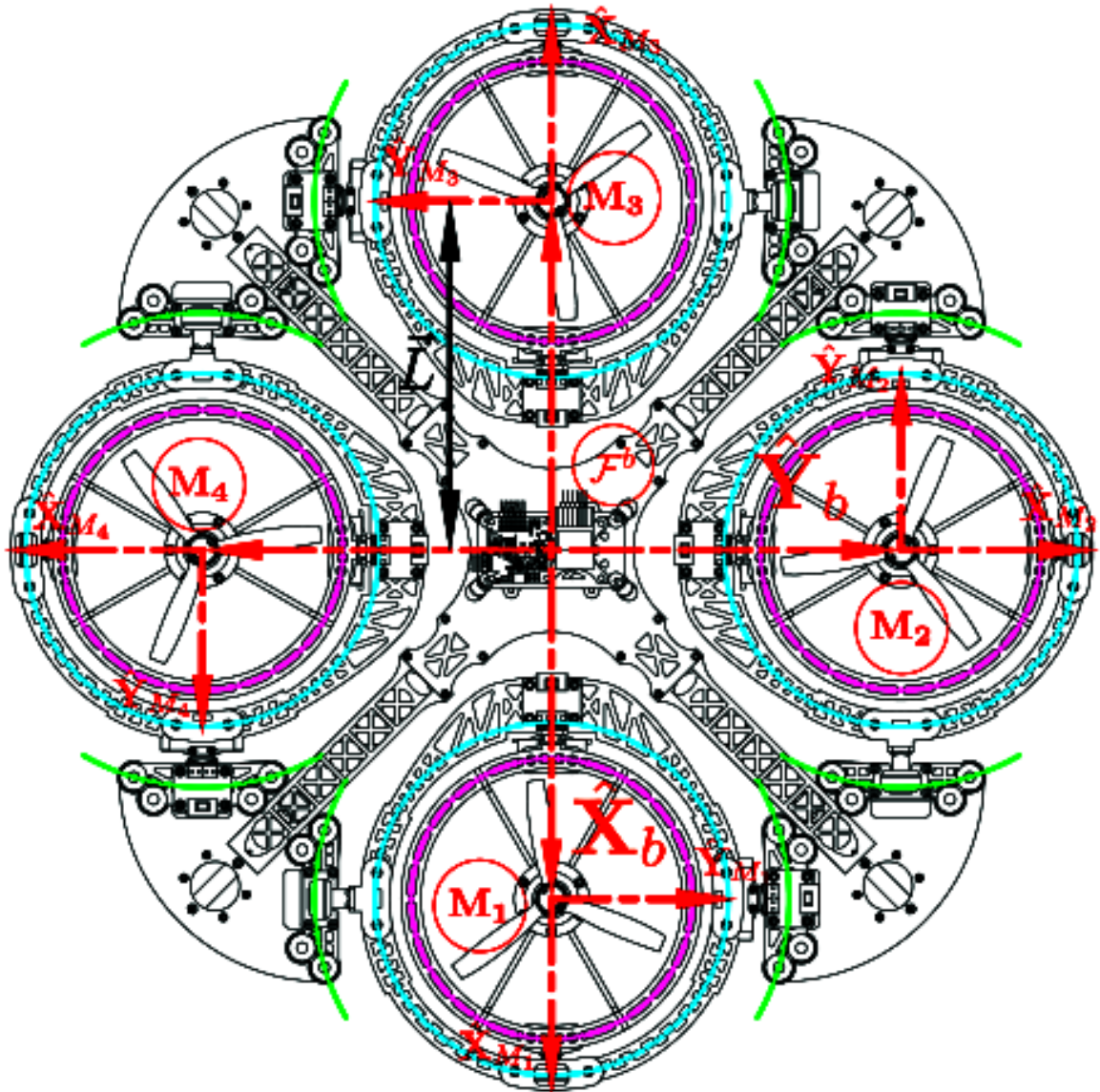


**Figure 2.8:** Body frame axes layout

Not shown in Fig:2.8 is the relative  $\hat{Z}$  axis position with respect to the structure. The  $\hat{Z}$  height of the body's motion centroid is such that its origin is co-planar with the four motor modules rotational centers. The center of motion is not the center of mass, an aspect which is discussed next in Sec:2.3. Motor modules 1 & 3 have clockwise (*positive*) rotating propellers, conversely modules 2 & 4 have counter-clockwise (*negative*) rotations. Vector transformations from each of the four motor frames to the body frame are characterized as:

$$\vec{v}_b = \mathbb{R}_z(-\sigma_i)\mathbb{R}_y(-\alpha_i)\mathbb{R}_x(-\lambda_i)\vec{v}_{M_i}, \quad \sigma_i \in \frac{1}{2}[0, \pi, 2\pi, 3\pi] \quad (2.9a)$$

With orthogonal rotation matrices  $\mathbb{R}_z$ :

$$\mathbb{R}_z = \begin{bmatrix} 1 & 0 & 0 \\ 0 & 1 & 0 \\ 0 & 0 & 1 \end{bmatrix}, \begin{bmatrix} 0 & -1 & 0 \\ 1 & 0 & 0 \\ 0 & 0 & 1 \end{bmatrix}, \begin{bmatrix} -1 & 0 & 0 \\ 0 & -1 & 0 \\ 0 & 0 & 1 \end{bmatrix}, \begin{bmatrix} 0 & 1 & 0 \\ -1 & 0 & 0 \\ 0 & 0 & 1 \end{bmatrix} \text{ for } i \in [1, 2, 3, 4] \text{ respectively} \quad (2.9b)$$

The entire actuator space, including propeller speed  $\Omega_i$  [RPS], is then  $\in \mathbb{R}^{12}$ , or rather  $\mathbb{U} \in \mathbb{R}^{12}$ , in contrast with  $\mathbb{U} \in \mathbb{R}^4$  for a traditional quadrotor. The actuator input set  $u \in \mathbb{U}$  is then structured as:

$$u_{\mathbb{U}} = [\Omega_1 \quad \lambda_1 \quad \alpha_1 \quad \dots \quad -\Omega_4 \quad \lambda_4 \quad \alpha_4]^T \quad (2.10)$$

## 2.3 Inertial Matrices & Masses

Although inertias are presented here rounded to either 2 or 0 decimal places, full floating point numbers are used in simulation and prototype software. In some cases when transforming inertias it's more appropriate to use rotation matrices to apply the transformation and not quaternions. Spatial rotation of inertial tensors are ill suited to quaternion parametrization.

### Inertias

An undesirable side effect of the relative rotations within a non-rigid body are the inertial responses associated with such movements. Given Newton's Second Law of Rotational Motion<sup>†</sup>, each applied rotation is going to produce an equal but opposite reaction onto the principle inducing frame. Similarly a gyroscopic cross product from rotational velocities is also present. Such first and second order effects are often neglected given that the angular rates which they're dependent on are mostly small enough to approximate as zero,  $\vec{\omega}_b \approx \vec{0}$ . A dynamic set-point (non-zero) attitude tracking plant is, however, going to produce non-zero time varying body angular velocities and accelerations. Unlike a traditionally actuated quadrotor, such effects will need to be compensated for.

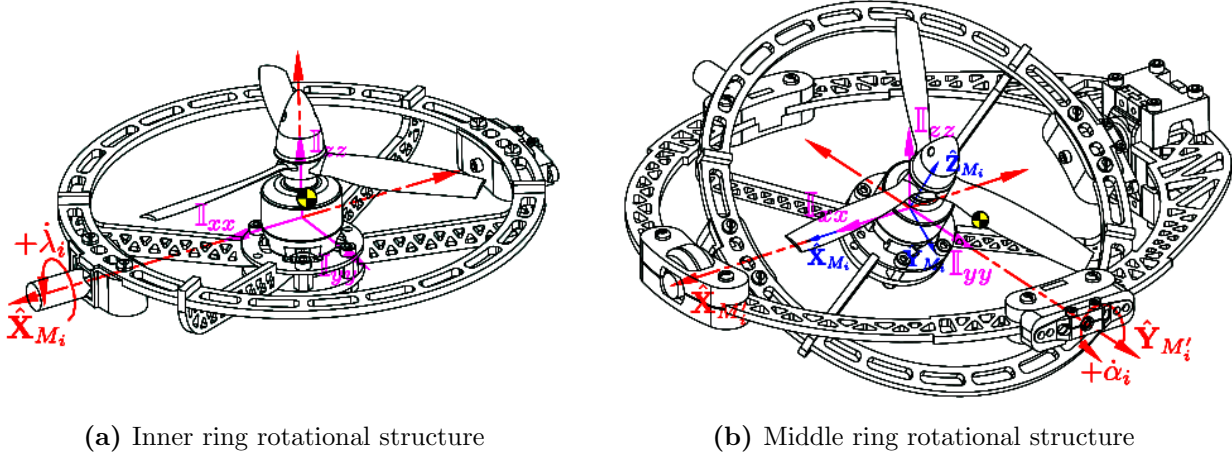


**Figure 2.9:** Inertial measurement references

The manifestation of those responses are derived next in Sec:3.2.1. Both of those effects are dependent on the rotational body's inertial tensor<sup>6</sup> about each respective rotational axis. The magnitude of those inertias are obviously a by-product of the structure's design. Starting with the innermost assembly, in each motor frame  $F^{M_i}$ , the inner ring structure is a 92g body (all components incorporated). The rotational center roughly coincides with the center of its mass ( $C.M = [-1.44 \ 0 \ 5.81]^T [mm]$  relative to its rotational center). The inner ring, being rotated by  $\lambda_i$  about the  $\hat{X}_{M_i}$  axis, then has an inertial matrix (centered and aligned with axes as in Fig:2.9a):

$$\mathbb{I}_{M_i} = \begin{bmatrix} 561.96 & -32.29 & -0.26 \\ -32.29 & 1888.74 & 0.00 \\ -0.26 & 0.00 & 2090.97 \end{bmatrix} [g.cm^2] \quad (2.11a)$$

$$\approx diag(562, 1889, 2091) \times 10^{-7} [kg.m^2] \quad (2.11b)$$

The effect of rapidly spinning propellers on the inertia in Eq:2.11a is approximated well by a solid disc, hence the inner ring's inertial components are regarded as constant. The moment of inertia about that  $\hat{X}_{M_i}$  rotational axis, pertinent to a  $\lambda_i$  rotation, is then  $\mathbb{I}_\lambda \approx 531 \times 10^{-7} [kg.m^2]$ .

<sup>6</sup>All inertias are assumed symmetrical and calculated in SolidWorks with overridden masses to match physical prototype measurements, all those values are included in Appendix:B

The first  $\lambda_i$  actuating servo and bearing supports are affixed to the intermediate middle ring assembly (Fig:2.9b). The middle ring frame,  $\mathcal{F}^{M'_i}$ , is a 98g body, excluding the inner most ring. Collectively the mass for both the inner and middle rings assemblies is  $m_{module} = 190g$ . The middle ring is rotated by  $\alpha_i$  about its  $\hat{Y}_{M'_i}$  axis. The compound body's inertia about that axis of rotation,  $\hat{Y}_{M_i}$ , is a combination of both the middle ring's inertia and the inner ring's. The latter's contribution dependant on the *rotation* (not transformation) angle  $\lambda_i$  which, from the conservation of angular momentum theory [106]<sup>7</sup>, is:

$$\text{If } \mathbb{I}_{middle} = \begin{bmatrix} 2905.70 & 0.02 & 390.89 \\ 0.02 & 8446.41 & 0.01 \\ 390.89 & 0.01 & 11125.74 \end{bmatrix} \quad [\text{g.cm}^2] \quad (2.12a)$$

$$\mathbb{I}_{M'_i} = \mathbb{I}_{middle} + \mathbb{R}_x(\lambda_i)(\mathbb{I}_{inner})\mathbb{R}_x^{-1}(\lambda_i) \quad (2.12b)$$

$$\mathbb{I}_{M'_i}(\lambda_i) = \mathbb{I}_{const} + \mathbb{I}_{M_i}(\lambda_i) \quad (2.12c)$$

$$\approx \begin{bmatrix} 3468 & 0 & 391 \\ 0 & 10436 & 0 \\ 391 & 0 & 13155 \end{bmatrix} + \begin{bmatrix} 0 & -32c_\lambda & -32s_\lambda \\ -32c_\lambda & -101c_{2\lambda} & 101s_{2\lambda} \\ -32s_\lambda & 101s_{2\lambda} & 101c_{2\lambda} \end{bmatrix} \times 10^{-7} \quad [\text{kg.m}^2] \quad (2.12d)$$

With  $\mathbb{I}_{inner} = \mathbb{I}_{M_i}$  being the inertia from Eq:2.11a, re-orientated through a rotation  $\mathbb{R}_x(\lambda_i)$ . The net inertia is then a combination of an inertia as a function of the rotation angle  $\lambda_i$  and a constant inertial component (Eq:2.12c), which together are then simplified<sup>8</sup> to Eq:2.12d. It's important to note the two non-zero products of inertia,  $\mathbb{I}_{yx}$  and  $\mathbb{I}_{yz}$ , which are going to result in a vector torque  $\vec{\tau}_\alpha$  response. The inertia then encountered by an  $\alpha_i$  rotation is:

$$\mathbb{I}_\alpha(\lambda) \approx [-32c_\lambda, 10436 - 101c_{2\lambda}, 101s_{2\lambda}]^T \times 10^{-7} \quad [\text{kg.m}^2] \quad (2.13)$$

Variable inertias dependent on state input variables are one of many non-trivial aspects unique to the multi-body interconnected design. Control solutions are thus decidedly plant dependent in their formulation. The center of mass for each motor module's compound assembly coincides with neither rotational axes' intersections. As a result the effective center of mass for each module, and the entire structure, is going to be a time varying function each motor module's angular rotational position.

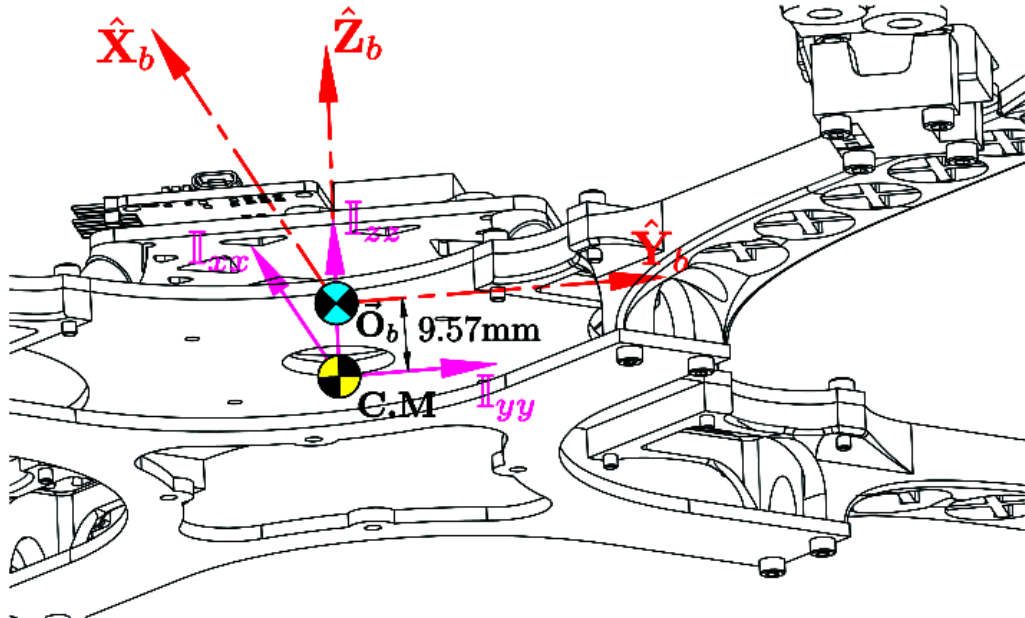


Figure 2.10: Body structure's center of mass

<sup>7</sup> $\mathbb{R}_x$  is a full rank and square, so an inverse  $\mathbb{R}_x^{-1}$  always exists.

<sup>8</sup>Eq:2.12d is rounded to no decimal places, its units are already  $\times 10^{-7}$  and thus small products of inertia are omitted.

The second  $\alpha_i$  rotating servo adjoins the complete motor module (both the inner and middle ring assemblies) to the body structure. The inertial volume of the servo and bearing supports contribute then to the body structure's inertia, whose value excludes any of the four motor modules. Consisting of servo and bearing damping brackets, each "damping" assembly collectively weighs 84g and suspends the motor modules from the body frame with a set of silicon damping balls. The body structure's center of mass (without motor modules, Fig:2.10) coincides with the XY directional axes and lies  $\Delta Z = -9.57 \text{ mm}$  below the Body Frame's origin of motion;  $\vec{\mathbf{O}}_b \in \mathcal{F}^b$ .

*Note: that body frame origin which all motion is calculated with respect to is co-planar to the motor module's rotational centers, not the net center of mass.*

The body's weight, including all four damping assemblies and electronics, totals to 814.7 g. The body's net inertia (*sans* motor modules)  $\mathbb{I}_{body}$ , about its center of mass (Fig:2.10) is:

$$\mathbb{I}_{body} = \begin{bmatrix} 181689.67 & -0.44 & -8.86 \\ -0.44 & 181567.22 & -19.44 \\ -8.86 & -19.44 & 360077.58 \end{bmatrix} \times 10^{-7} \text{ [kg.m}^2\text{]} \quad (2.14a)$$

Using the Parallel Axis theorem<sup>†</sup>, that same net body inertia about the body frame's origin,  $\vec{\mathbf{O}}_b$ , is:

$$\mathbb{I}_{body}' = \mathbb{I}_{body} + m(\vec{d} \cdot \vec{d} + \vec{d} \otimes \vec{d}) \approx \mathbb{I}_{body} + md^2 \quad (2.14b)$$

Here  $\otimes$  represents the Hamilton product of two 3X3 matrices, it's used elsewhere to indicate the quaternion multiplication operator. The vector  $\vec{d}$  is the difference between the center of mass C.M and the body frame origin  $\vec{\mathbf{O}}_b$ .

$$\mathbb{I}_{body}' = \begin{bmatrix} 182435.66 & -0.42 & -6.46 \\ -0.42 & 182313.18 & -14.52 \\ -6.46 & -10.41 & 360077.62 \end{bmatrix} \times 10^{-7} \text{ [kg.m}^2\text{]} \quad (2.14c)$$

Net inertia for the compound assembly,  $\mathbb{I}_b$ <sup>9</sup>, about the origin  $\vec{\mathbf{O}}_b$  is a combination of all the relative attached bodies. That being; the four motor modules, transformed and then translated to the body frame origin, and the body structure itself. That transformation from the motor frame  $\mathcal{F}^{M_i}$  to the body frame  $\mathcal{F}^b$  is analogous to that of Eq: 2.9. Reiterating that the the origin is co-planar to the module's center of rotation, each motor module's inertia,  $\mathbb{I}_{M'_i}$ <sup>10</sup>, is further rotated by  $\alpha_i$  about  $\hat{Y}_{M'_i}$  and finally an orthogonal  $\hat{Z}_{M''_i}$  rotation (aligned with  $\hat{Z}_b$ ) onto  $\mathcal{F}^b$ . Still measured with respect to their individual rotational centers ( $\vec{\mathbf{M}}_i$  in Fig:2.11) but re-orientated to align with  $||\vec{\mathbf{O}}_b$ . Contribution of each motor module's inertia, with  $\mathbb{R}_z$  being the same as Eq:2.9b, is then:

$$\mathbb{I}_{i^{th}motor} = \mathbb{R}_z(\sigma_i)\mathbb{R}_z(\alpha_i)(\mathbb{I}_{M'_i}(\lambda_i))\mathbb{R}_y^{-1}(\alpha_i)\mathbb{R}_z^{-1}(\sigma_i) \quad (2.15a)$$

Or expanding that to individual inner and middle ring contributions:

$$= \mathbb{R}_z\mathbb{R}_y(\alpha_i)(\mathbb{I}_{middle})\mathbb{R}_y^{-1}(\alpha_i)\mathbb{R}_z^{-1} + \mathbb{R}_z\mathbb{R}_y(\alpha_i)\mathbb{R}_x(\lambda_i)(\mathbb{I}_{inner})\mathbb{R}_x^{-1}(\lambda_i)\mathbb{R}_y^{-1}(\alpha_i)\mathbb{R}_z^{-1} \quad (2.15b)$$

$$\text{With respective axes } \hat{X} \in \mathcal{F}^{M_i}, \quad \hat{Y} \in \mathcal{F}^{M'_i}, \quad \hat{Z} \in \mathcal{F}^{M''_i} \quad (2.15c)$$

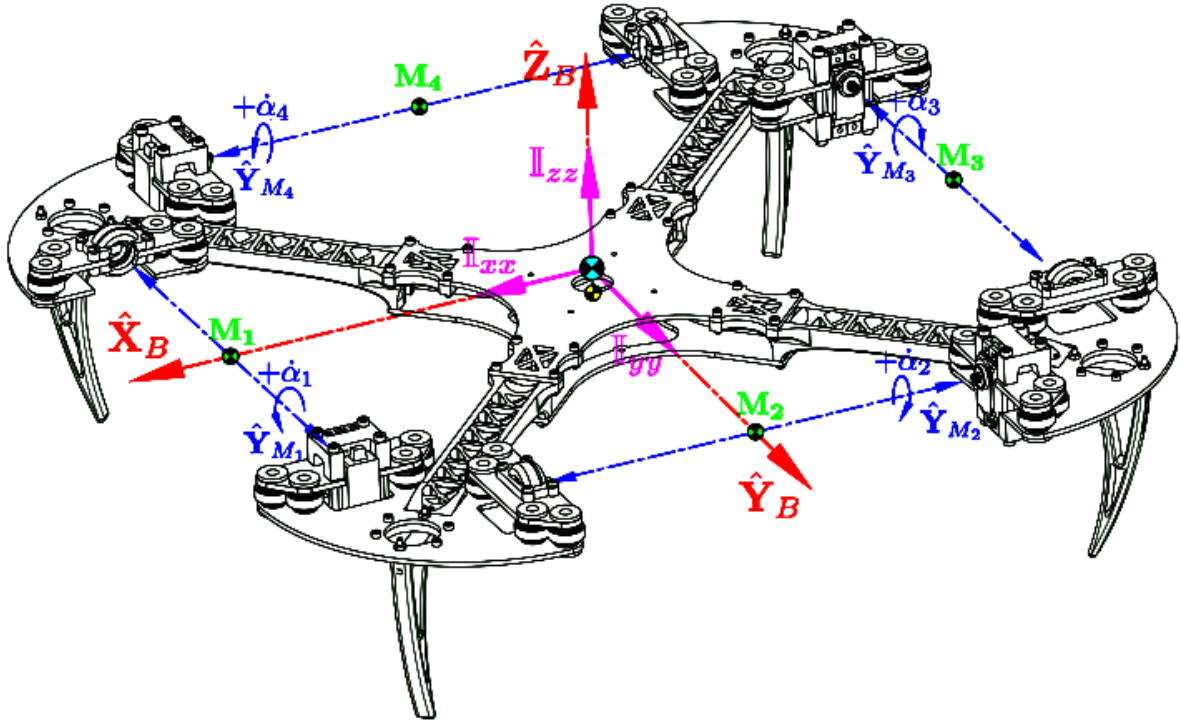
*It's at this stage that, despite simplifications, the symbolic inertial equations all become overly cumbersome to include with numeric values... For the sake of brevity, exact calculated inertial values for the input dependent plant are omitted.*

Each module's rotational center ( $\vec{L}_i = [\pm 195.16 \ 0 \ 0]$  or  $[0 \ \pm 195.16 \ 0]$  recalling Fig:2.8) are spaced equally relative to  $\vec{\mathbf{O}}_b$  with a parallel axis arm  $L_{arm} = 195.16 \text{ [mm]}$  (Fig:2.11). The net inertial equation about  $\vec{\mathbf{O}}_b$ , dependent on the actuator suite  $\mathbb{U}$  positions, can be calculated as:

$$\mathbb{I}_b(u) = \mathbb{I}_{body} + \sum_{u \in \mathbb{U}}_{i=1}^4 \mathbb{M}_i \text{ [kg.m}^2\text{]} \quad (2.16a)$$

<sup>9</sup>Disambiguation:  $\mathbb{I}_b$  is *net* body frame's inertia, different from  $\mathbb{I}_{body}$  which is the inertia for *just* the body structure

<sup>10</sup>Middle ring assembly inertia  $\mathbb{I}_{M'_i}$  defined in Eq:2.12b

**Figure 2.11:** Inertial center & mass center

$$\mathbb{M}_i = \mathbb{I}_{ith\ motor} + m_{module}(\vec{L}_i \cdot \vec{L}_i - \vec{L}_i \otimes \vec{L}_i) \quad (2.16b)$$

Although Eq:2.16 does indeed produce the net body's inertia, the transformations to calculate  $\mathbb{M}_i$  are cascaded. Motor module inertias are first translated to their centers of rotation from their respective center of masses and then finally to the body frame's origin. Subsequent transformations are successively going to deteriorate the floating point precision of the resultant inertial tensor. Transforming inertial tensors about each sub-body's center of mass directly to the body frame origin will improve the reliability and generality of the produced inertial equations. It is also perhaps more intuitive to consider each sub-body's contribution individually, despite having been derived as combined inertial systems previously.

$$\mathbb{I}_b(u) = \mathbb{I}_{body} + \sum_{i=1}^4 \mathbb{M}_{inner} + \sum_{i=1}^4 \mathbb{M}_{middle} \quad (2.17)$$

The relative movement pertinent to Eq:2.11 and Eq:2.12 are separate from those affecting Eq:2.16. For each inner ring, W.R.T its center of mass measured relative to its center of rotation, different from Eq:2.11a, the inner ring's inertia is calculated as;

$$m_{inner} = 92 \text{ [g]} \quad (2.18a)$$

$$\mathbb{I}_{inner} = \begin{bmatrix} 530.88 & -32.29 & 7.46 \\ -32.29 & 1855.74 & 0 \\ 7.46 & 0 & 2088.87 \end{bmatrix} \text{ [g.cm}^2\text{]} \quad (2.18b)$$

$$C.M_{inner} = [-1.44 \ 0 \ 5.81]^T \text{ [mm]} \quad (2.18c)$$

$$C.M'_{inner} = \mathbb{R}_z \mathbb{R}_y(\alpha_i) \mathbb{R}_x(\lambda_i) (C.M_{inner}) \quad (2.18d)$$

$$\mathbb{I}_{inner} \parallel \vec{\mathbf{O}} = \mathbb{R}_z \mathbb{R}_y(\alpha_i) \mathbb{R}_x(\lambda_i) (\mathbb{I}_{inner}) \mathbb{R}_x^{-1}(\lambda_i) \mathbb{R}_y^{-1}(\alpha_i) \mathbb{R}_z^{-1} \quad (2.18e)$$

$$\Delta L = \vec{L}_i - C.M'_{inner} \quad (2.18f)$$

$$\mathbb{M}_{inner} = \mathbb{I}_{inner} = \mathbb{I}_{inner} + m_{inner} ((\Delta L \cdot \Delta L) \mathbb{I}_{3x3} - \Delta L \otimes \Delta L) \quad (2.18g)$$

Similarly for the middle rings:

$$m_{middle} = 98 \text{ [g]} \quad (2.19a)$$

$$\mathbb{I}_{middle}^{C.M} = \begin{bmatrix} 2879.06 & 172.29 & 223.58 \\ 172.29 & 6268.97 & 13.33 \\ 223.58 & 13.33 & 8947.52 \end{bmatrix} \text{ [g.cm}^2\text{]} \quad (2.19b)$$

$$C.M_{middle} = [-47.00 \ 3.74 \ -3.63]^T \text{ [mm]} \quad (2.19c)$$

$$C.M'_{middle} = \mathbb{R}_z \mathbb{R}_y(\alpha_i)(C.M_{middle}) \quad (2.19d)$$

$$\mathbb{I}_{middle}^{||\vec{\mathbf{O}}} = \mathbb{R}_z \mathbb{R}_y(\alpha_i)(\mathbb{I}_{middle}) \mathbb{R}_y^{-1}(\alpha_i) \mathbb{R}_z^{-1} \quad (2.19e)$$

$$\Delta L = \vec{L}_i - C.M_{middle}' \quad (2.19f)$$

$$\mathbb{M}_{middle}^{||\vec{\mathbf{O}}} = \mathbb{I}_{middle}^{||\vec{\mathbf{O}}} = \mathbb{I}_{middle} + m_{middle}((\Delta L \cdot \Delta L) \mathbb{I}_{3x3} - \Delta L \otimes \Delta L) \quad (2.19g)$$

Unless otherwise specified; any inertia  $\mathbb{I}_b(u)$ , irrespective of arguments, will refer to an instantaneous calculated solution to Eq:2.17 given a particular  $u(t) \in \mathbb{U}$ . The purpose of the derivations Eq:2.18 & Eq:2.19 is twofold; highlighting both the inertial contributions and the variable center of masses for each sub-body. Seeing that the origin of the motion frame  $\mathcal{F}^b$  and the net body's center of mass aren't coincidental, it's important to quantify the equation for the center of mass position. If, for a collection of  $n$  bodies, with each body's center at some position  $\vec{X}_i$  and a mass  $m_i$ , the net center of mass<sup>†</sup> is:

$$C.M = \frac{\sum_{i=1}^n m_i \cdot \vec{X}_i}{\sum_{i=1}^n m_i} \quad (2.20a)$$

Such that, with  $\vec{X}_{inner}$  &  $\vec{X}_{middle}$  being rotated centers of mass defined in Eq:2.18d & Eq:2.19d respectively, the entire assembly has a center of mass<sup>†</sup>:

$$C.M(u) = \frac{m_{body} \cdot \vec{X}_{body} + \sum m_{inner} \cdot \vec{X}_{inner} + \sum m_{middle} \cdot \vec{X}_{middle}}{m_{body} + \sum m_{inner} + \sum m_{middle}} \quad (2.20b)$$

Making the resultant gravitational torque<sup>11</sup> about the origin  $\vec{\mathbf{O}}_b$  at any given moment:

$$\Delta C.G = \vec{\mathbf{O}}_b - C.M \quad (2.20c)$$

$$\tau_g = \Delta C.G \times \vec{G}_b \text{ [N.m]}, \tau_g \in \mathcal{F}^b \quad (2.20d)$$

The net mass for the whole assembly is 1574 g. For reference, the center of gravity when all actuators are at their zero positions is:  $C.M = [-0.02 \ -0.03 \ -4.5]^T \text{ [mm]}$ . Then, according to Eq:2.17, the inertial tensor for the net assembly at the rest conditions,  $u = \vec{0}$ , about the origin  $\vec{\mathbf{O}}_b$  is:

$$\mathbb{I}_b(\vec{0}) = \begin{bmatrix} 317784.78 & -0.42 & -6.46 \\ -0.42 & 317662.31 & -14.52 \\ -6.46 & -14.52 & 628430.75 \end{bmatrix} \text{ [g.cm}^2\text{]} \quad (2.21)$$

Finally rotational inertia of each propeller is incorporated into the inner ring's inertia, Eq:2.11. Individual propeller inertias are relevant later for gyroscopic torques, Eq:3.38c. For each propeller, having an angular velocity  $\Omega_i$  about its rotor  $\hat{Z}_{M_i}$  axis, and aligned with the module center of rotation 23.39mm below the propeller's own plane of rotation (Fig:2.3), the propeller's inertia is given as:

$$\mathbb{I}_p = \begin{bmatrix} x & y & z \\ x & y & z \\ x & y & z \end{bmatrix} \text{ [g.cm}^2\text{]} \quad (2.22)$$

---

<sup>11</sup>With  $\vec{G}_b = \mathbb{R}_I^b \vec{F}_g \text{ [N]}$

## 2.4 Electronics

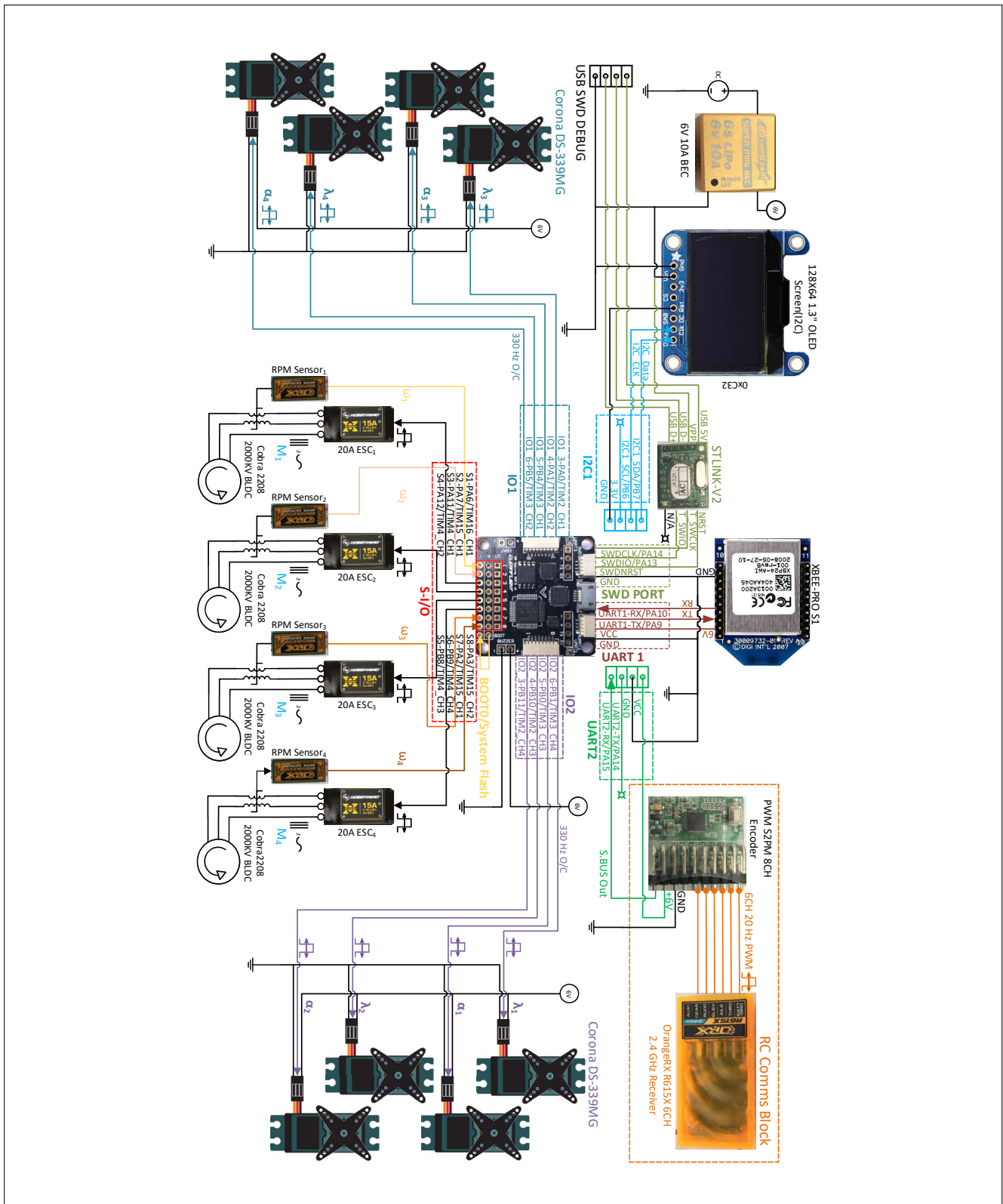
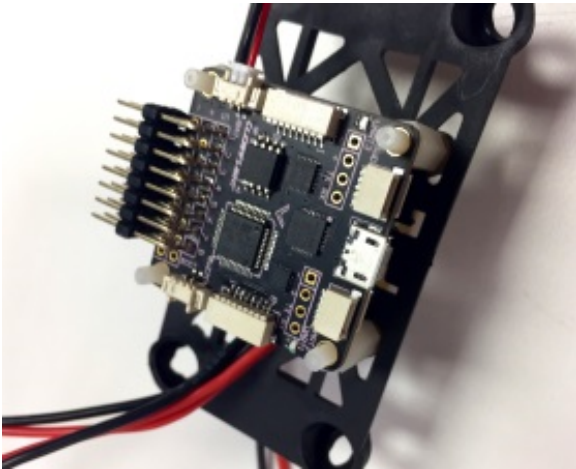
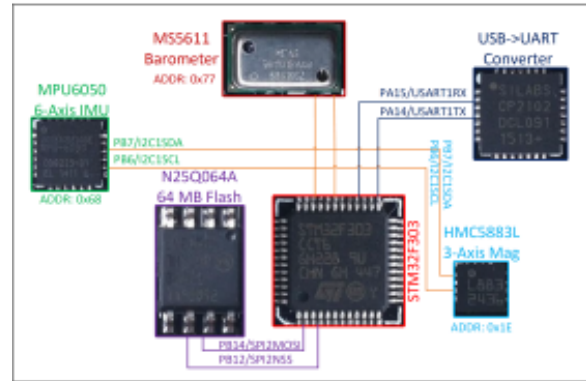


Figure 2.12: Hardware schematic diagram

An abstracted hardware diagram for the (electronic) system layout is shown in Fig:2.12. It's an illustration for the connection of different electronic peripherals used to aid the on-board control system. The structure of the implemented autopilot system and control loops are addressed later in Chapter:6. This section aims to provide a brief overview of the specific modules used, their purpose and a description of how they're interfaced. No code structure or control loops are considered yet...



(a) SPRacing F3 deluxe flight controller



(b) F3 Deluxe on-board connections

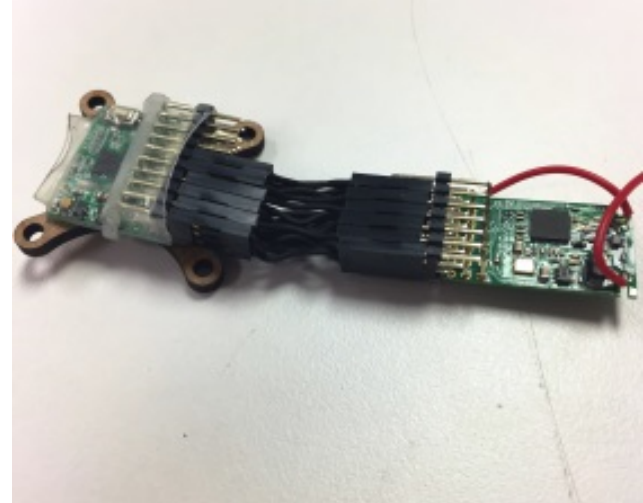
**Figure 2.13:** SPRacing F3 deluxe layout

The embedded system is constructed around an ARM STM32F303 [105] based  $\mu$ C. The microprocessor board is a commercial flight control board, specifically an SPRacing F3 Deluxe [24]<sup>12</sup>, which has had its bootloader removed and custom firmware, unique to this project, developed for it. That software is later described in Chapter:6; the I/O for all the peripherals are however detailed here. The flight-controller has the following onboard peripherals: an I2C MPU-6050 [47] 6-axis gyroscope & accelerometer with an I2C connected HMC5883 [30] magnetometer compass, an I2C MS5611 [103] barometer and finally 64 Mb of SPI flash memory. The electrical schematic diagram of those peripherals and the core STM32F303 microprocessor is detailed in Appendix:B.2 but their connection(s) and layout are shown in Fig:2.13.

*The combination of above sensors fused for state estimation and their associated filtration algorithms are dealt with in Section:5.3 of Chapter:5.*

Two separate wireless communication peripherals are used. First the system relays full state information, for a complete 6-DOF autopilot system, from a ground control station using 2.4 GHz XBEE S1 module(s) [48], connected via USART. Secondly, an augmented pilot control input system, fail safe and secondary to the autopilot loop, is transmitted through 6 Channel 2.4 GHz R/F comms. The 6 CH received signals, otherwise permeated as six individual 20 KHz PWM signals via an OrangeRx R615x [81] receiver, are encoded into a single proprietary S.BUS data stream (Fig:2.14).

The need for an S.BUS encoder [44] comes about as a consequence of the introduction of the 8 additional servos. As a result, there are no longer 6 free additional timer I/O channels which can be dedicated to input capture of those RC channels.

**Figure 2.14:** SBUS converter & 6CH receiver

<sup>12</sup>CleanFlight or BetaFlight opensource software is regularly used for the F3 but its hardware specifications are not openly available. The reverse engineered electrical schematic for the board is included in Appendix:B.2

Encoding the received data to a serial communication protocol means the 6CH data can be processed on a single serial RX line. The S.Bus encoder implements a USART derivative communications standard, Fig:2.15 shows the sampled data stream used to ascertain the standard's following parameters:

- 25 Bytes per packet
- 8-Bit byte length
- 1 Start byte 0x240
- 1 Byte of flags
- 1 Stop byte 0x0
- Bytes are:
  - MSB First
  - 1 start & 2 stop bits
  - Even parity bit
  - Inverted
  - $100000$  baud ( $b.s^{-1}$ )
- 22 bytes of CH data
- Each channel's data is 11 bits long
- 16CH encoded
- Channel data is little endian prioritized
- 14 ms idle time between packets
- Packets are arranged:

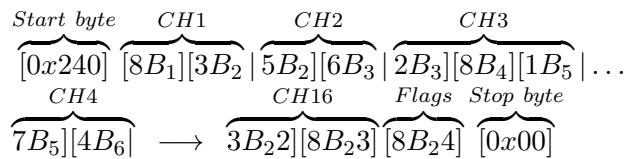


**Figure 2.15:** S.BUS data stream

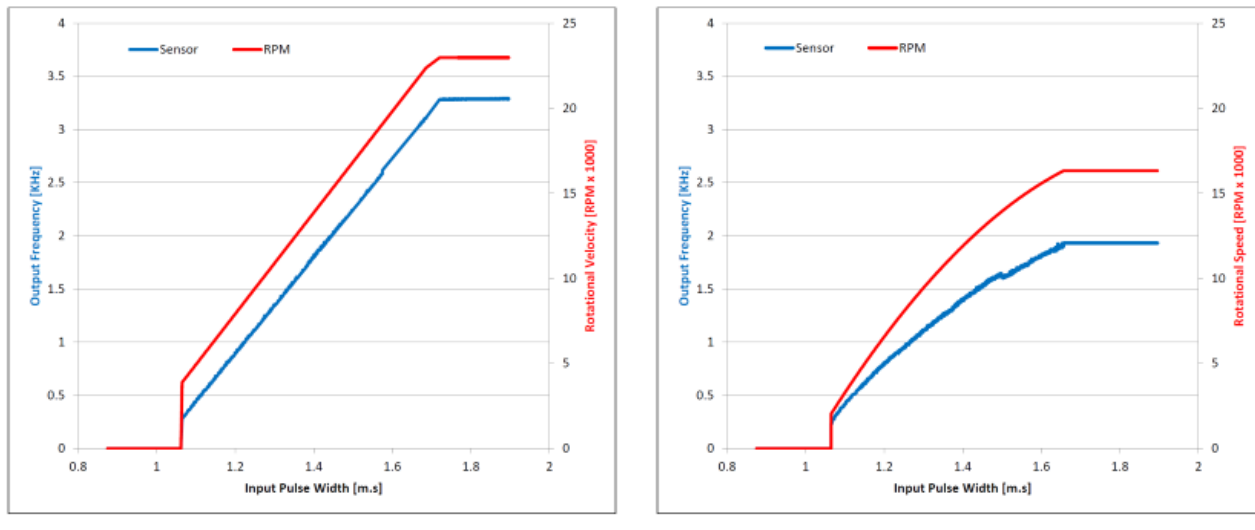
The received information from the transmitted 6 channels is filtered through a moving average IIR<sup>†</sup> filter. The filters difference equation is as follows:

$$y_n = \left(1 - \frac{1}{N}\right)y_{n-1} + \frac{1}{N}x_n \quad (2.23)$$

Moving over an average of  $N = 5$  samples. The signal's sample rate is sufficiently fast enough such that the digital filter's frequency response isn't of consequence. Similarly all the measured RPM signals are filtered as well. Any received signals referred to are all post filtration. Filtering for non-IMU state estimates is separately performed on the Ground Control Station computer.

Each of the eight digital servo actuators are driven individually from 330 Hz PWM timer output compare channels (TIM2:CH1→CH4 & TIM3:CH1→CH4). Output pulses typically range from 1ms - 2ms to linearly control the rotational position. The exact range and transfer function is empirically determined next in Subsection:2.4.1. The four 20A brushless DC speed controllers (ESCs) are each driven from a 20 Hz PWM output (TIM4:CH1→CH4), similarly with 1ms - 2ms input pulse widths. There are a total of 12 PWM output compare signals drawn from the  $\mu$ C. Servos are powered by a regulated 6V DC 10A power supply [43] whilst the ESCs switch unregulated 14.1 V DC from an externally tethered power supply. The DC supply could potentially be drawn from an on-board battery bank but that would add significant weight to an already heavy platform.

There's no integrated feedback for instantaneous RPM values from the ESCs. Using discrete OrangeRX BLDC RPM sensors [42], that measure switching phases across two of the three motor phases, the exact RPM can be ascertained.



(a) RPM sensor plot - no load

(b) RPM sensor plot - 6X4.5 prop

Figure 2.16: RPM sensor calibration plots

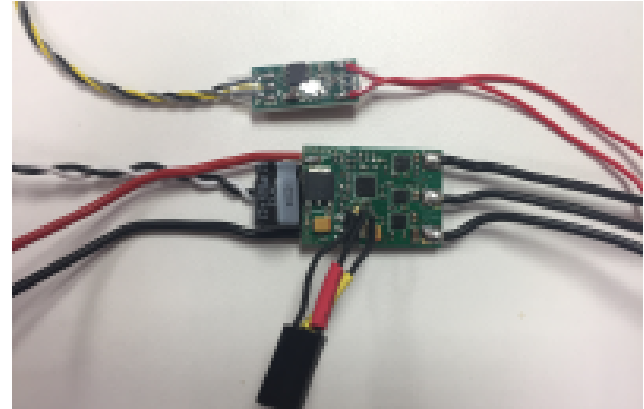
The switching signal of a 3-Phase induction motor<sup>13</sup> is [66]:

$$F_{rps} = \frac{2 \times F_{poles}}{\text{No. of rotor poles}} \quad [\text{Hz}] \quad (2.24)$$

The signal produced by the RPM sensors varies the period of a 50% duty cycle square wave, the wave frequency is directly proportional to that of the pole's switching frequency. The RPM sensor's output signal is then calibrated to a gain of 7 for the 14 pole BLDC Cobra motors used. That gain is verified with the linear relationship(s) is shown in Fig:2.16. Knowing exact RPM rates means the subsequent thrust and aerodynamic torques for the control plant inputs can be calculated.



(a) XRotor 20A ESC connection guide [41]



(b) LDPower 20A ESC with RPM sensor

Figure 2.17: BLDC electronic speed controllers

The speed controllers, although LDPower 20A devices, are all re-flashed with BLHeli<sup>14</sup> [11] firmware. The custom software on the ESC's  $\mu$ C can provide greater refinement over parameter configuration like the deflection range of inputs, however, default values were used. The plot in Fig:2.16a shows the linear RPS (in Hz) speed curve for an unloaded motor; similarly in Fig:2.16b shows the speed curve when loaded for a 6-inch prop.

<sup>13</sup>Although termed DC motors, BLDC motors are actually 3- $\phi$  IM motors which, combined with an ESC, behave like closed loop DC motors.

<sup>14</sup>LDPower 20A ESCs (Fig:2.17b) match Hobbywing Xrotor 20A speed controllers (Fig:2.17a), they both use SiLabs F396 MCUs. Physical rotational values in the plots Fig:2.16 were measured with optical encoders.

It's interesting to note that the loaded speed curve is slightly parabolic (Fig:2.16b), resulting from the aerodynamic drag term which is quadratic with respect to rotational velocity, expanded on in Sec:3.3.1. Moreover, when the motor is torque loaded by the propeller, the ESC current limits rotational speeds at just over 16 000 RPM. The sensor feedback is used for minor loop RPM control.

Timers channels are used to measure the varying frequency output from the RPM sensors. General purpose Timers 15 (TIM15:CH1→CH2), 16 (TIM16:CH1) and 17 (TIM17:CH1) are configured to capture the input PWM signal generated by the speed sensors. Included on the I2C communication line is an I2C O-LED display for debugging and status update purposes.

Any STM32  $\mu$ controller is programmed through a dedicated debugging device. The ST-Link V2 [104] is the current proprietary device which, itself, is a specially programmed STM32F10 chip. The chip connects to the dedicated **Serial Wire Debugging** ports of the target STM (*SWD-CLK*, *SWD-IO* & *SWD-NRST*) and is interfaced via regular USBD+ and USBD- data lines.

#### 2.4.1 Actuator Transfer Functions

##### Servo Transfer Functions

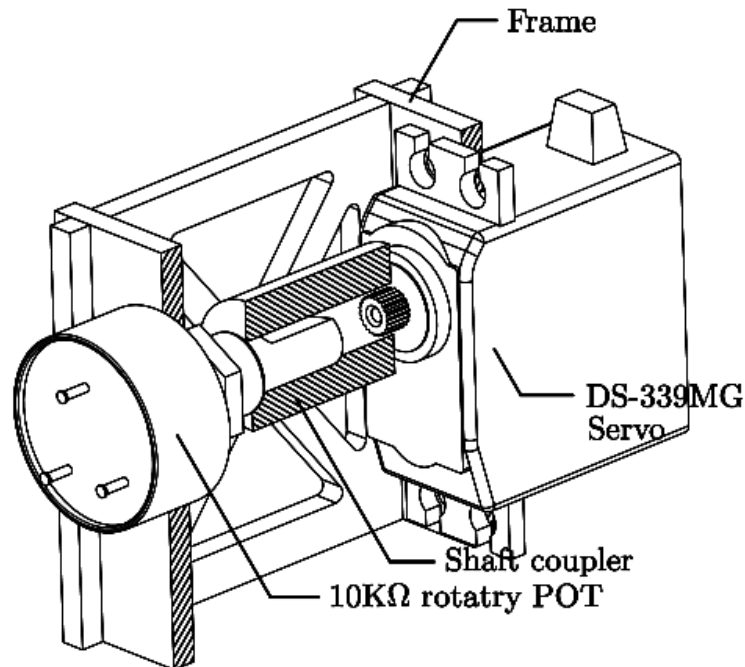


**Figure 2.18:** Servo transfer function test rig

The full scale deflection of each digital servo is in fact greater than its quoted 180° range. Each servo has a rotational range of around 230° (Fig:2.19a). The exact characteristics for every servo differ slightly and thus individual transfer functions for each of the 8 servos are used in simulation. In the prototype control loop the servos are left in open loop; the major loop controller coefficients are expected to account for minor loop actuator dynamics. With that being said, for such an expectation to be validated the simulation would need to accurately represent the servo's response.

Seeing that the 180° limitation was imposed as a design decision; one of the first points of contention is the effect such a constraint would have on the feasible operating trajectories. The control algorithms derived in Chapter:4 are first tested with an ideal, continuous rotation servo actuator with similar rate limits and transfer characteristics. Later the servo saturation limitations are introduced and the constraints to feasibly achievable trajectories are investigated.

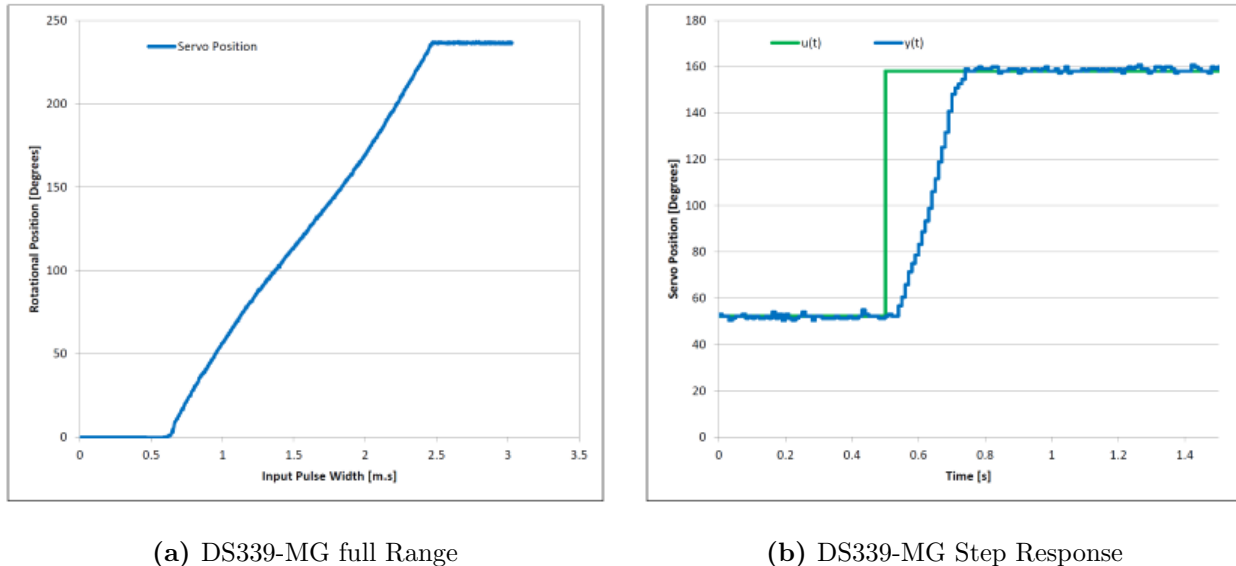


**Figure 2.19:** Unloaded servo transfer characteristics

For the servo<sup>15</sup> whose rotational range and step response are shown in Fig:2.19, the relationship between the input pulse-width  $x$  [m.s] and the rotational output position  $y$  degrees is given by:

$$y(x) = \begin{cases} 0^\circ & x < 0.65 \text{ m.s} \\ 129.12x - 82.64 & 0.64 \text{ m.s} \leq x \leq 2.46 \text{ m.s} \\ 230^\circ & x > 2.46 \text{ m.s} \end{cases} \quad (2.25)$$

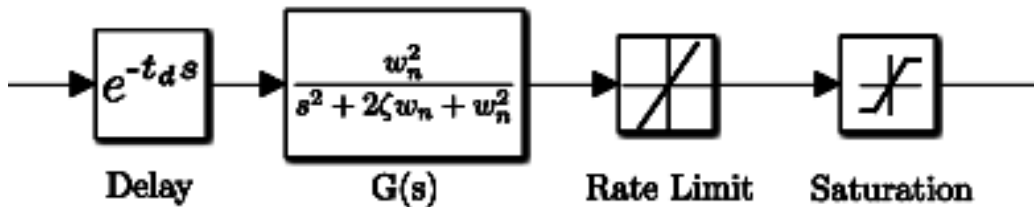


**Figure 2.20:** Servo block diagram

Although, in practice, the equation Eq:2.25 is changed such that  $0^\circ$  offset is taken at around a 50% input, making its operational range  $\pm 90^\circ$ . Each servo is mechanically rate limited to  $60^\circ/0.15s$  or  $400 \text{ RPS}$  with a dead time of  $\approx 1.2 \text{ m.s}$  and a mechanical deadband of  $\leq 4\mu\text{s}$ . The net transfer block for the servo is shown in Fig:2.20, including non-linearities but neglecting the deadband. Each servo has an approximate (*critically damped*) second order transfer function<sup>†</sup>:

$$G_{servo}(s) = e^{-t_{ds}} \frac{w_n^2}{s^2 + 2\zeta w_n s + w_n^2} = e^{-0.012s} \frac{(15.717)^2}{s^2 + 2(1)(15.717) + (15.717)^2} \quad (2.26a)$$

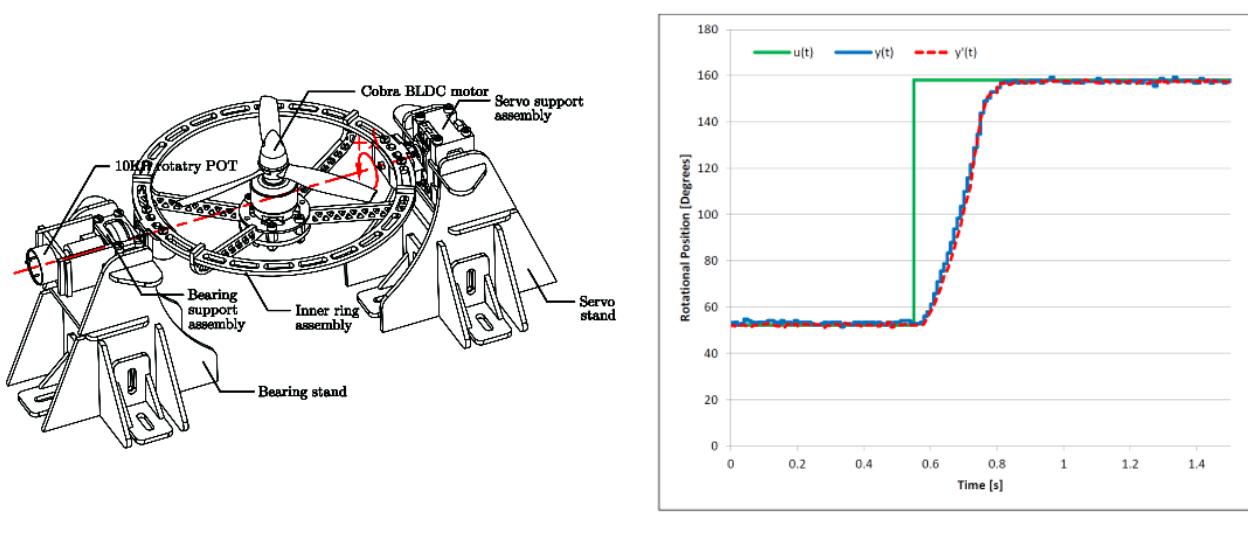
With saturation limits:

$$Y_{servo}(s) = \begin{cases} 0^\circ & |U(s)| < 0.65 \\ G(s) & 0.65 \leq |U(s)| \leq 2.46 \\ 230^\circ & |U(s)| > 2.46 \end{cases} \quad (2.26b)$$

The transfer plot in Fig:2.19b is that of an unloaded servo's response. When loaded with the inner ring assembly (Fig:2.21) the plant response  $y(t)$  is consistent with that of Eq:2.26. Despite rotating a load mass and hence requiring a greater torque, the servo's characteristics remains unchanged, even when the BLDC motor (with a  $6 \times 4.5"$  prop) is spun an average rate of 6500 RPM,  $y'(t)$ , further tensioning the assembly.

---

<sup>15</sup>Servo number 1 of 8 tested,  $\lambda_1$ , is used for transfer function demonstration. For simulation, each of the 8 servos were individually determined.

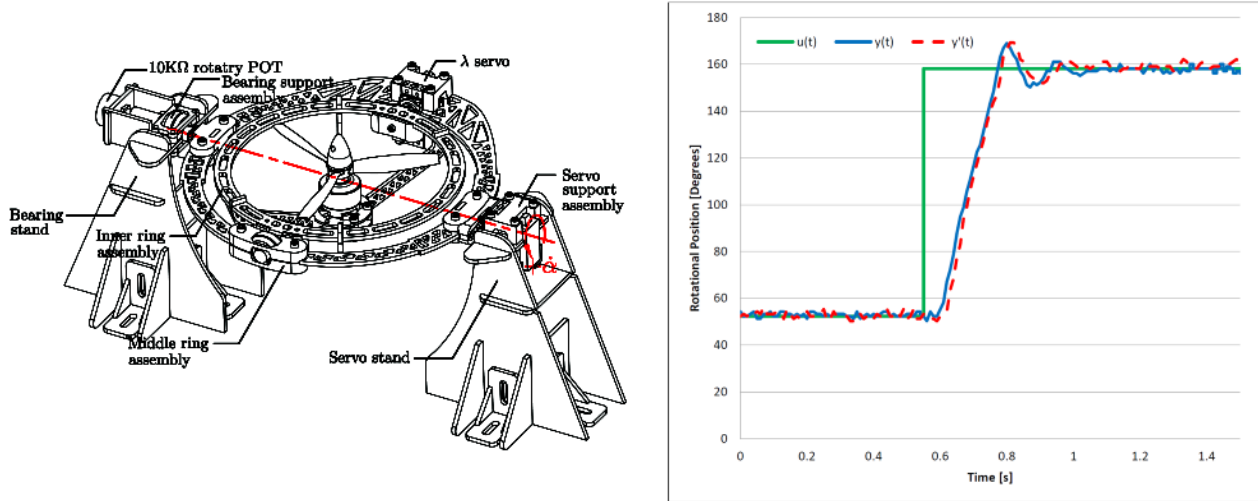


(a) Inner ring servo rig

(b) Servo response plot

**Figure 2.21:** Inner ring servo characteristics

However, in Fig:2.22, the response for a servo driving the middle ring is shown. Its rate transients remains the same but oscillations at the settling point are introduced by the larger mass being driven. These are product of the structure's flex within the middle ring assembly and *not from the servo plant*. The rotational position was measured (Fig:2.22a) with respect to the bearing supported output shaft, coaxial to the servos, and *not* the servo's output shaft. The oscillations are still present under load,  $y'(t)$ , despite the frame being further tensioned by a thrust vector. The mechanical harmonics can be accounted for by either introducing a more rigid sub-frame, limiting the maximum angular rate or applying a damping minor loop controller. The latter would require a *virtual* closed loop with an approximated error rate as the prototype structure doesn't incorporate positional feedback for each motor module.



(a) Middle ring servo test rig

(b) Servo response plot

**Figure 2.22:** Middle ring servo characteristics

## BLDC Transfer Functions

Each Cobra 2208 BLDC motor, when loaded with a  $6 \times 4.5$  propeller has a quadratic speed curve, Fig:2.24a. This is as a result of the propeller's opposing aerodynamic drag, *appromixately* proportional to the square of the propellers angular velocity (Sec:3.3.1).

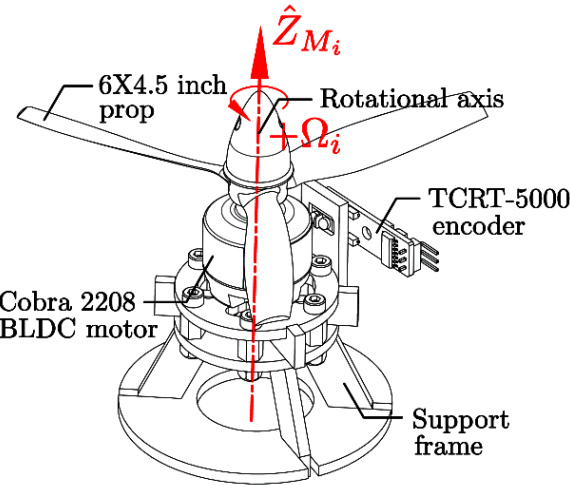


**Figure 2.23:** BLDC rpm speed calibration and transfer function rig

The relationship<sup>16</sup> between input pulse-width to the ESCs and output RPM sensor signal (Fig:2.24a) is:

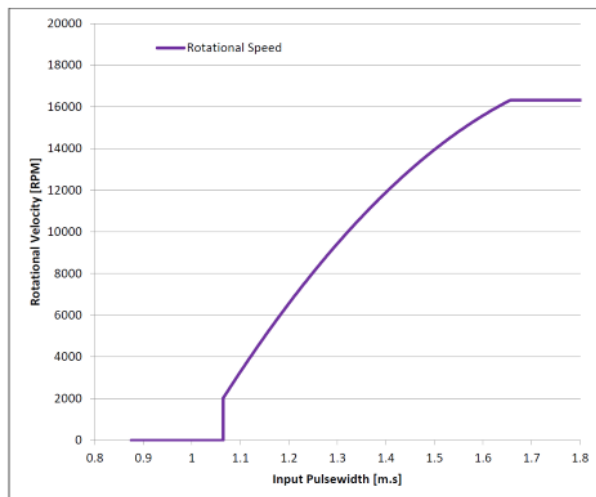
$$y(x) = \begin{cases} 0 & x < 1.065 \text{ m.s} \\ -20593x^2 + 80187x - 60004 & 1.065 \text{ m.s} \leq x \leq 1.655 \text{ m.s} \\ 16300^\circ & x > 1.655 \text{ m.s} \end{cases} \quad (2.27)$$

The upper limit in Eq:2.27 and the motor's step response are both governed by the ESC's maximum current limit; in this case 20A. Imposing 10A current limiting (a consequence of using lower power ESCs), the plot for  $c(t)$  in Fig:2.24b, significantly restricts the motor's transient and steady-state performance. The motor's step response,  $y(t)$  has a negligible dead time and 2<sup>nd</sup> order dynamics<sup>17</sup>, far faster than the servo's plant. The motors transfer function for speed in RPM is:

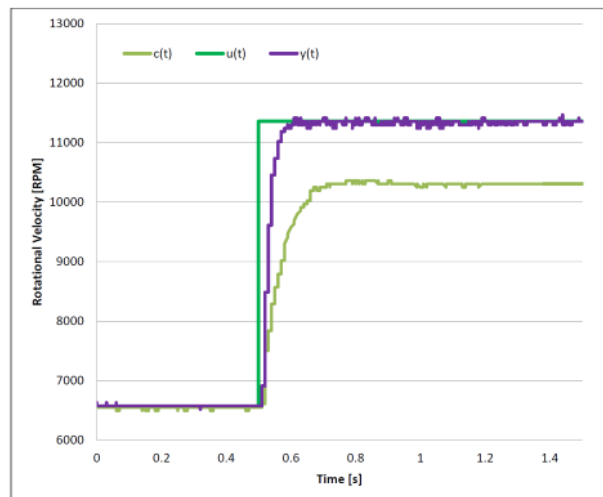
$$G_{BLDC}(s) = \frac{1}{(1 + 1.7583s \times 10^{-3})(1 + 1.7494s \times 10^{-3})} \quad (2.28a)$$

And saturation limits:

$$Y_{BLDC}(s) = \begin{cases} 0^\circ & |U(s)| < 1.065 \\ G(s) & 1.065 \leq |U(s)| \leq 1.655 \\ 16300 & |U(s)| > 1.655 \end{cases} \quad (2.28b)$$



(a) BLDC RPM range



(b) Cobra BLDC step response

**Figure 2.24:** BLDC motor characteristics

<sup>16</sup>The input range can be adjusted in BLHeli ESC software to improve input resolution, but was left unchanged.

<sup>17</sup>It can't be stressed enough how much the BLHeli ESC firmware improved dynamic response of the motors

# Chapter 3

## Kinematics & Dynamics

Generally applicable rigid body dynamics are first derived with respect to net forces and torques. Thereafter, those dynamics are adapted to the non-linear multibody case where constrained relative rotational motion between bodies is permitted. Following that, aerodynamic effects incorporated into the plant's model. Finally a consolidated, quaternion based plant model is presented which is used for the later control plant development next in Chapter:4.

### 3.1 Rigid Body Dynamics

#### 3.1.1 Lagrange Derivation

Fundamentally any body, rigid or otherwise, can undergo two kinds of movements, namely rotational and translation motions. Often a Lagrangian [90,109] approach for combined angular and translational movements is used to derive the differential equations of motion for each degree of freedom. The Lagrangian principle ensures that (translational and rotational) kinematic energies and potential energy are conserved throughout the system's trajectory progression. When combined with Euler-Rotational equations, the Euler-Lagrangian [111] formulation fully defines the aerospace 6-DOF equation set.

Lagrangian formalism is regarded as especially useful in non-cartesian (*spherical etc...*) co-ordinate frames or multi-body systems. With that being said, a cartesian co-ordinate system was already defined in Sec:2.2.2. Rigid body dynamics in a cartesian co-ordinate frame do lend themselves to Newtonian mechanics. The Newton-Euler or Euler-Lagrange formulations both stipulate the same resultant differential equations of motion. The Lagrangian operator,  $\mathcal{L}$ , is a term consisting of the difference between kinetic and potential energies,  $T$  and  $U$  respectively. Considering some generalized path co-ordinates  $\mathbf{r}(t)$ , for both position  $\vec{\mathcal{E}}$  and attitude  $\vec{\eta}$  relative co-ordinates;

$$\mathbf{r}(t) = \begin{bmatrix} \vec{\mathcal{E}} \\ \vec{\eta} \end{bmatrix} \quad (3.1)$$

The co-ordinates in Eq:3.1 are generalized here, despite being symbols commonly used to represent linear and attitude positions. The generalized co-ordinates are later be refined to Cartesian body co-ordinates with respect to the inertial frame. The Lagrangian is, by definition:

$$\mathcal{L}(\mathbf{r}, \dot{\mathbf{r}}, t) = T(\mathbf{r}, \dot{\mathbf{r}}) - U(\mathbf{r}, \dot{\mathbf{r}}) \quad (3.2a)$$

With kinetic and potential energy function(s)  $T$  and  $U$  respectively. Then introducing a rigid body's general (linear & angular) kinetic and potential energies, in some shared reference frame  $\mathcal{F}^x$ .

In this case the only potential energy is gravitational<sup>1</sup> potential energy:

$$\mathcal{L} = \frac{1}{2} \begin{bmatrix} \dot{\vec{\mathcal{E}}}^T(m) \dot{\vec{\mathcal{E}}} \\ \dot{\vec{\eta}}^T(\mathbb{I}_b) \dot{\vec{\eta}} \end{bmatrix} - \begin{bmatrix} m\vec{G}z \\ 0 \end{bmatrix} \quad (3.2b)$$

Noting that  $\mathbb{I}_b$  is the inertial tensor of the body aligned and translated w.r.t whichever reference frame is used. The Euler-Lagrange formulation equates partial derivatives of the Lagrangian to any generalized forces,  $\mathbf{V}$ , acting on the system. In this case the generalized forces are, more specifically, a net force  $\vec{F}_{net}$  and a net torque  $\vec{\tau}_{net}$ .

$$\frac{d}{dt} \left( \frac{\delta L}{\delta \dot{\mathbf{r}}} \right) - \frac{\delta L}{\delta \mathbf{r}} = \mathbf{V} = \begin{bmatrix} \vec{F}_{net} \\ \vec{\tau}_{net} \end{bmatrix} \quad (3.3)$$

Then taking the partial derivatives of Eq:3.2b with respect to the path co-ordinates  $\mathbf{r}$ :

$$\frac{\delta L}{\delta \mathbf{r}} = \begin{bmatrix} m\vec{G}_x \\ 0 \end{bmatrix} \quad (3.4a)$$

$$\frac{d}{dt} \left( \frac{\delta L}{\delta \dot{\mathbf{r}}} \right) = \left[ m \frac{d}{dt} \dot{\vec{\mathcal{E}}} \quad \mathbb{I} \frac{d}{dt} \dot{\vec{\eta}} \right]^T \quad (3.4b)$$

Where  $\vec{G}_x$  is the gravitation force in whichever reference frame ( $\mathcal{F}^x$ ) the Lagrangian is with respect to. In any generalized coordinate system a rotating vector's time derivative, according to the Reynolds Transportation Theorem [86], is given by:

$$\frac{d\vec{f}}{dt_a} = \frac{d\vec{f}}{dt_b} + \vec{\omega}_{a/b} \times \vec{f} \quad (3.5)$$

So applying that theorem (Eq:3.5) to the partial derivatives in Eq:3.4b and further defining the generalized co-ordinates as cartesian body coordinates with respect to an inertial origin (the body frame  $\mathcal{F}^b$  and inertial frame  $\mathcal{F}^I$ ). Noting that in Eq:3.4b the place holders used for linear ( $\vec{\mathcal{E}}$ ) and angular positions ( $\vec{\eta}$ ) all exist in a common shared frame<sup>2</sup>, and hence:

$$\frac{d}{dt} \begin{bmatrix} \vec{\mathcal{E}} \\ \vec{\eta} \end{bmatrix} \triangleq \begin{bmatrix} \vec{\nu} \\ \vec{\omega} \end{bmatrix} \in \mathcal{F}^b \quad (3.6)$$

It then follows that the Lagrangian Eq:3.2b changes to:

$$\mathcal{L} = \frac{1}{2} \begin{bmatrix} \vec{\nu}^T(m)\vec{\nu} \\ \vec{\omega}^T(\mathbb{I}_b)\vec{\omega} \end{bmatrix} - \begin{bmatrix} m\vec{G}_b z \\ 0 \end{bmatrix} \quad (3.7a)$$

$$\frac{d}{dt} \left( \frac{\delta L}{\delta \dot{\mathbf{r}}} \right) = \left[ m \frac{d}{dt} \vec{\nu} \quad \mathbb{I}_b \frac{d}{dt} \vec{\omega} \right]^T \quad (3.7b)$$

$$\rightarrow m \frac{d}{dt} \vec{\nu} = m \dot{\vec{\nu}} + \vec{\omega}_{I/b} \times \vec{\nu} \quad (3.7c)$$

$$\rightarrow \mathbb{I}_b \frac{d}{dt} \vec{\omega} = \mathbb{I}_b \dot{\vec{\omega}} + \vec{\omega}_{I/b} \times \mathbb{I}_b \vec{\omega} \quad (3.7d)$$

Which, when substituted back into the Euler-Lagrange formulation Eq:3.3, results in the familiar Newton-Euler equations for linear and angular differentials, both in the body frame;

$$\vec{F}_{net} = m\dot{\vec{\nu}} + \vec{\omega}_b \times m\vec{\nu} - m\mathbb{R}_I^b(-\eta)\vec{G}_I \quad (3.8a)$$

$$\vec{\tau}_{net} = \mathbb{I}_b \dot{\vec{\omega}}_b + \vec{\omega}_b \times \mathbb{I}_b \vec{\omega}_b \quad (3.8b)$$

It's important to recall that  $\vec{\omega}_b \neq \dot{\vec{\eta}}$  in the case where  $\vec{\eta} = [\phi \ \theta \ \psi]^T$ , seeing that Euler Angles are defined in sequentially rotated reference frames. So then four differential equations are often used to completely describe the entire set of state derivatives, namely:

$$\dot{\vec{\mathcal{E}}} = \mathbb{R}_b^I(-\eta)\vec{\nu} \quad \in \mathcal{F}^I \quad (3.9a)$$

$$\vec{F}_{net} = m\dot{\vec{\nu}} + \vec{\omega}_b \times m\vec{\nu} - m\mathbb{R}_I^b(-\eta)\vec{G}_I \quad \in \mathcal{F}^b \quad (3.9b)$$

---

<sup>1</sup>Here gravity is defined as;  $G = [0 \ 0 \ -9.81]^T \text{ m.s}^{-2}$  in the Inertial frame,  $\in \mathcal{F}^I$

<sup>2</sup>In this case  $\vec{\eta} \neq [\phi \ \theta \ \psi]^T$  seeing that the angular position  $\vec{\eta}$  is defined in a common frame.  $\vec{\eta}$  is NOT an Euler angle set.

$$\dot{\vec{\eta}} = \Psi(\eta)\vec{\omega}_b \quad \in \mathcal{F}^{v2,v1,I} \quad (3.9c)$$

$$\vec{\tau}_{net} = \mathbb{I}_b \dot{\vec{\omega}}_b + \vec{\omega}_b \times \mathbb{I}_b \vec{\omega}_b \quad \in \mathcal{F}^b \quad (3.9d)$$

The state differentials in Eq:3.9 can be reduced to a set of two equations. Those differentials are defined in the reference frames of the state variables which they represent. The non-linear form of those equations substitutes<sup>3</sup>  $d\vec{\eta}/dt = \Phi(\eta)\vec{\omega}_b$  into the Lagrangian derivative, Eq:3.4b.

$$\frac{d}{dt} \left( \frac{\delta \mathcal{L}}{\delta \dot{\mathbf{r}}} \right) = \left[ m \frac{d}{dt} \vec{\nu} \quad \mathbb{I}_b \frac{d}{dt} \dot{\vec{\eta}} \right]^T \Rightarrow \left[ m \frac{d}{dt} \vec{\nu} \quad \mathbb{I}_b \frac{d}{dt} \Phi(\eta) \vec{\omega}_b \right]^T \quad (3.10)$$

This only affects the angular component as the two kinetic energies are independent of one another. And so applying the differential chain rule yields:

$$\mathbb{I}_b \frac{d}{dt} \Phi(\eta) \vec{\omega}_b = \mathbb{I}_b (\Phi(\dot{\eta}) \vec{\omega}_b + \Phi(\eta) \dot{\vec{\omega}}_b) \quad (3.11)$$

Drawing from [78] and recognizing that  $\mathbb{I}_b$  must be transformed to the common intermediate Euler axes,  $\mathbb{J} = \Psi(\eta)^T \mathbb{I}_b \Psi(\eta)$ . The controllable differential equation for angular acceleration in Eq:3.8b, then in intermediate Euler frames for each angle, becomes<sup>4</sup>:

$$M(\eta) \ddot{\vec{\eta}} + C(\eta, \dot{\eta}) \dot{\vec{\eta}} = \Psi(\eta) \vec{\tau}_{net} \quad \in \mathcal{F}^{v2,v1,I} \quad (3.12a)$$

$$M(\eta) = \Psi(\eta)^T \mathbb{I}_b \Psi(\eta) \quad (3.12b)$$

$$C(\eta, \dot{\eta}) = -\Psi(\eta) \mathbb{I}_b \Psi(\dot{\eta}) + \Psi(\eta)^T [\Psi(\eta) \dot{\vec{\eta}}]_{\times} \mathbb{I}_b \Psi(\eta) \quad (3.12c)$$

The equation in Eq:3.12a fully describes the state derivative  $\ddot{\vec{\eta}}$  in its own reference frame(s). The two differential equations which describe the entire bodies motion are then:

$$\vec{F}_{net} = m \dot{\vec{\mathcal{E}}} + \mathbb{R}_b^I(-\eta) \vec{\omega}_b \times m \dot{\vec{\mathcal{E}}} - m \vec{G}_I \quad \in \mathcal{F}^I \quad (3.13a)$$

$$\vec{\tau}_{net} = \Psi(\eta)^{-1} M(\eta) \ddot{\vec{\eta}} + \Psi(\eta)^{-1} C(\eta, \dot{\eta}) \quad \in \mathcal{F}^{v2,v1,I} \quad (3.13b)$$

The generalized net forces effecting the system,  $\vec{F}(u)$  and  $\vec{\tau}(u)$ , are the system's controllable inputs and are going to be affected directly the systems actuators and their associated effectiveness function. In the general case, which is expanded upon in Sec:3.3, the control inputs are typically as follows. The net force acting on the system is simply the sum of all thrust vectors produced by rotating propellers  $T(\Omega_i)$ ;

$$\mu \vec{F} = \sum_{i=1}^4 \vec{T}(\Omega_i) \quad (3.14a)$$

Secondly the net torque is the sum of all differential torque arms produced from those propeller thrust vectors.

$$\mu \vec{\tau} = \sum_{i=1}^4 \vec{l}_i \times \vec{T}(\Omega_i) \quad (3.14b)$$

Where  $\vec{T}(\Omega_i)$  is the  $i^{th}$  motor's thrust vector typically fixed in the  $\hat{Z}_b$  axis direction. The thrust vectors could potentially be  $\in \mathbb{R}^3$ . Similarly  $\vec{l}_i$  is that thrust vector's perpendicular displacement from the origin  $\mathbf{O}_b$ . The above equations are still applicable to any 6 DOF body, common simplifications applied to the system(s) for quadrotor control are explored in Appendix:A.1. Aspects unique to (multibody) aerospace frames are now introduced. Obviously the contextual focus is on quadrotor and tilting quadrotor platforms...

<sup>3</sup>Originally introduced in Eq:2.5f

<sup>4</sup>The relationship  $\dot{\Phi} = \Phi \dot{\Psi} \Phi$  was used to simplify Eq:3.12, the singularity in  $\Phi$  still remains...

### 3.1.2 Rotation Matrix Singularity

The Euler Angle singularity is often mentioned but far less common is the demonstration of exactly how that singularity *mathematically* manifests itself. By definition, a singularity occurs when a loss of differentiability is encountered. In the case of a rotational 3-axis gimbal system(Fig:3.1a), when an intermediate sequenced rotational angle<sup>5</sup> is at  $\pi/2$  then the remaining two axes become co-linear (Fig:3.1b). That being both pitch  $\phi$  or yaw  $\psi$  rotations will subsequently have the same rotational effect. Such a situation results in what is termed as a loss of a degree of freedom.

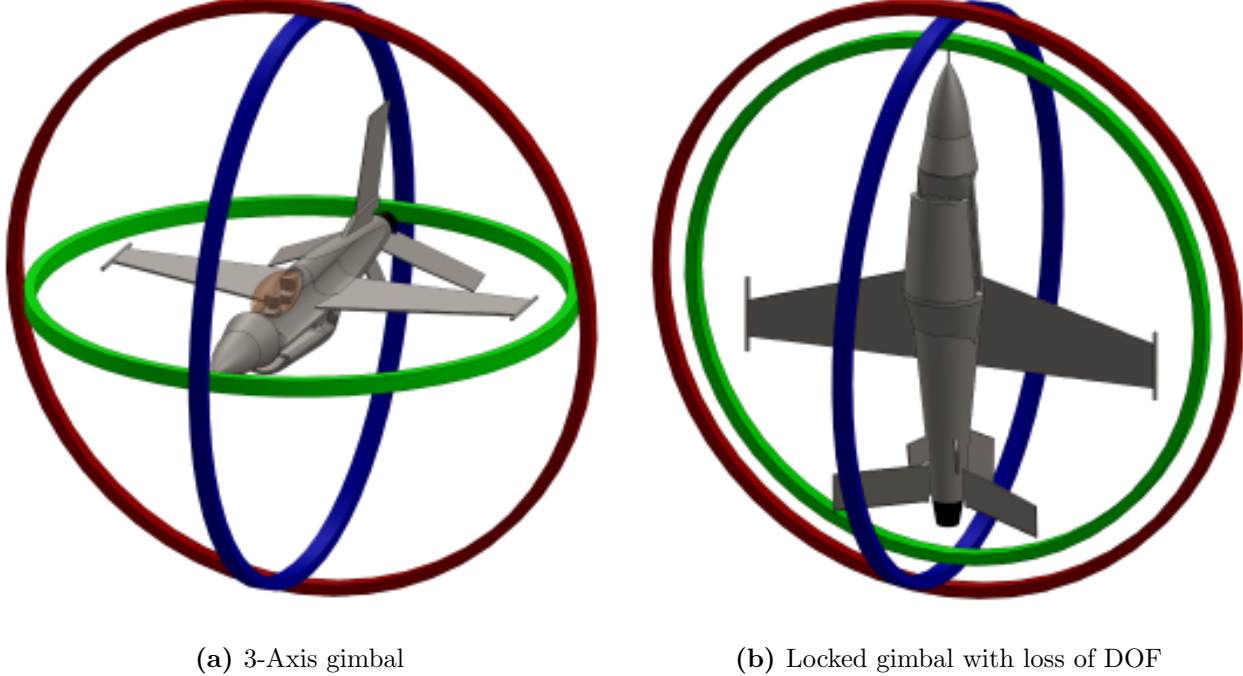


**Figure 3.1:** Mechanical gimbal lock

What is clear in the physical world is not necessarily as clear mathematically. An obvious loss of differentiability is present in the Euler Matrix  $\Psi(\eta)$ , defined previously in Eq:2.5f from Sec:2.2.1. That relation between angular velocity, in the inertial frame or inversely in the body frame, and the angular rates of the Euler Angles is dependent on singular secant and tangential terms.

$$\begin{bmatrix} \dot{\phi} \\ \dot{\theta} \\ \dot{\psi} \end{bmatrix} = \begin{bmatrix} 1 & \sin(\phi)\tan(\theta) & \cos(\phi)\tan(\theta) \\ 0 & \cos(\phi) & -\sin(\phi) \\ 0 & \sin(\phi)\sec(\theta) & \cos(\phi)\sec(\theta) \end{bmatrix} \begin{bmatrix} p \\ q \\ r \end{bmatrix} = \Phi(\eta)\omega_b \quad (3.15)$$

$$\text{As } \lim_{\theta \rightarrow \pi/2} \sec(\theta), \tan(\theta) \rightarrow \infty \quad (3.16)$$

Or that  $\Phi(\eta)$  is undefined at  $\theta = \pi/2$ . It's clear to see that in Eq:3.15 there exists an undefined singularity as  $\theta \rightarrow \pi/2$ . The physical consequence of this is the loss of a degree of freedom. More specifically, if one looks at how the Z-Y-X rotation (or transformation) matrices are formulated:

$$\mathbb{R}_I^b = \mathbb{R}_z \mathbb{R}_y \mathbb{R}_x = \begin{bmatrix} c_\psi & -s_\psi & 0 \\ s_\psi & c_\psi & 0 \\ 0 & 0 & 1 \end{bmatrix} \begin{bmatrix} c_\theta & 0 & s_\theta \\ 0 & 1 & 0 \\ -s_\theta & 0 & c_\theta \end{bmatrix} \begin{bmatrix} 1 & 0 & 0 \\ 0 & c_\phi & -s_\phi \\ 0 & s_\phi & c_\phi \end{bmatrix} \quad (3.17a)$$

$$\mathbb{R}_I^b = \begin{bmatrix} c_\psi c_\theta & c_\psi s_\theta s_\phi - s_\psi c_\phi & c_\psi s_\theta c_\phi + s_\psi s_\phi \\ s_\psi c_\theta & s_\psi s_\theta s_\phi + c_\psi c_\phi & s_\psi s_\theta c_\phi - c_\psi s_\phi \\ -s_\theta & c_\theta s_\phi & c_\phi c_\theta \end{bmatrix} \quad (3.17b)$$

<sup>5</sup>In Z-Y-X rotation sequence for example; the rolling angle  $\theta$ .

In the case where  $\theta = \pi/2$ , and using trigonometric double angles, the following can be reduced;

$$= \begin{bmatrix} 0 & c_\psi s_\phi - s_\psi c_\phi & c_\psi c_\phi + s_\psi s_\phi \\ 0 & s_\psi s_\phi + c_\psi c_\phi & s_\psi c_\phi - c_\psi s_\phi \\ -1 & 0 & 0 \end{bmatrix} = \begin{bmatrix} 0 & s(\phi - \psi) & c(\phi - \psi) \\ 0 & c(\phi - \psi) & s(\phi - \psi) \\ -1 & 0 & 0 \end{bmatrix} = \mathbb{R}_{x'}(\phi - \psi) \quad (3.17c)$$

Where the resultant in Eq:3.17c represents an  $\hat{X}'$ -axis rotation in a new intermediate frame, post a  $\pi/2$  rotation about the  $\hat{Y}$ -axis. Through trigonometric double angles a degree of freedom is lost at  $\theta = \pi/2$ , when  $\phi$  &  $\psi$  effect the same angle.

### 3.1.3 Quaternion Dynamics

An algorithm proposed in *How To Avoid a Singularity When Using Euler Angles?* [101] suggested a solution to the problem of Euler Angle singularities. The heuristic proposed was to switch between sequencing conventions (ZYX,ZYZ etc...there are 12 in total) such that the singularity is always avoided. However the implementation of such an algorithm is cumbersome and inefficient. Far more elegant is the use of *quaternion* attitude representations in  $\mathbb{R}^4$  ([36, 39, 59] amongst others...most notably made popular by Shoemake [1987] [100] for use in animation).

A quaternion is analogous to a rotation matrix in that it represents an attitude difference between two reference frames. An  $\mathbb{R}^3$  position is parameterized as one rotation  $\theta$  about a single unit *Euler axis*  $\hat{u}$  (sic Rodriguez Formula [72]). Without deliberating too much on their proof or details, a quaternion consists of a scalar component,  $q_0$ , and complex vector component,  $\vec{q} \in \mathbb{C}^3$ , such that;

$$Q \triangleq \begin{bmatrix} q_0 \\ \vec{q} \end{bmatrix} \in \mathbb{R}^4 \quad (3.18)$$

The relationship between an Euler Angles rotation matrix  $\mathbb{R}_I^b(\eta)$  and a quaternion attitude  $Q_b$  is given by the Rodriguez formula:

$$\mathbb{R}_I^b(\eta) = \mathbb{R}(Q_b) = \mathbb{I} + 2q_0[\vec{q}]_{\times} + 2[\vec{q}]_{\times}^2 \quad (3.19)$$

Any and all quaternions, unless otherwise stated, in this dissertation are unit quaternions<sup>6</sup>,  $Q \in \mathbb{Q}_u$ . The need for quaternions with unity magnitude is such to ensure rotational operations don't affect the magnitude of the vector operand. A unit quaternion is defined as:

$$\|Q\| = \sqrt{q_0^2 + \vec{q}^2} = 1 \quad (3.20)$$

Quaternion multiplication is distributive and associative, but not commutative. Specifically a quaternion multiplication operation is equivalent to the Hamilton product. For two quaternions,  $Q$  &  $P$ :

$$Q \otimes P = \begin{bmatrix} q_0 \\ \vec{q} \end{bmatrix} \otimes \begin{bmatrix} p_0 \\ \vec{p} \end{bmatrix} \quad (3.21a)$$

$$= q_0 p_0 - \vec{q} \cdot \vec{p} + p_0 \vec{q} + q_0 \vec{p} + \vec{q} \times \vec{p} \quad (3.21b)$$

Seeing that the vector component of a quaternion is complex valued, it is natural that there exists a quaternion conjugate property. Namely:

$$Q^* = \begin{bmatrix} q_0 \\ -\vec{q} \end{bmatrix} \quad (3.22)$$

It then follows that<sup>7</sup> the fundamental quaternion identity is:

$$Q \otimes Q^* = \mathbb{I}_{4 \times 4} \quad (3.23)$$

---

<sup>6</sup>Unit quaternions are a subset of the quaternion space

<sup>7</sup>Disambiguation:  $\mathbb{I}$  in this context is a  $4 \times 4$  identity matrix, not an inertial matrix

Application of a right handed quaternion rotation to a vector  $\vec{v} \in \mathbb{R}^3$  involves multiplication by two unit quaternions.

$$\begin{bmatrix} 0 \\ \vec{v}' \end{bmatrix} = Q \otimes \begin{bmatrix} 0 \\ \vec{v} \end{bmatrix} \otimes Q^* \quad (3.24)$$

Mostly, the zero scalar components are omitted in a rotation (*or transformation*) operation, as such it is implied vector operands are substituted with quaternions.

$$\vec{v}' = Q \otimes (\vec{v}) \otimes Q^* \quad (3.25)$$

In the case of rigid body attitude representation,  $Q_b$  is the quaternion which represents the difference between  $\mathcal{F}^b$  and  $\mathcal{F}^I$ . A quaternion operator is equivalent to a rotation matrix operation:

$$\mathbb{R}_I^b \underset{Q}{\iff} Q_b \otimes (\cdot) \otimes Q_b^* \quad (3.26)$$

A Z-Y-X sequenced<sup>8</sup> body quaternion,  $Q_b$ , can be constructed from Euler angles as:

$$Q_b = Q_z \circ Q_y \circ Q_x = \begin{bmatrix} \cos(\psi/2) \\ 0 \\ 0 \\ \sin(\psi/2) \end{bmatrix} \otimes \begin{bmatrix} \cos(\theta/2) \\ 0 \\ \sin(\theta/2) \\ 0 \end{bmatrix} \otimes \begin{bmatrix} \cos(\phi/2) \\ \sin(\phi/2) \\ 0 \\ 0 \end{bmatrix} \quad (3.27)$$

A quaternion time derivative, with  $Q_\omega$  being a quaternion with a vector component equal to angular velocity  $\vec{\omega}_{b/I}$  and a zero scalar component, is given by:

$$\frac{d}{dt} Q_b = \frac{1}{2} Q_b \otimes Q_\omega = \begin{bmatrix} -\frac{1}{2} \vec{q}^T \vec{\omega}_b \\ \frac{1}{2} ([\vec{q}]_\times + q_0 \mathbb{I}) \vec{\omega}_b \end{bmatrix} \quad (3.28)$$

Using quaternions to represent attitudes negates the need for an Euler Matrix,  $\Phi(\eta)$ , to represent attitudes and their rates. A body quaternion is fully defined in the inertial frame with respect to the body frame or inversely so. The first quaternion time derivative replaces Eq:3.9a & Eq:3.9c;

$$\dot{Q} = \mathbb{R}_b^I(-\eta) \vec{v} \underset{Q}{\iff} Q_b(-\eta) \otimes \vec{v} \otimes Q_b(-\eta)^* = Q_b^* \otimes \vec{v} \otimes Q_b \quad \in \mathcal{F}^I \quad (3.29a)$$

$$\dot{\eta} = \Phi(\eta) \vec{\omega}_b \underset{Q}{\iff} \dot{Q} = \frac{1}{2} Q_b \otimes Q_\omega \quad \in \mathcal{F}^{v2,v1,I} \quad (3.29b)$$

Second order time derivatives for quaternion acceleration aren't as useful or concise as their higher order velocity counterparts. The second order derivative is provided here however it's only relevant to quaternion backstepping later in the control chapter. If possible, quaternion accelerations are mostly avoided due to the complexity of their evaluation;

$$\ddot{Q}(\dot{Q}, Q, t) = \dot{Q} \otimes Q^* \otimes \dot{Q} + \frac{1}{2} Q \otimes [\mathbb{I}_b^{-1}(\tau - 4(Q^* \otimes \dot{Q}) \times (\mathbb{I}_b(Q^* \otimes \dot{Q})))] \quad (3.30)$$

### 3.1.4 Quaternion Unwinding

Although quaternions are indeed better than Euler angles, lacking the associated singularity, they do contain one caveat. Seeing that a quaternion  $Q = [q_0 \vec{q}]^T$  represents an attitude orientation of a body in  $\mathbb{R}^3$  using  $\mathbb{R}^4$  variables there exists what is called a dual coverage [72]. Each unit quaternion, stemming from Euler-Rodriguez theorem, is parametrized such that the quaternion operation represents a single Euler-axis rotation of  $\theta$  about a unit axis  $\hat{u}$  such that:

$$Q = \begin{bmatrix} q_0 \\ \vec{q} \end{bmatrix} = \begin{bmatrix} \cos(\theta/2) \\ \sin(\theta/2) \hat{u} \end{bmatrix} \quad (3.31)$$

---

<sup>8</sup>The resultant quaternion rotational products are sequence independent, but the quaternions rotational trajectories do depend on the sequence used. Here they are sequenced following the order of the rotational Euler angles used as arguments.

That rotation is applied with a quaternion operator Eq:3.25. It then follows that for each unique attitude in 3-Dimensions there exist two quaternions which correlate to the same position, differing by their rotational direction about the Euler-axis. Seeing that  $\theta = 2\pi - \theta^9$ , then there are two definitions for  $Q_b$ :

$$Q_b = \begin{bmatrix} q_0 \\ \vec{q} \end{bmatrix} = \begin{bmatrix} \cos(\theta/2) \\ \sin(\theta/2)\hat{u} \end{bmatrix} \quad (3.32a)$$

$$Q = \begin{bmatrix} \cos(\pi - \theta/2) \\ \sin(\pi - \theta/2)\hat{u} \end{bmatrix} = \begin{bmatrix} -\cos(\theta/2) \\ \sin(\theta/2)\hat{u} \end{bmatrix} \quad (3.32b)$$

$$\eta \in \mathbb{R}^3 \iff_Q \begin{bmatrix} \pm q_0 \\ \vec{q} \end{bmatrix} \in \mathbb{R}^4 \quad (3.32c)$$

The conjecture in Eq:3.32c is that for each physical attitude in  $\mathbb{R}^3$  there are two corresponding quaternions in  $\mathbb{R}^4$ ;  $[\pm q_0 \ \vec{q}]^T$ . A consequence of this is two possible error state trajectories for every attitude difference. Both a clockwise  $\theta$  rotation and an anticlockwise  $2\pi - \theta$  negative rotation will point to the same quaternion error state. This could lead to an erroneous and unnecessary "unwinding" of a complete counter revolution as a result of a dual covered error state.

Often the signed scalar component of the attitude quaternion error (Sec:4.4.1) is simply neglected or assumed positive. As such for attitude controllers the requirement is that for positive and negative scalars the control input is consistent:

$$\nu_d = h([q_0 \ \vec{q}]^T, t) = h([-q_0 \ \vec{q}]^T, t) \quad (3.33)$$

Or more simply that  $Q_e = [|q_0| \ \vec{q}]^T$ . The most simple solution adhering to that constraint, which control designers often adopt, is to simply neglect the scalar component altogether. The adjustment is to use a simplified error state argument for the control law;  $h(\vec{q}_e, t)$ . Such a solution is an oversimplification and would only ever be asymptotically stable in the local and not global regions.

An alternative solution is using an only positive quaternion scalar, one that will always ensure that an error state represents a right-handed clockwise rotation and not necessarily the most direct rotation trajectory. If the resolution of trajectory co-ordinates generated is sufficiently high enough, the control plant will however never encounter a problem. One proposal in *Nonlinear Quadcopter Attitude Control* [20] suggested using a *signum* operator to design the signs of the controller coefficients for the virtual control plant input.

$$\vec{\omega}_d = \frac{2}{\tau} sgn(q_0) \vec{q} \quad (3.34a)$$

$$sgn(\vec{q}) = \begin{cases} 1 & \vec{q} \geq 0 \\ -1 & \vec{q} < 0 \end{cases} \quad (3.34b)$$

The resultant *hybrid* mode controller provides global asymptotic stability, but only in the case that the Euler-axis angle  $\theta \leq \pm\pi$ . The control law described in Eq:3.34 would still need the control torques to be designed from that angular velocity virtual control setpoint.

Another proposal [72] to the unwinding problem was to lift the quaternion error-state back into  $\mathbb{R}^3$  using the Rodriguez formula, Eq:3.19. The mapping back to  $\mathbb{R}^3$  effectively ensures that  $\theta$  is minimized, or that the error-state imposes the shortest possible rotation between the reference and desired body frames. Controllers presented in Sec:4.4 all incorporate the signed quaternion scalar into the control law; hence relying on the trajectory generation to provide the desired direction of the rotation path.

## 3.2 Multibody Nonlinearities

Typically multibody dynamics are solved (and simulated) as a series of torque & force interactions or responses. There are many different schools of thought on the subject which each have proposed various

---

<sup>9</sup>Disambiguation:  $\theta$  is not the  $\hat{Y}$ -axis Euler angle here...

methodologies for stepping through the systems dynamics [sic Implicit Euler [54,117] or otherwise . . .]. For the prototype design here, only relative rotational motion is permissible between the interconnected rigid bodies. Each body is considered independently, as free and rigid, whose constraint torques induced from excitation are imposed onto sequential rotational joints. Opposed to those torques are Newtonian responses of importance which manifest as what are termed *gyroscopic* and *inertial* torques. Those responses are now quantified and introduced into the dynamic model derived in Sec:3.1.1. By the nature of the design there can be no unbalanced constraining forces existing between each body and as such the translational model is regarded as rigid.

A distinction must be made between torque responses here and those of Eq:3.9d. The latter being a response to be diminished in feedback compensation and the former being something which is later exploited by the control allocation algorithm in a feedforward type configuration, Sec:4.6. The multibody analysis which follows is a very Newtonian approach in that each body involved is resolved independently and relative responses are transferred onto the inducing body. The alternative numeric solution is to form a Lagrangian for the entire dynamic system, this would simplify solving net effects. Such an approach is unused here as each individual effect needs to be quantified if they're to be used as potential actuator inputs.

### 3.2.1 Relative Rotational Gyroscopic & Inertial Torques

The torque responses induced from relative rotations, the only permissible intra-body movement, are transferred from the interacting bodies as a result of Newtons second law of rotational motion. For each of the motor modules' pitching or rolling motion, the respective servo motors apply some torque to invoke that rotation. Opposed to the rotational motion are both inertial and gyroscopic response(s) of that body being acted upon. The latter being a consequence of a vector's time derivative in a rotating frame, Eq:3.5.

Each of the four motor modules are symmetrical and as such the induced torque response characteristics for one module can be extrapolated through a reference frame rotation. Seeing that each relative rotation from the actuator set  $u \in \mathbb{U}$  is actuated independently and upon a different body, their responses are calculated separately too.

Drawing again from Lagrangian theory<sup>10</sup> and considering only the rotational kinetic energy for the inner ring assembly  $\mathcal{F}^{M_i}$ . There are no permissible transnational motions between each body and as such there can be no linear kinetic energy contribution. The Lagrangian for the inner ring is formed, with concern on the effect  $\lambda_i$  has on the system:

$$\mathcal{L}_{M_i} = \frac{1}{2} \vec{\Omega}_i^T (\mathbb{I}_p) \vec{\Omega}_i + \frac{1}{2} \dot{\vec{\lambda}}_i^T (\mathbb{I}_\lambda) \dot{\vec{\lambda}}_i \quad (3.35)$$

Where  $\mathbb{I}_p$  is the propeller's rotational inertia, Eq:2.22, and  $\mathbb{I}_\lambda$  being the inner ring's inertia, defined in Eq:2.11a. Noting that  $\vec{\Omega}_i = [0 \ 0 \ \Omega_i]^T \in \mathcal{F}^{M_i}$  and  $\dot{\vec{\lambda}}_i = [\dot{\lambda}_i \ 0 \ 0]^T \in \mathcal{F}^{M'_i}$ , the two contributors are not in a common frame. As such the equation<sup>11</sup> changes to:

$$\mathcal{L}_{M_i} = \frac{1}{2} \vec{\Omega}_i^T (\mathbb{I}_p) \vec{\Omega}_i + \frac{1}{2} \dot{\vec{\lambda}}_i'^T (\mathbb{I}_\lambda) \dot{\vec{\lambda}}_i' \quad (3.36a)$$

$$\dot{\vec{\lambda}}_i' = Q_x(-\lambda_i) \otimes (\dot{\vec{\lambda}}_i) \otimes Q_x^*(-\lambda_i) \Rightarrow \dot{\vec{\lambda}}_i' = \dot{\vec{\lambda}}_i \quad (3.36b)$$

Where both  $\mathbb{I}_p$  and  $\mathbb{I}_\lambda$  are taken W.R.T to their rotational centre(s).

---

<sup>10</sup>The generalized linear kinetic energy for each module is an extension of that in Eq:3.13a and is independent of any of the actuator positions.

<sup>11</sup>The transformation of  $\dot{\vec{\lambda}}_i \rightarrow \dot{\vec{\lambda}}_i'$  is superfluous but included for completeness.

Then recalling the Euler-Lagrange formulation from Eq:3.3 with generalized co-ordinates<sup>12</sup>  $\mathbf{u}(t)$  for the motor module frame,  $\mathcal{F}^{M_i}$ , relative to the body frame,  $\mathcal{F}^b$ .

$$\frac{d}{dt} \left( \frac{\delta L}{\delta \dot{\mathbf{u}}} \right) - \frac{\delta L}{\delta \mathbf{u}} = \mathbf{V} = \vec{\tau}_{net} \quad (3.37)$$

It then follows that:

$$\frac{d}{dt_b} \left( \frac{\delta \mathcal{L}}{\delta \dot{\mathbf{u}}} \right) = \frac{d}{dt_{M_i}} \mathbb{I}_p \vec{\Omega}_i + \vec{\omega}_{M_i/b} \times \mathbb{I}_p \vec{\Omega}_i + \frac{d}{dt_{M_i}} \mathbb{I}_\lambda \dot{\vec{\lambda}}_i + \vec{\omega}_{M_i/b} \times \mathbb{I}_\lambda \dot{\vec{\lambda}}_i \quad (3.38a)$$

With  $\vec{\omega}_{M_i/b}$  being the net angular velocity of the inner ring frame relative to the body frame. Both inner and middle ring servo rates,  $d\vec{\lambda}_i/dt$  &  $d\vec{\alpha}_i/dt$  respectively, contribute to that inner ring's relative angular velocity:

$$\vec{\omega}_{M_i/b} = Q_x(-\lambda_i) Q_y(-\alpha_i) \otimes \dot{\vec{\alpha}}_i \otimes Q_y^*(-\alpha_i) Q_x^*(-\lambda_i) + Q_x(-\lambda_i) \otimes \dot{\vec{\lambda}}_i \otimes Q_x^*(-\lambda_i) \quad (3.38b)$$

The net torque from a  $\lambda_i$  rotation, induced in the motor module frame  $\mathcal{F}^{M_i}$ , can be grouped into second order *Inertial* and first order *Gyroscopic* components. Depending on the fidelity of the model or aggressiveness of control actions taken, higher order induced terms could be ignored to save computational complexity.

$$\vec{\tau}_\lambda = \underbrace{\mathbb{I}_p \dot{\vec{\Omega}}_i + \mathbb{I}_\lambda \ddot{\vec{\lambda}}_i}_{Inertial} + \underbrace{\vec{\omega}_{M_i/b} \times \mathbb{I}_p \vec{\Omega}_i + \vec{\omega}_{M_i/b} \times \mathbb{I}_\lambda \dot{\vec{\lambda}}_i}_{Gyroscopic} \in \mathcal{F}^{M_i} \quad (3.38c)$$

Similarly for the middle ring, with the inertia,  $\mathbb{I}_\alpha(\lambda_i)$ , as a function of the inner ring rotation angle,  $\lambda$ , from Eq:2.12c. Using a new set of generalized co-ordinates,  $\mathbf{v}(t)$ , for the middle ring frame,  $\mathcal{F}^{M'_i}$ , relative to the body frame, the Lagrangian is then:

$$\mathcal{L}_{M'_i} = \frac{1}{2} \dot{\vec{\alpha}}_i^T (\mathbb{I}_\alpha(\lambda_i)) \dot{\vec{\alpha}}_i \quad (3.39a)$$

$$\frac{d}{dt_b} \left( \frac{\delta L}{\delta \dot{\mathbf{v}}} \right) = \frac{d}{dt_{M'_i}} \mathbb{I}_\alpha(\lambda_i) \dot{\vec{\alpha}}_i + \vec{\omega}_{M'_i/b} \times \mathbb{I}_\alpha(\lambda_i) \dot{\vec{\alpha}}_i \quad (3.39b)$$

$$\vec{\omega}_{M'_i/b} = Q_y(-\alpha_i) \otimes \dot{\vec{\alpha}}_i \otimes Q_y^*(\alpha_i) \quad (3.39c)$$

Which are similarly grouped into first and second order gyroscopic and inertial components.

$$\vec{\tau}_\alpha(\lambda_i) = \underbrace{\mathbb{I}_\alpha(\lambda_i) \ddot{\vec{\alpha}}_i}_{Inertial} + \underbrace{\vec{\omega}_{M'_i/I} \times \mathbb{I}_\alpha(\lambda_i) \dot{\vec{\alpha}}_i}_{Gyroscopic} \in \mathcal{F}^{M'_i} \quad (3.39d)$$

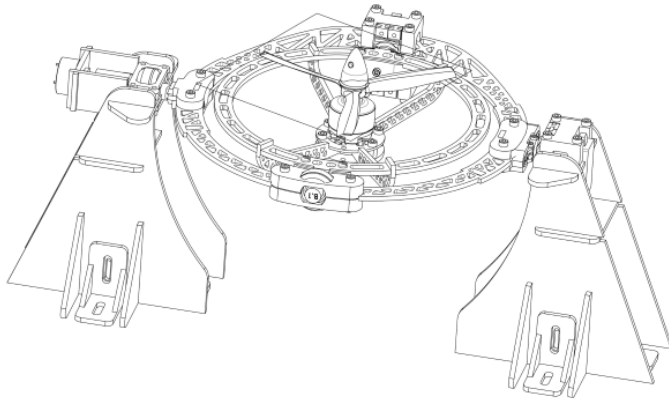


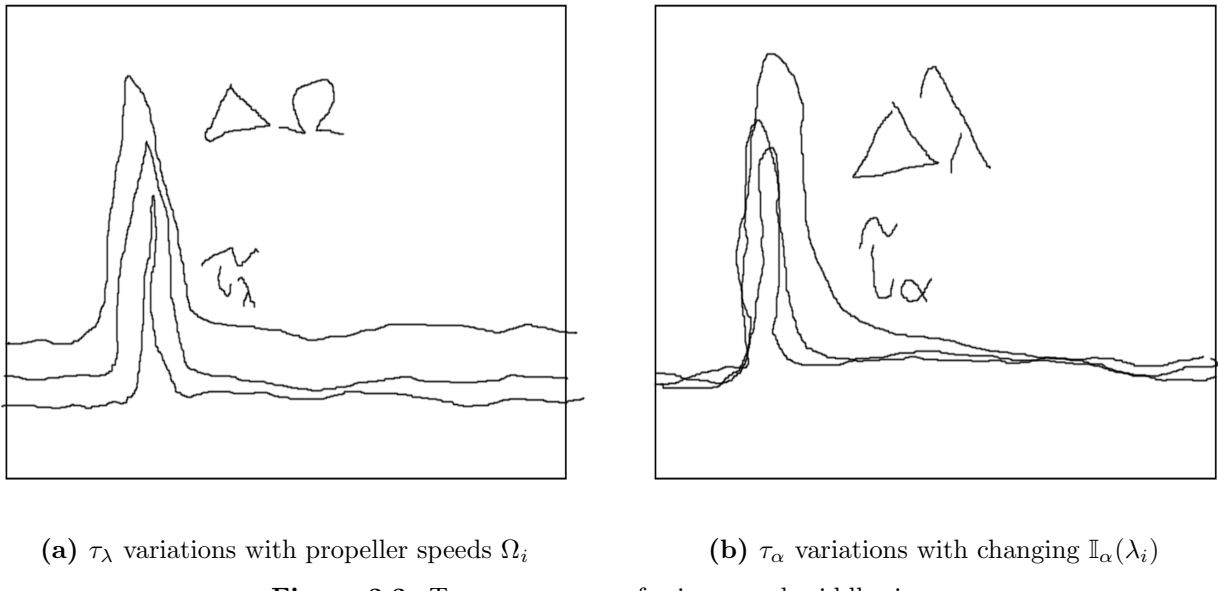
**Figure 3.2:** Torque response rig

<sup>12</sup>Relative to the body frame and not the inertial frame because Eq:3.9d accounts for the inertial response of the entire body frame. Here only the induced relative responses are being considered.

Each of the induced torques,  $\vec{\tau}_\lambda$  and  $\vec{\tau}_\alpha(\lambda_i)$ , occur in intermediary frames associated with the inner and middle ring assemblies. As such, their negative responses effect<sup>13</sup> Eq:3.9d, and each need to be transformed to the body frame.

$$\vec{\tau}_Q(u) = \sum_{i=1}^4 -Q_{M_i}^* \otimes \vec{\tau}_{\lambda_i}(u) \otimes Q_{M_i} - Q_{M'_i}^* \otimes \vec{\tau}_{\alpha_i}(u) \otimes Q_{M'_i} \in \mathcal{F}^b \quad (3.40)$$

The torque response equations were tested using the rig in Fig:3.2. The first plot in Fig:3.3a shows the induced torque for  $\tau_\lambda$  measured purely about the  $\hat{X}_{M_i}$  axis. The plot changes with increased rotation rates of  $\Omega_i$ <sup>14</sup>, illustrating the gyroscopic torque effect from the propeller's rotation. Plotted against measured values are  $\hat{\tau}_\lambda$  estimates from Eq:3.38c. Similarly the second plot in Fig:3.3b shows the middle ring induced torque,  $\tau_\alpha \in \mathcal{F}^{M'_i}$ . Detailing variations with respect to changing  $\lambda_i$  positions. The changes in  $\mathbb{I}_\alpha(\lambda_i)$  alter the magnitude of torque responses inline with estimates of  $\hat{\tau}_\alpha$ .



(a)  $\tau_\lambda$  variations with propeller speeds  $\Omega_i$       (b)  $\tau_\alpha$  variations with changing  $\mathbb{I}_\alpha(\lambda_i)$

**Figure 3.3:** Torque responses for inner and middle rings

The above responses are pertinent to simulation and plant dependent feedback compensation. The simulation environment is structured such that the torques are produced as responses from Newtonian movement at every step interval. In due course it would be more efficient (and less stiff) for the simulation to exploit an implicit Euler [54, 117] coordinate system in lieu of the cartesian response equations developed above. However this was not implemented in Chapter:5 and remains open to further testing and simulation...

### 3.3 Aerodynamics

The relationship between a propeller's rotational speed,  $\Omega_i$ , and its produced thrust,  $\vec{T}(\Omega_i)$ , is more complicated than the quadratic simplification taken at static conditions which most papers purport. Thrust induced is mostly dependent on the incident air stream flowing into the propellers rotational plane; typically being the component of the body velocity normal to that propeller's plane (Eq:3.57). Parallel fluid flowing across the propeller contributes toward in-plane aerodynamic drag (hence torque).

<sup>13</sup>Depending on dynamic equations used it could effect Eq:3.13b. However the equations Eq:3.13 are unnecessary when using quaternion dynamics.

<sup>14</sup>Motors 1 & 3 have clockwise rotations ('+'), motors 2 & 4 are counter-clockwise ('-').

The combination of aerodynamic Blade-element [82,95] and fluid-dynamics Momentum (*disc actuator*) theories stipulates an integral term taken across the propellers length which accurately models the produced thrust and torque. A verbose presentation of all aerodynamic effects experienced by a quadrotor's propeller(s) is thoroughly detailed in [8] and again [7]. The following provides a review of pertinent aerodynamic theories. Some phenomena aren't included, like Vortex Ring States or parasitic drag like effects, which weren't deemed to be pertinent.

### 3.3.1 Propeller Torque and Thrust

A feasible situation which the prototype could encounter is where an upstream propeller provides the incident fluid flow to another downstream propeller. Such a situation presents a complicated fluid dynamics & vortex wake effect problem. Propeller overlapping effects are investigated in [108], but remain open to further research in the context of the aircraft considered here.

To expedite the system ID process some simplifications are made on the aerodynamics to construct an approximate model; specifically using coefficients in place of complete local chord and pitch based integrals. Such an assumption holds true given that fixed pitch propellers are used.

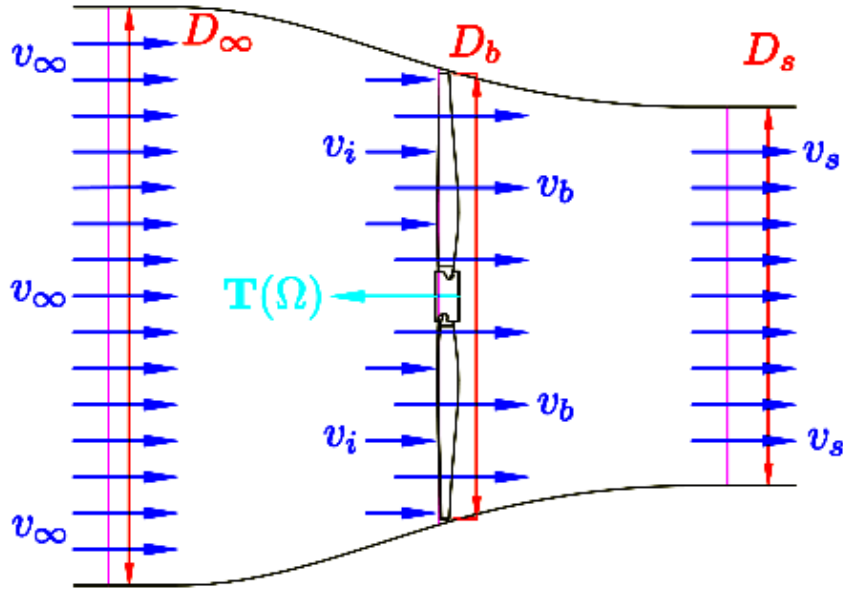


**Figure 3.4:** Disc Actuator Propeller Planar Flow

The rotation of a propeller applies a thrust force,  $\vec{T}$ , onto the fluid stream<sup>15</sup> in which it acts. That fluid stream (Fig:3.4) has an incident head velocity,  $v_\infty$ , and a resultant slip velocity downstream relative to the rotational plane,  $v_s$ . There exists some relationship about the change of fluid flow applied by the propeller's rotation. Such a relationship can then be given by:

$$v_s = \Delta v + v_\infty \quad (3.41)$$

Wherein  $\Delta v$  is the change in velocity, added to the fluid by the propeller blade's rotating aerofoil profile. The propeller induces a velocity directly in front of its rotational plane,  $v_i$ , such that the net fluid flow into the plane is  $v_b = v_i + v_\infty$ . Bernoulli's principle<sup>†</sup> has it that net fluid flow through that plane is:

$$v_b = \frac{1}{2}(v_s - v_\infty) = \frac{1}{2}\Delta v = \frac{1}{2}v_s|_{v_\infty=0} \quad (3.42)$$

---

<sup>15</sup>Only perpendicular mass flow across the propeller's plane is considered for momentum theory, adjacent fluid velocities are small enough that propeller induced drag is neglected...

And as such, stemming from classical Disc Actuator<sup>†</sup> (fluid *momentum*) theory, the scalar force,  $T(\Omega)$ , acting on the fluid is calculated as a function of mass flow rate with respect to the change in fluid velocity (pressure differential).

$$T = (A_b v_b) \Delta v = \rho \pi R_b^2 v_b \Delta v = \rho \pi R_b^2 (v_i + v_\infty) \Delta v = \frac{1}{2} \rho \pi R_b^2 \Delta v^2 \quad (3.43)$$

Where  $R_b$  is the disc (propeller) radius for the fluid stream under consideration. The fluid density of that stream,  $\rho$ , is typically  $1.225 \text{ Kg.m}^{-3}$ . The solution to Eq:3.43 is not entirely clear in terms of  $\Omega_i$ , which is the desired form in which the thrust can be calculated. It can however be solved as a function of aerodynamic propulsive power expended,  $\Delta P = \vec{T} \cdot \vec{\Delta v}$ . That kinetic energy relationship between rotational kinetic energy and power transferred from the motor is tenuous at best, compounded by parasitic losses which deteriorate the power transferred through the propellers. Furthermore, the local fluid velocity through the propeller isn't purely normal to its plane.

The fluid flow induced by the propeller's rotation directly in front of its plane of rotation is not purely perpendicular but has axial and tangential induced velocity components,  $a$  and  $a'$  respectively. Those induced components for the fluid velocity can be abstracted to induction factors dependent on the incident fluid velocity to the propeller's plane of rotation:

$$v_i = av_\infty \text{ in the axial direction} \quad (3.44a)$$

$$v_\theta = a'\Omega_i R_b \text{ in the tangential direction} \quad (3.44b)$$

From induction factors defined Eq:3.44, the velocity components can be written as functions of free upstream velocity  $v_\infty$ .

$$v_b = (1 + a)v_\infty \quad (3.45a)$$

$$v_s = (1 + 2a)v_\infty \quad (3.45b)$$

A consequence of the tangential fluid flow is that there exists an angular momentum flow rate across the propeller plane. This results in a torque response to the rotational motion about the propeller's axis of rotation, analogous to Eq:3.43.

$$\vec{Q} = \rho \pi R_b^3 (v_\theta - v_\infty) v_b \quad (3.46)$$

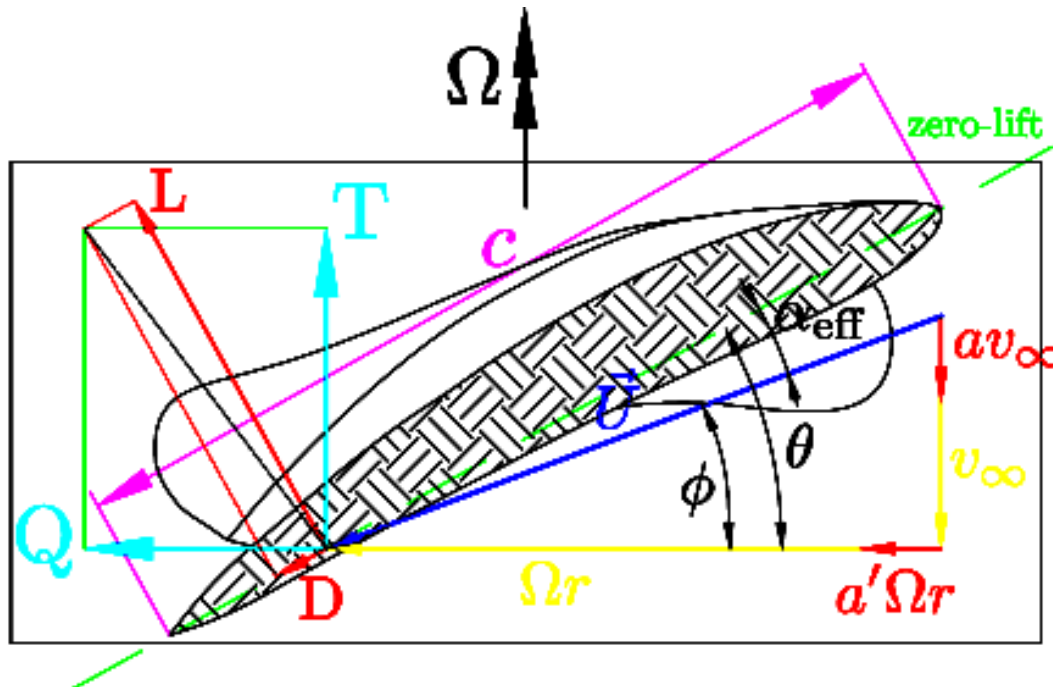


**Figure 3.5:** Blade element profile at radius  $r$

Together, Eq:3.43 & Eq:3.46 make up propeller momentum theory but cannot be solved on their own. Blade-element theory analyses incremental aerofoil sections of width  $dr$  of the propeller profile (Fig:3.5) at some radius  $r$ . Net local fluid velocity across a single elemental aerofoil profile  $\vec{U}$  is calculated as:

$$\vec{U} = \sqrt{(v_\infty + v_i)^2 + (v_\Omega + v_\theta)^2} \quad (3.47)$$

Each elemental profile, of chord length  $c$ , has a local pitch,  $\theta$ , of its aerofoil zero-lift line relative to the horizontal. Local fluid velocities (again in Fig:3.5) encountered by the propeller make their own an angle of attack  $\phi$  such that:

$$\phi = \theta - \alpha_{effective} \quad (3.48)$$

That local angle of attack changes with the inflow magnitude  $v_\infty$  and the induced axial velocity  $v_i$ . That trigonometric ratio is given as:

$$\phi = \tan^{-1} \left( \frac{v_\infty + v_i}{v_\Omega + v_\theta} \right) = \tan^{-1} \left( \frac{v_\infty(1+a)}{\Omega r(1+a')} \right) \quad (3.49)$$

The in-plane fluid flow  $\vec{U}(r, \phi)$ , for an element at radius  $r$  with a local angle of attack  $\phi$ , then contributes towards elemental lift and drag forces as a function of aerofoil's dimensionless lift,  $C_L$ , and drag,  $C_D$ , coefficients<sup>16</sup>.

$$\Delta L = \frac{1}{2} \rho \vec{U}(r, \phi)^2 c C_L \quad (3.50a)$$

$$\Delta D = \frac{1}{2} \rho \vec{U}(r, \phi)^2 c C_D \quad (3.50b)$$

With air density  $\rho^{17}$  and local chord length  $c$ . Those lift and drag forces are taken as components parallel and perpendicular to the plane of rotation. Those components are then thrust  $T$  and torque  $F_x$  forces (Fig:3.5). The in-plane force  $F_x$  applies an aerodynamic torque  $Q$  as the force acts at a radius  $r$ .

$$dT = \frac{1}{2} \rho \vec{U}(r, \phi)^2 c (C_L \cos(\phi) + C_D \sin(\phi)) . dr \quad (3.51a)$$

$$dF_x = \frac{1}{2} \rho \vec{U}(r, \phi)^2 c (C_L \sin(\phi) + C_D \cos(\phi)) . dr \quad (3.51b)$$

$$\rightarrow dQ = \frac{1}{2} \rho \vec{U}(r, \phi)^2 c (C_L \sin(\phi) + C_D \cos(\phi)) r . dr \quad (3.51c)$$

$$\rightarrow dP = \Omega r dF_x . dr \quad (3.51d)$$

Typically a power term, Eq:3.51d, is given in lieu of torque or drag terms, Eq:3.51c or Eq:3.51b. Then calculating forces and power terms as per momentum theory for each element, in terms of axial and tangential induction factors:

$$dT = \rho 4\pi r^2 v_\infty (1+a) a . dr \quad (3.52a)$$

$$dP = \rho 4\pi r^2 v_\infty (1+a) \Omega r (1+a') . dr \quad (3.52b)$$

Finally equating momentum and element terms together produces the blade-element momentum equation(s) for thrust and power produced by a propeller. Following a few assumptions, most importantly that the lift coefficient  $C_L$  is a linear function of the effective angle of attack  $\alpha_{eff}$ . The lift curve gradient,  $a_L$ , for an ideally twisted blade, like the fixed pitch propellers under consideration here, is typically  $2\pi$  such that  $C_L = 2\pi(\theta - \phi)$ . And assuming that tangentially induced velocities  $v_\theta$  are small (or that the tangential induction factor  $a' \ll 1$ ) when compared to the propeller's speed  $\Omega r$ . Similarly the net inflow and axial induced velocities  $v_\infty + v_i \ll \Omega r$ <sup>18</sup>

<sup>16</sup>The lift and drag coefficients are determined by the aerofoil's characteristics, but would be constant across the length of a variable pitch, non-twisted hinged propeller...

<sup>17</sup>Typically  $\rho = 1.225 \text{ kg/m}^3$

<sup>18</sup>Small angle approximations then apply to  $\cos(\phi + \alpha_{eff}) \approx 1$  and  $\sin(\phi + \alpha_{eff}) \approx \phi + \alpha_{eff}$

$$T = \int_{r=0}^R \frac{1}{2} a_L b c \rho (\Omega r)^2 \left( \theta - \frac{v_\infty + v_i}{\Omega r} \right) dr \quad (3.53a)$$

$$P = \int_{r=0}^R \frac{1}{2} a_L b c \rho (\Omega r)^3 \left[ \left( \theta - \frac{v_\infty + v_i}{\Omega r} \right) \left( \frac{v_\infty + v_i}{\Omega r} \right) + C_d \right] dr \quad (3.53b)$$

With  $b$  being the number of propeller blades. Generally knowing exact pitch and chord values as a function  $r/R$  is difficult and calculating integrals at each process step is cumbersome. Both Eq:3.53a & Eq:3.53b can be solved by equating element and momentum terms (a full expansion is given in Appendix:A.2). Often dimensionless thrust, torque and power coefficients are defined across the entire blade's length:

$$C_T(J) = \frac{T}{\rho \Omega^2 D^4} \quad (3.54a)$$

$$C_P(J) = \frac{P}{\rho \Omega^3 D^5} \quad (3.54b)$$

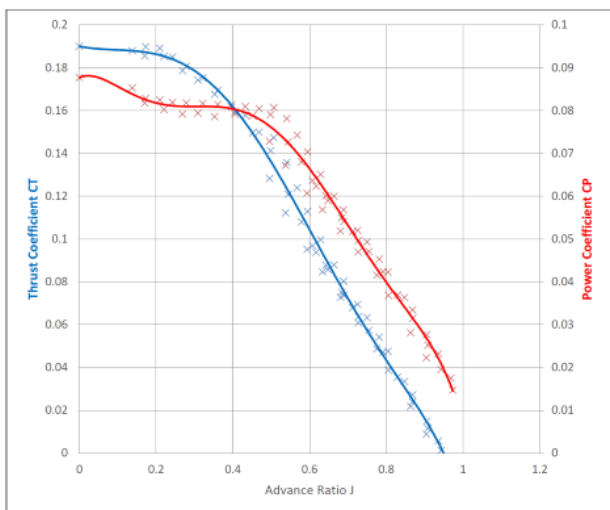


Figure 3.6: Power & thrust coefficients

Where  $\Omega$  is the propellers rotational speed in [RPS] and  $D$  is the propellers diameter in [mm]. For fixed pitch propellers the thrust and power coefficients are easily determined and remain consistent. Eq:3.54a and Eq:3.54b both vary due to what is defined as the *advance ratio*  $J$ .

$$J = \frac{v_\infty}{\Omega R} \quad (3.55)$$

In most cases, the net head stream velocity  $v_\infty$  is the perpendicular component (projected onto the plane's normal vector  $\hat{n}$ , Eq:3.57) of the vehicles transnational velocity in the body frame,  $\vec{v}_b \cdot \hat{n}$ . For the case of a zero advance ratio,  $J = 0$ , the conditions are regarded as static. Static thrust and power coefficients are nominal in their values.

Propeller databases like [18]<sup>19</sup> provide comprehensive values for a range of propeller types at different advance ratios. The introduction of those coefficients greatly simplifies the thrust estimation process. For a typical 6X4.5 inch propeller<sup>20</sup>, the static thrust and power coefficients respectively are:

$$C_{T0} = 0.191 \quad (3.56a)$$

$$C_{P0} = 0.0877 \quad (3.56b)$$

Fig:3.6 shows the thrust,  $C_T$ , and power,  $C_P$ , coefficients as a function of the advance ratio  $J$ . As the incident head fluid velocity,  $v_\infty$ , increases, the thrust coefficient decreases. So too does the power coefficient and hence the aerodynamic torque. The thrust and power coefficients can be assumed constant for low advance ratios, or in the case considered here, translational velocities.

In Fig:3.7, the thrust & torque test rigs and the results of both static (thrust and torque) tests are plotted. In each test the measured values are shown ( $T(\Omega)$  &  $Q(\Omega)$  with quadratic trend-lines) and an estimated value dependent on static coefficients ( $\hat{T}C_t(\Omega)$  &  $\hat{Q}C_p(\Omega)$ ). Using the results from the plot(s) in Fig:3.6 as a lookup table and calculating the values from Eq:3.54, induced propeller thrust and torques can be accurately modeled (*quadratically*<sup>21</sup>).

<sup>19</sup>The UIUC database also includes blade profiles, pitch and chord lengths. The database is the outcome of [19].

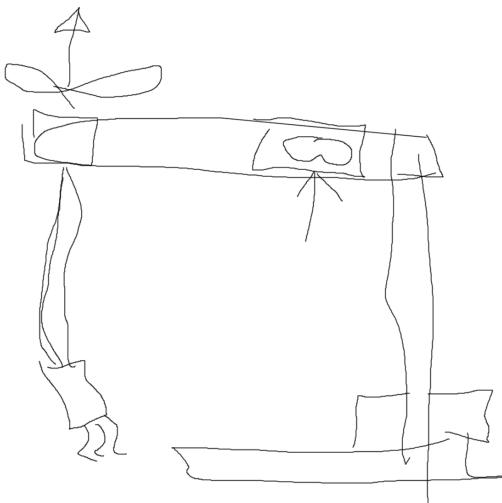
<sup>20</sup>Coefficients are linearly interpolated from similar pitched database results to match physical test values.

<sup>21</sup>The power term is cubic W.R.T its rotational velocity

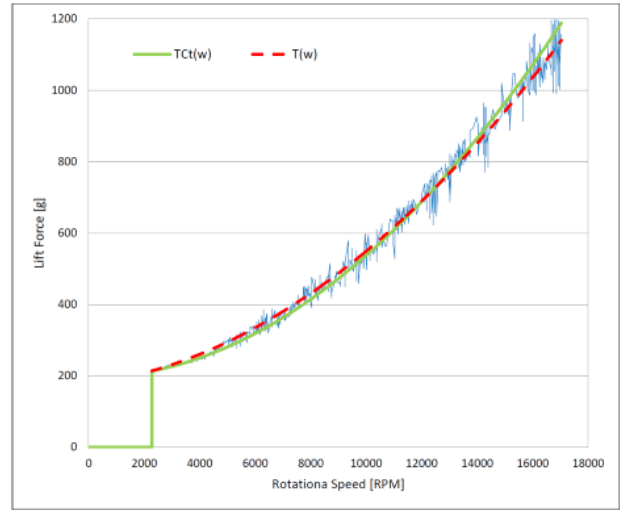
Instantaneous advance ratios, or rather the propeller incident fluid flow(s), are dependent on the vehicle's net transnational and angular velocity. Such that the fluid velocity's normal component to the propeller plane is given by:

$$v_\infty = (\vec{v}_b + \vec{L}_{arm} \times \vec{\omega}_b) \cdot \hat{n} \quad (3.57)$$

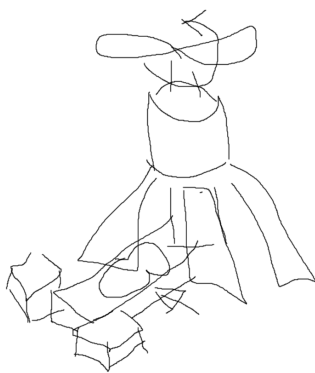
Where  $\vec{v}_b$  is the body's transnational velocity and  $\vec{\omega}_b$  is the body's angular velocity, both transformed to the propeller's frame,  $\in \mathcal{F}^{M_i}$ . Furthermore  $\hat{n}(\lambda_i, \alpha_i)$  is the unit vector normal to the propeller's rotational plane, dependent on the propeller's orientation relative to the body velocity. Then  $J$  is calculated as in Eq:3.55.



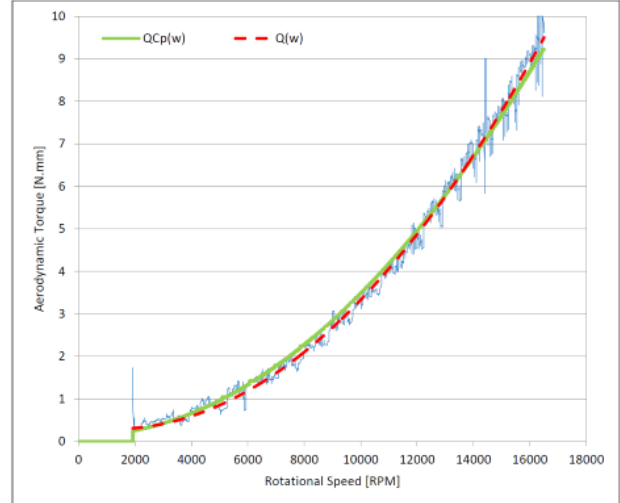
(a) Thrust test rig



(b) Thrust plot



(c) Torque test rig



(d) Torque plot

**Figure 3.7:** Static propeller tests

It's worth noting that the above static coefficients are indeed calculated from physical static tests. However advance ratio coefficient dependencies are linearly interpolated from the closest available matching data (APC Thin-Electric 8X6 propellers) cited from [18].

Counterclockwise and clockwise propellers and rotations were used for both thrust and torque tests. Despite the thrust and test rigs having been designed to isolate each respective response, the use of both directs allowed for opposing effects to cancel one another out. In the case of thrust tests plotted in Fig:3.7b; the opposing results were constructively averaged such that cross-directional torque effects on the strain gauge were canceled out.

Conversely the recorded torque results, plotted in Fig:3.7d, were subtractively averaged so that any erroneous perpendicular thrust deflection on the strain gauge was removed from the torque measurement. Both positive and negative rotational results for thrust and torque measurements are included in Appendix:C.1.

*Discrepancies which emerge between the model or coefficient values derived can be accounted for with lumped uncertainty disturbance term(s). Model uncertainty compensation can easily be incorporated into adaptive backstepping or  $H_\infty$  control algorithms. The deviation of the modeled thrust or torques from their true values would be simple to incorporate into a plant dependent Lyapunov candidate function; Sec:4.4.3.*

### 3.3.2 Hinged Propeller Conning & Flapping

Other non-linear effects which deteriorate a propeller's performance have all been well documented in the helicopter aerodynamic and propeller fields [17, 99]. Typically such affects are more pronounced when observing hinged variable pitch <sup>22</sup> propellers. Conning and flapping are the two most significant aerodynamic responses produced by a propeller. Other phenomenon like cyclic vortex ring states aren't applicable here and fall outside the scope of the investigation.

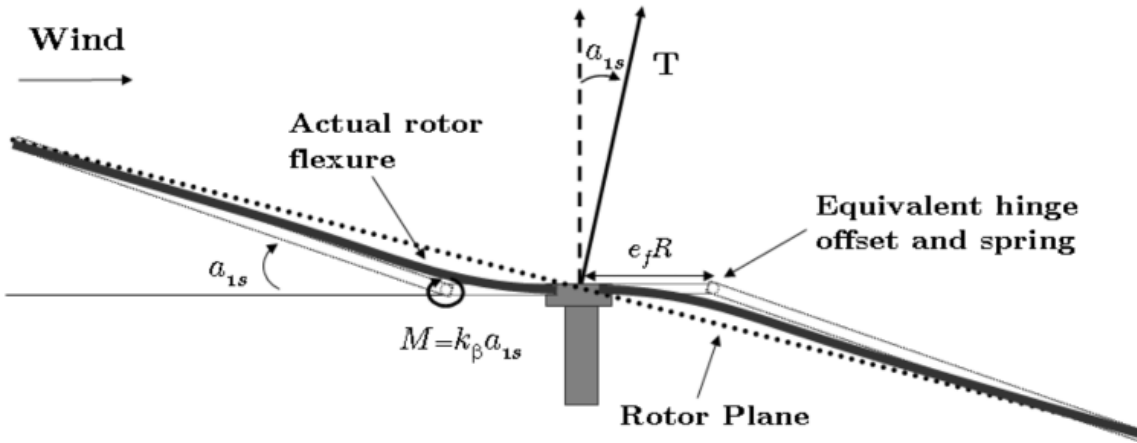


Figure 3.8: Propeller blade flapping

In translational flight for an unducted propeller each blade encounters varying incident fluid flow. The advancing blade, relative to the body's translational direction, encounters a greater fluid flow than the retreating blade. The result is that the effective local angle(s) of attack for the opposing advancing and retreating propeller blades aren't symmetrical. The unbalanced angles of attack produce a dissymmetry of lift across the propeller's surface.

Throughout each rotation the blade is forced up and down as it cycles through varying fluid flows, applying a torque about the propeller's hub. The extent of that torque is dependent on the body's net translational velocity and the propeller material's susceptibility to deflection. The flapping pitches the effective propeller plane (*tip-path plane*), and hence the thrust vector line, away from its principle axis, Fig:3.8<sup>23</sup>.

The overall net effect is that the propeller's thrust vector is pitched marginally away from an ideal perpendicular vector by some deflection angle. The phenomenon is diminished at low translational velocities and as such, isn't applicable to the range of flight envelopes which the prototype for this project will experience.

<sup>22</sup>Twisted, fixed pitched propellers are used on the prototype here and as such effects detailed in Sec:3.3.2 are diminished. Moreover, low translational velocities suppress such responses but they're worth mentioning.

<sup>23</sup>Diagram adapted from Hoffman et al.(2007) [46]

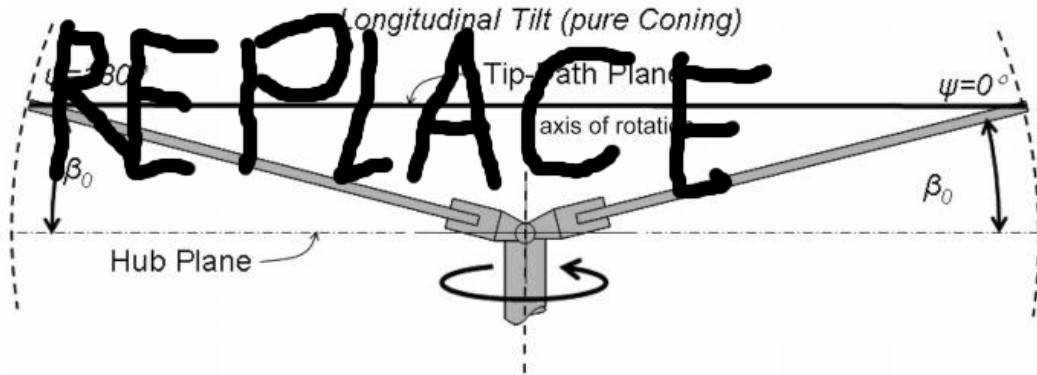


Figure 3.9: Propeller coning

Coning (illustrated in Fig:3.9) is another form of propeller deflection, which is again dependent on the blades stiffness properties, causes the propeller blades (advancing and retreating) to both deflect upward. Loading on the propeller surface and supporting a body's weight causes the upward deflection. The coning reduces the effective propeller disc's radius, adversely affecting thrust produced, Eq:3.53a. Increased loading accentuates the coning angle experienced by the propellers and as such alters the tip-path-plane.

Both aerodynamic induced propeller deflection effects can be quantified numerically. Their derivation and resultant equations are cumbersome however. In due course their effect on the produced prototype which this project investigates isn't significant enough to produce instability if neglected. The frame could potentially be affected in more adverse ways given certain flight conditions with higher translational velocities or incident wind & fluid flow disturbances...

### 3.3.3 Drag

For any solid body with some translational velocity motion within a fluid, there is a first order damping response opposing translational velocity. The net drag force,  $\vec{D}_{net}$ , although locally dependent on individual component cross-sections can be abstracted to a drag coefficient matrix representing the whole body.

$$\vec{D}_{net}(\vec{v}) = \begin{bmatrix} A_{xx} & A_{xy} & A_{xz} \\ B_{yx} & B_{yy} & A_{yz} \\ C_{zx} & C_{zy} & C_{zz} \end{bmatrix} \begin{bmatrix} u \\ v \\ w \end{bmatrix} \in \mathcal{F}^b \quad (3.58)$$

The drag coefficients,  $A, B$  &  $C$ , are determined by the frames directional cross-section areas for each  $\hat{X}_b, \hat{Y}_b, \hat{Z}_b$  axis. Given a well designed & symmetrical frame, it can be assumed the off-diagonal elements aren't of consequence and as such the drag equation can be simplified to:

$$\vec{D}_{net}(\vec{v}) \approx \text{diag}(A_{xx} \ B_{yy} \ C_{zz})\vec{v} \in \mathcal{F}^b \quad (3.59)$$

Without access to wind tunnel test facilities, the drag coefficients are difficult to empirically ascertain with a relative degree of certainty. As such the drag effects are relegated to the lumped disturbance & uncertainty term(s) to be adaptively compensated for, Sec:4.4.3. Analogous drag-like opposing effects to angular rotation rates do exist but, for the intents and purposes of most practical flight envelopes, can be disregarded.

In simulation; if the plant has sufficient disturbance rejection then a first order drag term in Eq:3.58 would be easily accounted for by the adaptive backstepping algorithm. It would be easy to physically test for the disturbance coefficients given further investigation on the prototype frame but, given the flight envelope for this research, is outside the scope of investigation here...

### 3.4 Consolidated Model

Reiterating the different aspects detailed above and consolidating the state equations from Eq:3.9a-3.9d. Then lifting the attitude states to  $\mathbb{R}^4$  space with the use of quaternions. Also introducing the non-linear inertial & gyroscopic responses to induced perturbations,  $\vec{\tau}_\lambda$  and  $\vec{\tau}_\alpha$  from Eq:3.38c & Eq:3.39d respectively, with non-linear inertial matrix terms  $\mathbb{I}_b(u)$  from Section:2.3. Finally replacing net virtual plant inputs<sup>24</sup>,  $\mu\vec{r}$  and  $\mu\vec{F}$ , with higher fidelity thrust models; produces the following set of state differentials used for control plant development ...

$$\dot{\mathcal{E}} = Q_b \otimes^* \vec{v}_b \otimes Q_b \quad \in \mathcal{F}^I \quad (3.60a)$$

$$\dot{\vec{v}}_b = m^{-1}(-\vec{\omega}_b \times m\vec{v}_b + Q_b \otimes m\vec{G}_I \otimes Q_b^* - \vec{D}_{net}(\vec{v}_b) + \mu\vec{F}(u)) \quad \in \mathcal{F}^b \quad (3.60b)$$

$$\dot{Q}_b = \frac{1}{2}Q_b \otimes \vec{\omega}_b \quad \in \mathcal{F}^I \quad (3.60c)$$

$$\dot{\vec{\omega}}_b = \mathbb{I}_b(u)^{-1}(-\vec{\omega}_b \times \mathbb{I}_b(u)\vec{\omega}_b + \vec{\tau}_Q(u) + \vec{\tau}_g(u) + \sum \vec{Q}(\Omega, \lambda, \alpha) + \mu\vec{r}(u)) \quad \in \mathcal{F}^b \quad (3.60d)$$

$$u = [\Omega_1^+, \lambda_1, \alpha_1, \dots, \Omega_4^-, \lambda_4, \alpha_4] \in \mathbb{U} \quad (3.60e)$$

With net thrust and torque plant control inputs,  $\mu\vec{F}$  &  $\mu\vec{r}$  respectively. Both are later abstracted to virtual control inputs next in Chapter:4, (*individual motor number subscripts,  $i \in [1 : 4]$ , are implied*).

$$\mu\vec{F}(u) = \sum \vec{T}(\Omega, \lambda, \alpha) = \sum Q_{M_i}^* \otimes T(\Omega) \otimes Q_{M_i} \quad \in \mathcal{F}^b \quad (3.61a)$$

$$\mu\vec{r}(u) = \sum \vec{l} \times \vec{T}(\Omega, \lambda, \alpha) = \sum \vec{l} \times (Q_{M_i}^* \otimes T(\Omega) \otimes Q_{M_i}) \quad \in \mathcal{F}^b \quad (3.61b)$$

The scalar thrust  $T(\Omega)$  is a function of the propellers rotational velocity however  $\vec{T}(\Omega, \lambda, \alpha)$  is a 3 dimensional thrust vector, redirected in the analogue of Eq:2.9a and transformed to the body frame  $\mathcal{F}^b$ . Equivalently  $Q(\Omega)$ <sup>25</sup> is the scalar aerodynamic torque term in  $\mathcal{F}^{M_i}$  about each motor's rotor  $\hat{Z}$ -axis,  $\vec{Q}(\Omega, \lambda, \alpha)$  is the torque vector counterpart in  $\mathcal{F}^b$ . Both thrust and aerodynamic propeller torque<sup>26</sup> terms are calculated from their respective coefficients (plotted in Fig:3.6):

$$T(\Omega) = C_T(J)\rho\Omega^2 D^4 \quad (3.62a)$$

$$Q(\Omega) = C_P(J)\rho\Omega^3 D^5 \frac{1}{R\Omega} \quad (3.62b)$$

Inertial torque responses from actuator input rates (*in feedback<sup>27</sup> configuration here*) from Eq:3.40;

$$\tau_Q(u) = \sum_{i=1}^4 -Q_{M_i} \otimes \tau_{\lambda_i}(u) \otimes Q_{M_i}^* - Q_{M'_i} \otimes \tau_{\alpha_i}(u) \otimes Q_{M'_i}^* \quad \in \mathcal{F}^b \quad (3.63)$$

And the variable gravitational torque arm from Eq:2.20d, dependent on net actuator positions  $u$ :

$$\vec{\tau}_g(u) = \Delta C.G \times \vec{G}_b \quad (3.64)$$

Finally, the body's net inertial tensor, taken from Eq:2.17 is given as:

$$\mathbb{I}_b(u) = \mathbb{I}_{body} + \sum_{i=1}^4 \mathbb{M}_{inner} + \sum_{i=1}^4 \mathbb{M}_{middle} \quad (3.65)$$

It is possible to bundle both attitude states (either euler angles  $\vec{\eta}$  or quaternions  $Q_b$ ) together with the linear translational position  $\mathcal{E}$  into a single state vector  $\mathbf{x}$ . Which then has its own combined control law. This could potentially exploit the cross-product coupling terms between angular and linear displacements for control benefits.

<sup>24</sup>Exact actuator relationships are explored in Section:4.2

<sup>25</sup>Disambiguation:  $Q(\Omega)$  here is a torque, not a quaternion.

<sup>26</sup>Torque dependent on the power term calculated from Eq:3.51d

<sup>27</sup>Response terms are used later as secondary actuator inputs in feedforward configuration rather than feedback terms to be compensated for.

# Chapter 4

## Controller Development

### 4.1 Control Loop

The control problem for this dissertation is, as outlined in Chater:1; to achieve dynamic (*attitude*) set point tracking on a quadrotor by solving the problem of its inherent underactuation. For the purposes of the subsequent controller development, the plant is described in the following non-linear state space form:

$$\dot{\mathbf{x}} = f(\mathbf{x}, t) + g(\mathbf{x}, \vec{\nu}, t) \quad (4.1a)$$

$$y = c(\mathbf{x}, t) + d(\mathbf{x}, \vec{\nu}, t) \quad (4.1b)$$

Where the plant dynamics are governed by  $f(\mathbf{x}, t)$  and the plant's input response by  $g(\mathbf{x}, \vec{\nu}, t)$ , for a given control input  $\vec{\nu}$ . The latter is not necessarily a function based relationship and could take the multiplicative form;  $g(\mathbf{x}, t)\vec{\nu}$ . The objective for setpoint tracking is for the output to track the state; namely  $y = \mathbf{x}$ . As such, the control problem is to design a stabilizing control law for an error state  $\mathbf{x}_e$ <sup>1</sup>:

$$\vec{\nu}_d = h(\mathbf{x}_e, t) \quad (4.2)$$

Such that the control plant is globally asymptotically stable or that  $\lim_{t \rightarrow \infty} \mathbf{x}_e = 0$ . It is possible to combine attitude and position states into one common trajectory state such that:

$$\mathbf{x} = \begin{bmatrix} \vec{\mathcal{E}} \\ Q_b \end{bmatrix} \quad (4.3)$$

The body's trajectory is then fully described by  $\mathbf{x}(t)$ . Separate control laws are developed for attitude and position tracking and hence those states aren't combined. However for the purposes of discussing the control plant, a single major loop is considered. The designed control input,  $\vec{\nu}_d$ , is then implemented by actuator suite  $u \in \mathbb{U}$  through its effectiveness function:

$$\nu_c = B(\mathbf{x}, u, t) \quad (4.4)$$

The exact relationship of the virtual control input and commanded input,  $\nu_c \rightarrow \nu_d$ , is governed by the allocation algorithm. That allocation function,  $B^\dagger$ , can be *roughly* referred to as the effectiveness inverse<sup>2</sup>. The actuator positions are then solved for, avoiding saturation, subject to some constraint:

$$\underset{\in \mathbb{U}}{u} = B^\dagger(\mathbf{x}, \nu_d, t) \quad (4.5)$$

The control allocation requirements and schemes are expanded upon subsequently in Sec:4.6. Multiple attitude controllers are presented whose stability is proven with Lyapunov<sup>†</sup> stability theorem. Each controller is compared in the context of an over actuated quadrotor plant. Similarly a series of proposed allocation schemes are evaluated too. Those comparisons, their details and how controller efficacy and stability are evaluated is all presented next in Chapter:5.

<sup>1</sup>Ignoring how the state error is formulated for the time being...

<sup>2</sup>Direct (*pseudo*) inversion is the typical allocation scheme.

A generalized over-actuated control loop is split into a series of cascaded control blocks, each with an individual function, as illustrated in Fig:4.1. From the error state of the generated trajectory,  $\mathbf{x}_e$ , the control law designs a virtual control input,  $\vec{\nu}_d$ , which is cast as the argument to the allocation block. From the allocation law,  $B^\dagger(\mathbf{x}, \vec{\nu}_d, t)$ , physical actuator positions are obtained;  $u \in \mathbb{U}$ . Those actuator positions effect a virtual plant input,  $\vec{\nu}_c = B(\mathbf{x}, u, t)$ , which is an input to the state function's dynamics, Eq:3.60. Not shown, but implied in Fig:4.1, is the state derivative feedback of  $\dot{\mathbf{x}}$  to the plant transfer function. Finally the output tracking state is estimated with some filtration paradigm,  $\hat{\mathbf{x}} = A(\mathbf{x}, t)$ , and fed back to the error state.

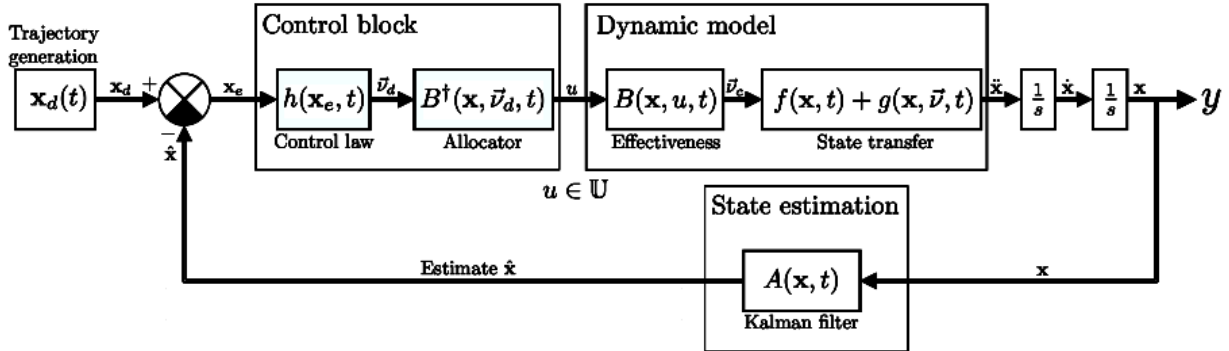


Figure 4.1: Generalized control loop with allocation

## 4.2 Control Plant Inputs

Thus far control plant inputs for the set of differential state equations, from Eq:3.60, have mostly been described with net forces and torques;  $\mu\vec{F}$  &  $\mu\vec{\tau}$ . The relationship between each propeller's rotational speed & servo positions and the its resultant output thrust direction is calculated as a quaternion transformation of produced lift force, as in Eq:3.61.

$$\mu\vec{F}(u) = \sum Q_{M_i}^*(\lambda_i, \alpha_i) \otimes T(\Omega_i) \otimes Q_{M_i}(\lambda_i, \alpha_i) \quad \in \mathcal{F}^b \quad (4.6a)$$

$$\mu\vec{\tau}(u) = \sum \vec{l} \times (Q_{M_i}^*(\lambda_i, \alpha_i) \otimes T(\Omega_i) \otimes Q_{M_i}(\lambda_i, \alpha_i)) \quad \in \mathcal{F}^b \quad (4.6b)$$

To accommodate comparison of each controller and allocation scheme, the error state control law(s) design net plant inputs  $\mu\vec{F}$  and  $\mu\vec{\tau}$ . The allocation rule then takes both net inputs as an argument to find actuator positions to effect those net inputs. As such each control law can be tested against various allocation rules and *vise versa*. However typical allocation algorithms, like pseudo-inversion, require a multiplicative relationship between plant and control inputs...

The actuator effectiveness functions in Eq:4.6 aren't readily reducible to a single multiplicative relationship with the actuator matrix  $u \in \mathbb{U}$ . Thusly the effectiveness function needs an extra layer of abstraction to incorporate a multiplicative relationship. Rather than calculating actuator positions directly from  $\vec{\nu}_d$ , a set of four 3-dimensional thrust vectors,  $\vec{T}_{1 \rightarrow 4}$  for each motor module, are calculated first.

$$\vec{\nu}_d = \begin{bmatrix} \mu\vec{F} \\ \mu\vec{\tau} \end{bmatrix} = \begin{bmatrix} 1 & 1 & 1 & 1 \\ [\vec{l}_1]_\times & [\vec{l}_2]_\times & [\vec{l}_3]_\times & [\vec{l}_4]_\times \end{bmatrix} \begin{bmatrix} \vec{T}_1 \\ \vec{T}_2 \\ \vec{T}_3 \\ \vec{T}_4 \end{bmatrix} \quad (4.7)$$

Where  $[\vec{l}_i]_\times$  is the cross product vector of the  $i^{th}$  torque arm. Individual actuator positions for each module,  $[\Omega_i, \lambda_i, \alpha_i]^T$ , can be calculated from those thrust vectors  $\vec{T}_i$  for  $i \in [1 : 4]$  with some trigonometry, ensuring that they only adhere to Eq:4.6. That trigonometric inversion<sup>3</sup> can be described as the function  $R^\dagger$ :

$$[\Omega_i, \lambda_i, \alpha_i]^T = R^\dagger(\mathbf{x}, \vec{F}_i, t) \quad \text{for } i \in [1 : 4] \quad (4.8)$$

<sup>3</sup>Inverting either rotation matrix operations or quaternions to solve for angular servo positions, Eq:4.109 in Sec:4.6.

To summarize then; each allocation rule controls designs net thrust vectors for each of the four modules, or 12 directional components, in the following form:

$$B^\dagger(\mathbf{x}, \vec{v}_d, t) = [T_{1x}, T_{1y}, T_{1z}, \dots, T_{4x}, T_{4y}, T_{4z}]^T \quad (4.9)$$

The control block in the loop (Fig:4.1) is then modified to incorporate the extra allocation abstraction level, shown in Fig:4.2. The output from that control block is still the same actuator matrix  $u \in \mathbb{U}$ . The block merely accommodates for comparison of various  $B^\dagger(\mathbf{x}, \vec{v}_d, t)$  allocation rules without having to redesign the remainder of the loop's structure.

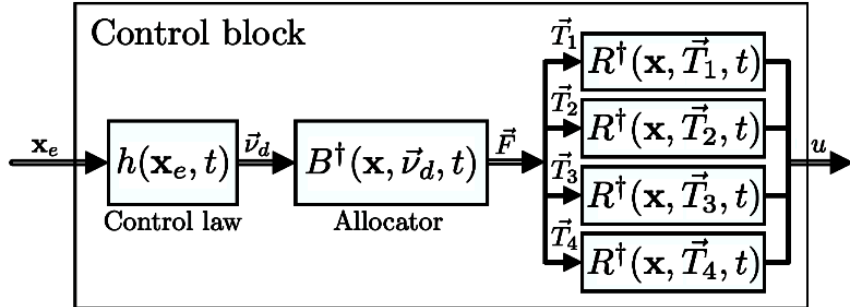


**Figure 4.2:** Abstracted control block

Al allocation algorithms proposed follow the same input/output structure described in Fig:4.2. Only one allocation algorithm does, however, circumvent the virtual abstraction level of thrust vector's for each module to directly calculate actuator positions, Section:4.6.5.

Each control law is co-dependent on an accompanying allocation algorithm. Traditional control loops (under-actuated or well matched) typically have a unity allocation rule and as such require no consideration so they're mostly disregarded. Separate control laws for attitude ad position control are presented next in Section:4.4 and 4.5 respectively. Thereafter a series of allocation rules are proposed in Section:4.6. Although presented independently, the controller and allocation laws are mutually inclusive. The stability of each control law is proven objectively but actual controller tuning and optimization takes place only in the following Chapter:5, in Sec:5.1.

## Model Dependent & Independent Controllers

Two classes of controllers are presented, attitude and position control laws. The former being the primary focus of this research project and containing a more complete control treatment and comparison of controllers. Both control categories consider MIMO state vector loops for  $\mathcal{E}$  &  $Q_b$ . The allocation algorithm combines both virtual control inputs  $\vec{\mu}_d = [\mu\vec{F} \ \mu\vec{r}]^T$  generated from the two control categories to calculate actuator positions.

The control dependency on the system plant is as a consequence of the prominent actuator response dynamics, as derived previously in Sec:3.2.1 from Chapter:3. Whilst not a prerequisite for stability, plant dependent compensation certainly improves controller performances. Independent and dependent cases are only presented in one type of controller; the most basic case PD controller in Section:4.4.2. It's shown that for an independent (PD) controller to achieve global stability some stringent assumptions must first be met.

Inherent plant dependency makes backstepping controllers an attractive control paradigm in this dissertation's context. The proposed dependent control laws compensate for undesirable dynamics their design, basic PD & PID control structures (*and the like*) will not. The first and most basic control solution, used as a reference case, is a PD controller for attitude and position with direct-inversion<sup>4</sup> allocation, both plant dependent and independent controllers are compared.

<sup>4</sup>Pseudo-inversion or Moore-Penrose inversion

### 4.3 Lyapunov Stability Theorem

Lyapunov's stability theory is a critical aspect of non-linear controller design. An abundance of literature has been written on the subject<sup>5</sup> spanning through the progression of control engineering. Typically linear systems are proven<sup>†</sup> to be stable using the frequency domain and Laplace transforms, the same is not true for non-linear systems. Lyapunov's stability theorem proves (*global*) asymptotic stability for continuous time invariant systems, linear or otherwise.

The theorem applies analysis of a generalized energy function representative of a system's autonomous trajectory. A negative trajectory energy derivative will ensure the system's energy is always dissipating toward a stable settling point. Lyapunov analysis is a popular method for stability verification because the trajectory of the system needn't be explicitly defined for stability to be determined. Proof of Lyapunov's theorem is done with a contradiction disproof and, as such, the theoretical underpinning is somewhat cumbersome.

Despite the conceptually difficult proof, it's worth reiterating its fundamentals given that backstepping controllers are proposed later in Sec:4.4.3 for attitude control. A backstepping controller iteratively enforces Lyapunov stability criterion onto the system through the control structure. In general, given a non-linear time invariant system that follows some continually differentiable trajectory  $\mathbf{x}(t)$ , typically the trajectory is going to progress subject to some rule:

$$\dot{\mathbf{x}}(t) = f(\mathbf{x}(t)) \quad (4.10)$$

Then, constructing a generalized positive-definite function (generalized energy or *Lyapunov candidate* function)  $V(x)$  for a trajectory  $x = \mathbf{x}(t)$ . A positive definite matrix,  $M$ , is defined such that  $z^T M z \geq 0 \forall z$ . As such an LCF typically has the form:

$$V = \mathbf{x}^T P \mathbf{x} \quad (4.11)$$

Given that, by its definition, the trajectory is continually differentiable; there is a gradient matrix for  $V(x)$  in the form:

$$\nabla V(x) = \begin{bmatrix} \frac{\delta V(x)}{\delta x_1} & \frac{\delta V(x)}{\delta x_2} & \dots & \frac{\delta V(x)}{\delta x_n} \end{bmatrix} \quad x \in \mathbb{R}^n \quad (4.12)$$

The energy function's derivative, otherwise referred to as the *Lie derivative*<sup>†</sup>, is calculated as follows:

$$\dot{V}(x) = \nabla V(x)^T f(x) = \frac{\delta V(x)}{\delta x_1} f_1(x) + \frac{\delta V(x)}{\delta x_2} f_2(x_2) + \dots + \frac{\delta V(x)}{\delta x_n} f_n(x) \quad (4.13)$$

Lyapunov's theorem states that *iff* the candidate function  $V(x)$  is positive definite with  $\dot{V}(0) = 0$  and its derivative is negative definite;  $\dot{V}(x) < 0 \forall x \neq 0$ , the system is then globally asymptotically stable. Mathematically that means, for any  $\mathbf{x}(t) \geq 0$ :

$$V(\mathbf{x}(t)) = V(\mathbf{x}(0)) + \int_0^t \dot{V}(\mathbf{x}(t)).dt \leq V(\mathbf{x}(t)) \quad (4.14)$$

Which can be physically interpreted as the system's generalized energy function always dissipating, irrespective of trajectory path taken. With a continually decreasing energy, the system will eventually settle to some stable point, hence the trajectory exists in some bounded  $\{x | V(x) \leq V(\mathbf{x}(t))\}$ , which is defined as global asymptotic stability. Every trajectory of  $\dot{\mathbf{x}}(t) = f(\mathbf{x}(t))$  converges to the zero<sup>6</sup> setpoint as  $t \rightarrow \infty$ .

The asymptotic stability proof can be extended to exponential stability boundedness, such that if the same conditions are met and there exists some positive coefficient  $\alpha > 0$  such that  $\dot{V}(x) \leq -\alpha V(x)$ . That implies the system is globally exponentially stable as is bound in such a manner that:

$$\|\mathbf{x}(t)\| \leq M e^{-\alpha t/2} \|\mathbf{x}(0)\| \quad (4.15)$$

---

<sup>5</sup>Included in almost every meritable textbook and papers; [73, 91], amongst others...

<sup>6</sup>Adapted to zero error state tracking in lieu or zero set point settling.

## 4.4 Attitude Control

### 4.4.1 The Attitude Control Problem

Set point tracking control of the attitude plant is to then design a stabilizing control torque  $\mu\vec{\tau} = h(\mathbf{x}_e, t)$  such that; for any desired attitude quaternion,  $\forall Q_d \in \mathbb{Q}$ , and an instantaneous attitude body quaternion, similarly  $\forall Q_b \in \mathbb{Q}$ , the error state asymptotically stabilizes to 0;  $Q_e \rightarrow [1 \vec{0}]^T$ . Or that:

$$\mu\vec{\tau} = h(Q_e, \dot{Q}_e) \text{ such that } \lim_{t \rightarrow \infty} Q_e = \begin{bmatrix} 1 \\ \vec{0} \end{bmatrix} \quad (4.16)$$

Quaternion error states are defined as the Hamilton product (*difference*) between the desired and current quaternion attitudes. Quaternion error states are in contrast with the subtractive relationship for Euler angle error states. The attitude error state is calculated as:

$$Q_e = Q_d^* \otimes Q_b \quad (4.17)$$

The relative angular velocity error between the body frame,  $\mathcal{F}^b$ , and the trajectory's desired frame,  $\mathcal{F}^d$ , is given as  $\vec{\omega}_e$ . The body angular velocity,  $\vec{\omega}_b$  is subject to the differential Eq:3.60d. As such there's an angular rate error:

$$\vec{\omega}_e = \vec{\omega}_d - \vec{\omega}_b \quad (4.18a)$$

The desired angular rate is taken with respect to the desired angular attitude frame, and so it must be transformed to the existing body frame.

$$\vec{\omega}_e = Q_e^* \otimes \vec{\omega}_d \otimes Q_e - \vec{\omega}_b \quad (4.18b)$$

Typically for the trajectories generated here  $\vec{\omega}_d = \vec{0}$ , so the angular rate error is simply the negative body angular velocity. It would be easy to include a non-zero angular velocity setpoint.

$$\vec{\omega}_e = -\vec{\omega}_b \quad (4.18c)$$

The time derivative of the quaternion error state is then, dependent on the angular velocity error, given as:

$$\dot{Q}_e = \frac{1}{2}Q_e \otimes \vec{\omega}_e = -\frac{1}{2}Q_e \otimes \vec{\omega}_b \quad (4.19)$$

### 4.4.2 Linear Controllers

#### PD Controller

The control law which is used as a basic reference for comparison is a simple Proportional-Derivative structured attitude controller. Specifically, a stability proof derived from the one presented *The Attitude Control Problem* [110] is used for asymptotic stability verification. An attitude PD control law, proportional to the vector quaternion error and angular rate error, designs the control torque as:

$$\mu\vec{\tau}_{PD} = K\vec{\omega}_e + \alpha\vec{q}_e \quad (4.20)$$

Where both  $K$  and  $\alpha$  are positive definite symmetrical  $3 \times 3$  coefficient matrices still to be determined. This control law does not take into account the quaternion error scalar. Then using a candidate Lyapunov energy function  $V_{PD}$ :

$$V_{PD} = \alpha\vec{q}_e^T \vec{q}_e + \alpha(q_0 - 1)^2 + \frac{1}{2}\vec{\omega}_e^T \mathbb{I}_b \vec{\omega}_e \quad (4.21)$$

And recalling from Eq:3.60d that body's the angular velocity differential  $\dot{\vec{\omega}}_b$  is:

$$\dot{\vec{\omega}}_b = \mathbb{I}_b^{-1}(-\vec{\omega}_b \times \mathbb{I}_b \vec{\omega}_b + \vec{\tau}_Q + \vec{\tau}_g + \vec{Q} + \mu \vec{\tau}) \in \mathcal{F}^b \quad (4.22)$$

With actuator inputs  $u \in \mathbb{U}$  implied and  $\vec{Q}$  being a simplified representation of the net aerodynamic torque experienced by the body from the rotating propellers, drawn from Eq:3.62b. Then, noting that from quaternion's inherent properties, it follows that:

$$\vec{q}^T \vec{q} + q_0^2 = \vec{q}^2 + q_0^2 = 1 \quad (4.23)$$

Substituting the angular velocity error state,  $\vec{\omega}_e = -\vec{\omega}_b$ , the proportional derivative LCF in Eq:4.21 is simplified<sup>7</sup> to:

$$V_{PD} = \alpha \vec{q}_e^2 + \alpha q_0^2 - 2q_0 + 1 + \frac{1}{2} \vec{\omega}_e^T \mathbb{I}_b \vec{\omega}_e \quad (4.24a)$$

$$= 2\alpha(1 - q_0) + \frac{1}{2} \vec{\omega}_b^T \mathbb{I}_b \vec{\omega}_b \quad (4.24b)$$

Similarly, using the fact that for a quaternion's time derivative:

$$\dot{Q} = \begin{bmatrix} -\frac{1}{2} \vec{q}^T \vec{\omega} \\ \frac{1}{2} (\vec{q} \times + q_0 \mathbb{I}) \vec{\omega} \end{bmatrix} \quad (4.25)$$

Then, resolving the above into the derivative of the LCF,  $\dot{V}_{PD}$ :

$$\dot{V}_{PD} = 2\alpha \frac{1}{2} \vec{q}_e^T \vec{\omega}_e + \frac{1}{2} \dot{\vec{\omega}}_b^T \mathbb{I}_b \vec{\omega}_b + \frac{1}{2} \vec{\omega}_b \mathbb{I}_b \dot{\vec{\omega}}_b^T \quad (4.26a)$$

$$= -\alpha \vec{q}_e^T \vec{\omega}_b + \vec{\omega}_b^T \mathbb{I}_b \dot{\vec{\omega}}_b \quad (4.26b)$$

Simplifying the angular acceleration  $\dot{\vec{\omega}}_b$  and introducing the PD control law Eq:4.20,  $\mu \vec{\tau}_{PD}$ :

$$\dot{\vec{\omega}}_b^T \mathbb{I}_b \dot{\vec{\omega}}_b = \vec{\omega}_b^T (-\vec{\omega}_b \times \mathbb{I}_b \vec{\omega}_b + \vec{\tau}_Q + \vec{\tau}_g + \vec{Q} - K \vec{\omega}_b + \alpha \vec{q}_e) \quad (4.27a)$$

$$\rightarrow \dot{V}_{PD} = -\alpha \vec{q}_e^T \vec{\omega}_b + \vec{\omega}_b^T (-\vec{\omega}_b \times \mathbb{I}_b \vec{\omega}_b + \vec{\tau}_Q + \vec{\tau}_g + \vec{Q} - K \vec{\omega}_b + \alpha \vec{q}_e) \quad (4.27b)$$

$$= -\alpha \vec{q}_e^T \vec{\omega}_b + \alpha \vec{\omega}_b^T \vec{q}_e - \vec{\omega}_b^T K \vec{\omega}_b + \vec{\omega}_b^T (-\vec{\omega}_b \times \mathbb{I}_b \vec{\omega}_b + \vec{\tau}_Q + \vec{\tau}_g + \vec{Q}) \quad (4.27c)$$

It follows that the transpose term  $\vec{q}_e^T \vec{\omega}_b \iff \vec{\omega}_b^T \vec{q}_e$  is interchangeable as its resultant product is the same. The LCF derivative then simplifies to:

$$\dot{V}_{PD} = -\vec{\omega}_b^T K \vec{\omega}_b + \vec{\omega}_b^T (-\vec{\omega}_b \times \mathbb{I}_b \vec{\omega}_b + \vec{\tau}_Q + \vec{\tau}_g + \vec{Q}) \quad (4.27d)$$

Then, under specific circumstances the following assumptions can be made to ensure the asymptotic stability proof can be applied. The stability obviously breaks down if any of the assumptions fail, as such the stability is not global...

1. The inertial matrix,  $\mathbb{I}_b$ , is roughly diagonal given the symmetrical design and similarly that the angular rate can be made small with appropriately slow trajectory updates, then:

$$\vec{\omega}_b^T (\vec{\omega}_b \times \mathbb{I}_b \vec{\omega}_b) \approx \vec{0}$$

2. The actuator rate torque responses,  $\vec{\tau}_Q$ , are all second order effects dependent on  $\dot{u}$ . Typically the actuator rates are going to be kept small and so any of the inertial responses to those position changes are small enough to be considered negligible. The approximation is made:

$$\vec{\tau}_Q \approx \vec{0}$$

3. Finally, for the sake of the stability proof, the eccentric gravitational torque arm is neglected,  $\vec{\tau}_g \approx \vec{0}$ . Such a situation only holds true if  $u \approx \vec{0}$  or that servo actuator positions<sup>8</sup> are close to their zero positions.

<sup>7</sup>The quaternion scalar  $q_0$  in Eq:4.24 is implied to be the quaternion error state scalar

<sup>8</sup>Excluding propeller rotational speeds, considering only the servo positions

All of these assumptions are made under extraneous circumstances and can't be assumed for almost all of the prototype's flight envelope. The plant independent case is considered and simulated purely for contrition; mainly to demonstrate the need for plant dependent compensation. All subsequent control laws compensate for the plant dynamic response torques introduced in Section:3.2.

If each of the assumptions made hold true, then the Lyapunov energy functions derivative is approximately negative definite.

$$\dot{V}_{PD} \approx -\alpha \vec{q}_e^T \vec{\omega}_b + \vec{\omega}_b^T (-K \vec{\omega}_b + \alpha \vec{q}_e) \quad (4.28a)$$

$$\Rightarrow \dot{V}_{PD} = -K \|\vec{\omega}_b\|^2 < 0 \quad \forall \mathbf{z}(t) \quad (4.28b)$$

Where  $\mathbf{z}(t)$  is a generalized attitude trajectory which includes  $\vec{\omega}_b$  &  $Q_b$  and  $K$  is a symmetrical positive (*definite*) 3X3 coefficient matrix. Then from Lyapunov stability theorem the limits exist;  $\lim_{t \rightarrow \infty} \vec{\omega}_e = \vec{0}$ ,  $\lim_{t \rightarrow \infty} \vec{q}_e = 0$  and  $\lim_{t \rightarrow \infty} (1 - q_0) = 0$ . Hence  $Q_e \rightarrow [1 \ \vec{0}]^T$  as  $t \rightarrow \infty$ , asymptotically stabilizing the attitude error state.

Introducing model dependent compensation to the PD control law in Eq:4.20 alleviates the stringent requirements on assumptions 1 through 3.

$$\mu \vec{\tau}_{PD} = \vec{\omega}_b \times \mathbb{I}_b \vec{\omega}_b - \vec{\tau}_Q - \vec{\tau}_g - \vec{Q} + K \vec{\omega}_b + \alpha \vec{q}_e \quad (4.29)$$

The resultant stability proof for Eq:4.29 is much the same as that for the independent case, Eq:4.20, and using the same LCF from Eq:4.21. The resultant dependent control law is less reliant on the very broad assumptions needed for independent stability to be achieved. The dynamic compensation in Eq:4.29 improves control response, especially considering the form of unwanted dynamics have already quantified previously and modeled with *relative* confidence.

### Auxiliary Plant Controller

Expanding on what has, in practice, proven<sup>9</sup> to be a very popular and effective control law for attitude stabilization, McGilvray et al. [2006] [107] suggested introducing an auxiliary plant term to a Proportional-Derivative structure. Their altered PD controller adds auxiliary terms proportional to the quaternion time derivative error. The important introduction is that part of the auxiliary plant is a term for the quaternion scalar. The scalar term is otherwise neglected in the previous PD control law (Sec:4.4.2).

The modified (*auxilliarily*) PD control torque is designed dependent on errors states for quaternions, angular rates and quaternion rates.

$$\mu \vec{\tau}_{XPD} = \underbrace{-\Gamma_2 \tilde{\Omega} - \Gamma_3 \vec{q}_e + \mathbb{I}_b \dot{\tilde{\Omega}}}_{Independent} + \underbrace{\vec{\omega}_b \times \mathbb{I}_b \vec{\omega}_b + \vec{\tau}_Q + \vec{\tau}_g + \vec{Q}}_{Compensation} \quad (4.30)$$

In which case the coefficients<sup>10</sup>  $\Gamma_2$  &  $\Gamma_3$  are both diagonal positive definite coefficient matrices and  $\Gamma_1$ , introduced subsequently in Eq:4.32, is a positive symmetric coefficient matrix. The auxiliary plants  $\tilde{\Omega}$  &  $\dot{\tilde{\Omega}}$  are defined as follows, and drawing on Eq:4.25 for definition of some aspects. For the first auxiliary plant  $\tilde{\Omega}$  is proportional to the quaternion error and hence  $\dot{\tilde{\Omega}}$  is a quaternion derivative term:

$$\tilde{\Omega} = -\Gamma_1 \vec{q}_e \rightarrow \dot{\tilde{\Omega}} = -\Gamma_1 \dot{\vec{q}}_e \quad (4.31a)$$

$$\dot{\tilde{\Omega}} = -\frac{1}{2} \Gamma_1 (q_0 \mathbb{I}_{3X3} + [\vec{q}_e] \times) \vec{\omega}_e \quad (4.31b)$$

$$= \frac{1}{2} \Gamma_1 (q_0 \mathbb{I}_{3X3} + [\vec{q}_e] \times) \vec{\omega}_b \quad (4.31c)$$

<sup>9</sup>Practical examples of various quadrotor attitude PD controllers listed in Table:1.1 from Sec:1.2.1.

<sup>10</sup>Reiterating that exact coefficient values are determined in Chapter:5...

And the second auxiliary plant,  $\tilde{\Omega}$ , is a term proportional to a combined quaternion and angular velocity error state.

$$\tilde{\Omega} = \vec{\omega}_e - \bar{\Omega} = \vec{\omega}_e + \Gamma_1 \vec{q}_e \quad (4.32a)$$

$$= -\vec{\omega}_b + \Gamma_1 \vec{q}_e \quad (4.32b)$$

Using an LCF similar to the basic one  $V_{PD}$  from Eq:4.21, but introducing an auxiliary term  $\tilde{\Omega}$  into the candidate function  $V_{XPD}$ :

$$V_{XPD} = \vec{q}_e^T \vec{q}_e + (q_0 - 1)^2 + \frac{1}{2} \tilde{\Omega}^T (\Gamma_3^{-1} \mathbb{I}_b) \tilde{\Omega} \quad (4.33)$$

Again using the simplification from a quaternion's inherent properties in Eq:4.23. The LCF from Eq:4.33 then simplifies with the following derivative:

$$V_{XPD} = 2(1 - q_0) + \frac{1}{2} \tilde{\Omega}^T (\Gamma_3^{-1} \mathbb{I}_b) \tilde{\Omega} \quad (4.34a)$$

$$\dot{V}_{XPD} = 2 \frac{1}{2} \vec{q}_e^T \vec{\omega}_e + \frac{1}{2} \dot{\tilde{\Omega}}^T (\Gamma_3^{-1} \mathbb{I}_b) \tilde{\Omega} + \frac{1}{2} \tilde{\Omega}^T (\Gamma_3^{-1} \mathbb{I}_b) \dot{\tilde{\Omega}} \quad (4.34b)$$

$$\dot{V}_{XPD} = -\vec{q}_e^T \vec{\omega}_b + \frac{1}{2} \dot{\tilde{\Omega}}^T (\Gamma_3^{-1} \mathbb{I}_b) \tilde{\Omega} + \frac{1}{2} \tilde{\Omega}^T (\Gamma_3^{-1} \mathbb{I}_b) \dot{\tilde{\Omega}} \quad (4.34c)$$

It then follows from Eq:4.32 that:

$$\dot{\tilde{\Omega}} = -\dot{\vec{\omega}}_b + \Gamma_1 \dot{\tilde{\Omega}} \Rightarrow \dot{\vec{\omega}}_b = \mathbb{I}_b^{-1} (-\vec{\omega}_b \times \mathbb{I}_b \vec{\omega}_b + \vec{\tau}_Q + \vec{\tau}_g + \vec{Q} + \mu \vec{\tau}) \quad (4.35a)$$

$$\therefore \dot{\tilde{\Omega}} = -\mathbb{I}_b^{-1} (-\vec{\omega}_b \times \mathbb{I}_b \vec{\omega}_b + \vec{\tau}_Q + \vec{\tau}_g + \vec{Q} + \mu \vec{\tau}) - \Gamma_1 \dot{\tilde{\Omega}} \quad (4.35b)$$

Introducing the control law,  $\mu \vec{\tau}_{XPD}$  from Eq:4.30, to the auxiliary plant derivative.

$$\rightarrow \dot{\tilde{\Omega}} = \mathbb{I}_b^{-1} (\mathbb{I}_b \dot{\tilde{\Omega}} - \Gamma_2 \tilde{\Omega} - \Gamma_3 \vec{q}_e) - \dot{\tilde{\Omega}} \quad (4.35c)$$

$$= \mathbb{I}_b^{-1} (-\Gamma_2 \tilde{\Omega} - \Gamma_3 \vec{q}_e) \quad (4.35d)$$

From the positive symmetric (or *diagonal*) properties of the coefficient matrices  $\Gamma_1, \Gamma_2$  &  $\Gamma_3$ , then the auxiliary plant's transpose is:

$$\dot{\tilde{\Omega}}^T = \mathbb{I}_b^{-1} (-\Gamma_2 \tilde{\Omega}^T - \Gamma_3 \vec{q}_e^T) \quad (4.36)$$

It then follows:

$$\frac{1}{2} \dot{\tilde{\Omega}}^T (\Gamma_3^{-1} \mathbb{I}_b) \tilde{\Omega} = \frac{1}{2} (-\Gamma_2 \tilde{\Omega}^T - \Gamma_3 \vec{q}_e^T) \Gamma_3^{-1} \tilde{\Omega} \quad (4.37a)$$

$$= \frac{1}{2} (-\tilde{\Omega}^T \Gamma_2 \Gamma_3^{-1} \tilde{\Omega} - \vec{q}_e^T \tilde{\Omega}) \quad (4.37b)$$

And substituting Eq:4.32,  $\vec{q}_e^T \tilde{\Omega} = -\vec{q}_e^T \vec{\omega}_b + \Gamma_1 \vec{q}_e^T$ :

$$\frac{1}{2} (-\tilde{\Omega}^T \Gamma_2 \Gamma_3^{-1} \tilde{\Omega} + \vec{q}_e^T \vec{\omega}_b - \vec{q}_e^T \Gamma_1 \vec{q}_e) \quad (4.37c)$$

Similarly, for the transposed energy function counterpart:

$$\frac{1}{2} \tilde{\Omega}^T (\Gamma_3^{-1} \mathbb{I}_b) \dot{\tilde{\Omega}} = \frac{1}{2} (-\tilde{\Omega} \Gamma_2 \Gamma_3^{-1} \tilde{\Omega}^T + \vec{q}_e^T \vec{\omega}_b - \vec{q}_e^T \Gamma_1 \vec{q}_e) \quad (4.37d)$$

Which, when substituted back into Eq:4.34c, then simplifies the LCF derivative to negative definite:

$$\Rightarrow \dot{V}_{XPD} = -\vec{q}_e^T \Gamma_1 \vec{q}_e - \tilde{\Omega} \Gamma_2 \Gamma_3^{-1} \tilde{\Omega}^T < \vec{0} \quad \forall (\vec{q}_e, \tilde{\Omega}) \quad (4.38)$$

As such, the control law  $\mu \vec{\tau}_{XPD}$  asymptotically stabilizes the attitude plant. Both  $\tilde{\Omega}$  and  $\vec{q}_e$  tend to  $\vec{0}$ , or more specifically the following limits exist:

$$\lim_{t \rightarrow \infty} \vec{q}_e = 0 \quad \text{and} \quad \lim_{t \rightarrow \infty} \tilde{\Omega} = 0 \quad (4.39a)$$

Then, from the auxiliary plant definition in Eq:4.32, the extended limits present themselves;

$$\lim_{t \rightarrow \infty} \vec{\omega}_b = 0 \quad \text{and} \quad \lim_{t \rightarrow \infty} \tilde{\Omega} = 0 \quad (4.39b)$$

The stability proof for  $V_{XPD}$  can then be extended to true exponential stability. From a quaternion's inherent definition it follows that  $0 \leq q_0 \leq 1$ . It can then be stated that:

$$1 - q_0 \leq 1 - q_0^2 = \|\vec{q}_e\|^2 \quad (4.40)$$

Seeing that exponential stability is a maximal boundedness proof, the relationship Eq:4.40 can then replace the quaternion scalar term  $2(1 - q_e)$  in  $V_{XPD}$ . For the stability proof the LCF is rewritten in terms of its norm(s) to produce the inequality:

$$V_{XPD} = \vec{q}_e^T \vec{q}_e + (q_0 - 1)^2 + \frac{1}{2} \tilde{\Omega}^T (\Gamma_3^{-1} \mathbb{I}_b) \tilde{\Omega} \quad (4.41a)$$

$$\rightarrow V_{XPD} \leq 2 \|\vec{q}_e\|^2 + \frac{1}{2} \Gamma_3^{-1} \mathbb{I}_b \|\tilde{\Omega}\|^2 \quad (4.41b)$$

Similarly the LCF derivative can be written in terms of its norms as:

$$\dot{V}_{XPD} = -\Gamma_2 \Gamma_3^{-1} \|\tilde{\Omega}\|^2 - \Gamma_1 \|\vec{q}_e\|^2 \quad (4.41c)$$

$V_{XPD}$  then gains a maximum such that:

$$V_{XPD} \leq \max \left\{ 2, \frac{\lambda_{\max}(\Gamma_3^{-1} \mathbb{I}_b)}{2} \right\} (\|\vec{q}_e\|^2 + \|\tilde{\Omega}\|^2) \quad (4.42)$$

Where the function  $\lambda_{\max}$  represents the maximum eigenvalue of its argument,  $\Gamma_3^{-1} \mathbb{I}_b$ . Similarly the negative definite LCF derivative is bound by the minimum:

$$\dot{V}_{XPD} \leq -\min \{ \lambda_{\min}(\Gamma_1), \lambda_{\min}(\Gamma_2 \Gamma_3^{-1}) \} (\|\vec{q}_e\|^2 + \|\tilde{\Omega}\|^2) \quad (4.43)$$

Therefore there exists some ratio  $\alpha$  that satisfies the relationship between the LCF and its derivative;  $\dot{V}_{XPD} \leq -\alpha V_{XPD}$ , where  $\alpha$  is defined as:

$$\alpha = \frac{\min \{ \lambda_{\min}(\Gamma_1), \lambda_{\min}(\Gamma_2 \Gamma_3^{-1}) \}}{\max \{ 2, \frac{\lambda_{\max}(\Gamma_3^{-1} \mathbb{I}_b)}{2} \}} \quad (4.44)$$

The attitude trajectory  $(\vec{q}_e(t), \tilde{\Omega}(t))$  is then exponentially bounded by:

$$(\|\vec{q}_e(t)\|, \|\tilde{\Omega}(t)\|) \leq M e^{-\beta t/2} (\|\vec{q}_e(0)\|, \|\tilde{\Omega}(0)\|) \quad (4.45)$$

*The stability proof for the auxiliary attitude controller was expanded upon and derived from McGilvray et al. [2006] [107] and adapted to fit attitude setpoint tracking. The fact that the auxiliary plant controller introduces the quaternion error, which is dependent on the quaternion scalar, dramatically improves controller performance. The exponential stability notably improves settling times and overshoot errors, seen next in Chapter:5.*

An earlier paper by Joshi, et al. [1995] [53] was the precursor for PD based attitude plants with asymptotic exponential stability. The control law first proposed didn't make use of any defined auxiliary plants, unlike [107], but equivalent terms were effectively incorporated. That control law developed for spacecraft attitude tracking proposed a very similar control scheme to  $\mu \vec{\tau}_{XPD}$ . That controller, when changed to the notational convention used above, designs body torque as:

$$\mu \vec{\tau}'_{XPD} = -\frac{1}{2} \left[ ([\vec{q}_e]_\times + q_0 \mathbb{I}_{3 \times 3}) \Gamma_1 + \alpha (1 - q_0 \mathbb{I}) \right] \vec{q}_e - \Gamma_2 \vec{\omega}_b \quad (4.46)$$

#### 4.4.3 Non-linear Controllers

Backstepping controllers(presented in [9, 56, 58],etc...) are a popular choice for non-linear attitude control plants. The process, through iterative design, enforces Lyapunov stability criteria to ensure asymptotic stability. In a report [114] Van Kampen, et al. [2008] describes fundamental backstepping algorithms. Ideal backstepping control is a precise control solution which requires exact plant matching, something that is difficult to achieve in practice. Another caveat of IBC control is poor disturbance rejection, being especially susceptible to plant uncertainty. The ideal backstepping algorithm can then be extended to incorporate non-idealities. The disturbance and uncertainty (*estimate error*) terms are incorporated into the LCF energy function. By Lyapunov's theorem their respective estimation error terms are stabilized.

#### Ideal Backstepping Controller

Starting with the ideal case for the first proposed backstepping controller, it's assumed the attitude plant described in Eq:3.60d, from the consolidated model in Sec:3.4, absolutely matches the dynamics of the physical prototype. The ideal backstepping controller aims to perfectly compensate for the plant's dynamic response to trajectory inputs. Ignoring any uncertainty associated with the dynamic equation, the aim here is to apply a stabilizing torque design. Recalling the quaternion tracking error from Eq:4.17;  $Q_e = Q_d^* \otimes Q_b$ . Then considering the first LCF proposal:

$$V_1(\vec{q}_e) = \vec{q}_e^T \vec{q}_e + (q_0 - 1)^2 \quad (4.47)$$

Which, after substituting in the quaternion derivatives and without using the quaternion simplification in Eq:4.24, has a Lie derivative:

$$\dot{V}_1 = 2\vec{q}_e^T \dot{\vec{q}}_e + 2(q_0 - 1)\dot{q}_0 \quad (4.48a)$$

$$= 2\vec{q}_e^T \frac{1}{2} ([\vec{q}_e]_{\times} + q_0 \mathbb{I}_{3 \times 3}) \vec{\omega}_e - 2(q_0 - 1) \frac{1}{2} \vec{q}_e^T \vec{\omega}_e \quad (4.48b)$$

$$= \vec{q}_e^T ([\vec{q}_e]_{\times} + q_0 \mathbb{I}_{3 \times 3}) \vec{\omega}_e - q_0 \vec{q}_e^T \vec{\omega}_e + \vec{q}_e^T \vec{\omega}_e \quad (4.48c)$$

$$= \vec{q}_e^T [\vec{q}_e]_{\times} \vec{\omega}_e + \vec{q}_e^T \vec{\omega}_e \quad (4.48d)$$

$$= -\vec{q}_e^T [\vec{q}_e]_{\times} \vec{\omega}_b - \vec{q}_e^T \vec{\omega}_b \quad (4.48e)$$

Then choosing the first stabilizing function  $z_1$  with a virtual backstepping control input  $\Omega_d$ . It's important to note that  $\Omega_d$  is used here to differentiate the backstepping *desired* value from the trajectory instructed  $\vec{\omega}_d$  from Eq:4.18a, or any auxiliary plants defined previously for the Auxiliary PD controller in Sec:4.4.2.

$$\vec{\omega}_b \Rightarrow \Omega_d = \Gamma_1 \vec{q}_e \quad (4.49)$$

Where  $\Gamma_1$  is the first symmetric positive definite coefficient matrix, a fact that is important to stress due to positive definite matrix's invertability. That stabilizing law then simplifies the LCF derivative  $\dot{V}_1$  to the negative definite term:

$$\dot{V}_1 = -\vec{q}_e^T [\vec{q}_e]_{\times} \Gamma_1 \Omega_d - \vec{q}_e^T \Omega_d \quad (4.50a)$$

$$= -\vec{q}_e^T [\vec{q}_e]_{\times} \Gamma_1 \vec{q}_e - \vec{q}_e^T \Gamma_1 \vec{q}_e \quad (4.50b)$$

$$= -\vec{q}_e^T \Gamma_1 \vec{q}_e \quad (4.50c)$$

However, that stabilizing virtual plant input  $\Omega_d$  has its own associated error,  $z_1$ , which then needs to be stabilized as well:

$$z_1 = \vec{\omega}_b - \Omega_d = \vec{\omega}_b - \Gamma_1 \vec{q}_e \quad (4.51a)$$

$$\rightarrow \vec{\omega}_b = z_1 - \Gamma_1 \vec{q}_e \quad (4.51b)$$

Introducing that error  $z_1$  into a second LCF, which expands the first proposed  $V_1$ :

$$V_2(\vec{q}_e, z_1) = V_1(\vec{q}_e) + \frac{1}{2} z_1^T \Gamma_1^{-1} z_1 \quad (4.52a)$$

$$= \vec{q}_e^T \vec{q}_e + (q_0 - 1)^2 + \frac{1}{2} z_1^T \Gamma_1^{-1} z_1 \quad (4.52b)$$

That first error  $z_1$  has its own derivative, and recalling  $\dot{\vec{\omega}}_b$  from earlier with an as yet undefined controllable input  $\mu\vec{\tau}$ :

$$\dot{z}_1 = \dot{\vec{\omega}}_b - \Gamma_1 \dot{\vec{q}}_e \quad (4.53a)$$

$$= \dot{\vec{\omega}}_b - \frac{\Gamma_1}{2} ([\vec{q}_e]_{\times} + q_0 \mathbb{I}_{3X3}) \vec{\omega}_e \quad (4.53b)$$

$$= \mathbb{I}_b^{-1} (-\vec{\omega}_b \times \mathbb{I}_b \vec{\omega}_b + \vec{\tau}_Q + \vec{\tau}_g + \vec{Q} + \mu\vec{\tau}) + \frac{\Gamma_1}{2} ([\vec{q}_e]_{\times} + q_0 \mathbb{I}_{3X3}) \vec{\omega}_b \quad (4.53c)$$

So then, following from Eq:4.53c, finding the derivative  $\dot{V}_2$ :

$$\begin{aligned} \dot{V}_2(\vec{q}_e, z_1) &= \vec{q}_e^T (z_1 - \Gamma_1 \vec{q}_e) + z_1^T \Gamma_1^{-1} \left( \mathbb{I}_b^{-1} (-\vec{\omega}_b \times \mathbb{I}_b \vec{\omega}_b + \vec{\tau}_Q + \vec{\tau}_g + \vec{Q} + \mu\vec{\tau}) \right. \\ &\quad \left. + \frac{\Gamma_1}{2} ([\vec{q}_e]_{\times} + q_0 \mathbb{I}_{3X3}) \vec{\omega}_b \right) \end{aligned} \quad (4.54a)$$

$$\begin{aligned} &= -\vec{q}_e^T \Gamma_1 \vec{q}_e + z_1^T \Gamma_1^{-1} \left( \Gamma_1 \vec{q}_e + \mathbb{I}_b^{-1} (\vec{\omega}_b \times \mathbb{I}_b \vec{\omega}_b + \vec{\tau}_Q + \vec{\tau}_g + \vec{Q} + \mu\vec{\tau}) \right. \\ &\quad \left. + \frac{\Gamma_1}{2} ([\vec{q}_e]_{\times} + q_0 \mathbb{I}_{3X3}) \vec{\omega}_b \right) \end{aligned} \quad (4.54b)$$

Then proposing the compensated stabilizing control law:

$$\mu\vec{\tau}_{IBC} = \vec{\omega}_b \times \mathbb{I}_b \vec{\omega}_b - \vec{\tau}_Q - \vec{\tau}_g - \vec{Q} - \mathbb{I}_b \Gamma_1 \vec{q}_e - \frac{\mathbb{I}_b \Gamma_1}{2} ([\vec{q}_e]_{\times} + q_0 \mathbb{I}_{3X3}) \vec{\omega}_b - \mathbb{I}_b \Gamma_2 z_1 \quad (4.55)$$

With  $\Gamma_2$  being another positive definite symmetric coefficient matrix. Then with the control law  $\mu\vec{\tau}_{IBC}$  introduced into the LCF derivative  $\dot{V}_2$  reduces to negative definite:

$$\dot{V}_2 = -\vec{q}_e^T \Gamma_1 \vec{q}_e - z_1^T \Gamma_2 z_1 \leq 0 \quad \forall (\vec{q}_e, z_1) \quad (4.56)$$

As such  $\vec{q}_e \rightarrow 0$  &  $q_0 \rightarrow 1$  as  $t \rightarrow \infty$ . Similarly  $z_1 \rightarrow 0$ , which leads to the limit:

$$\lim_{t \rightarrow \infty} (\vec{\omega}_b - \Gamma_1 \vec{q}_e) = 0 \quad (4.57)$$

Because the quaternion error vector already tends to 0;  $\vec{q}_e \rightarrow 0$ , it follows that  $\vec{\omega}_b \rightarrow 0$ . It can also be said that, from the definition of  $\vec{\omega}_e$ , that the angular velocity error stabilizes too. There is a distinct similarity in the structure of  $\mu\vec{\tau}_{IBC}$  from Eq:4.55 and that of the auxiliary PD controller presented in Eq:4.30. Furthermore, using the same reasoning from Eq:4.41, the exponential stability proof then follows:

$$V_{IBC} \leq V_2 = 2 \|\vec{q}_e\|^2 + \frac{\Gamma_1^{-1}}{2} \|z_1\|^2 \quad (4.58a)$$

$$\dot{V}_{IBC} = \dot{V}_2 = -\Gamma_1 \|\vec{q}_e\|^2 - \Gamma_2 \|z_1\|^2 \quad (4.58b)$$

Then both the energy function and its derivative are bound respectively by:

$$V_{IBC} \leq \max \left\{ 2, \frac{\lambda_{\max}(\Gamma_1^{-1})}{2} \right\} (\|\vec{q}_e\|^2 + \|z_1\|^2) \quad (4.59a)$$

$$\dot{V}_{IBC} \leq \min \{ \lambda_{\min}(\Gamma_1), \lambda_{\min}(\Gamma_2) \} (\|\vec{q}_e\|^2 + \|z_1\|^2) \quad (4.59b)$$

Which then leads to a similar exponential stability trajectory boundedness such that:

$$\dot{V}_{IBC} \leq \alpha V_{IBC} \quad (4.60a)$$

$$\therefore (\|\vec{q}_e(t)\|, \|z_1(t)\|) \leq M e^{-\alpha t/2} (\|\vec{q}_e(0)\|, \|z_1(0)\|) \quad (4.60b)$$

## Adaptive Backstepping Controller

As effective as the control law defined above in Section:4.4.3 may be, it lacks suitable disturbance rejection properties. Any plant uncertainties or disturbances encountered would adversely affect the controller in a dramatic manner (Sec:5.4). Introducing a term for lumped uncertainty/disturbance torques,  $\vec{L}$ , into the dynamic equations leads to:

$$\dot{\vec{\omega}}_b = \mathbb{I}_b^{-1}(-\vec{\omega}_b \times \mathbb{I}_b \vec{\omega}_b + \vec{\tau}_Q + \vec{\tau}_g + \vec{Q} + \vec{L} + \mu \vec{\tau}) \quad (4.61)$$

It would obviously be easy to merely introduce a compensation term for  $\vec{L}$  into the control law. In practice, however, it is very difficult to approximate a disturbance term without *a priori* knowledge about any of its properties. Noise compensation in sensors can be done easily due to the known frequency band which that noise occurs in, the same cannot be said for wind disturbances and the like.

An approximate estimation term  $\hat{L}$  has to be used for that disturbance compensation in the designed control torque  $\mu \vec{\tau}$ . That estimate term is then going to have its own error from the true disturbance affecting the system:

$$\tilde{L} = \vec{L} - \hat{L} \quad (4.62)$$

The purpose of adaptive backstepping is to introduce that estimate error term into an LCF and develop a derivative term for  $\dot{\hat{L}}$ , or a disturbance update law, such that even the estimate error asymptotically stabilizes. Typically, that disturbance update rule is the contribution of satellite and general attitude control papers. Similar terms can be introduced for plant uncertainty which can similarly be adapted for but are not included here...

The estimate error is then introduced into the LCF from an ideal backstepping control, in order for it to be dissipated as per Lyapunov theorem.

$$V_{ABC}(\vec{q}_e, z_1, \tilde{L}) = V_{IBC}(\vec{q}_e, z_1) + \frac{1}{2} \tilde{L}^T \Gamma_L^{-1} \tilde{L} \quad (4.63a)$$

$$= \vec{q}_e^T \vec{q}_e + (q_0 - 1)^2 + \frac{1}{2} z_1^T \Gamma_1^{-1} z_1 + \frac{1}{2} \tilde{L}^T \Gamma_L^{-1} \tilde{L} \quad (4.63b)$$

Where the positive symmetric matrix  $\Gamma_L \geq 0 \in \mathbb{R}^{3 \times 3}$  is termed as the adaptation gain coefficient matrix. Those particular coefficients determine how responsive the system is to disturbances and the rate at which it adapts to compensate for them. Then, to prove stability one starts with the Lie derivative  $\dot{V}_{ABC}$ :

$$\dot{V}_{ABC}(\vec{q}_e, z_1, \tilde{L}) = \dot{V}_{IBC}(\vec{q}_e, z_1) + \frac{1}{2} \dot{\tilde{L}}^T \Gamma_L^{-1} \tilde{L} + \frac{1}{2} \tilde{L}^T \Gamma_L^{-1} \dot{\tilde{L}} \quad (4.64)$$

Recalling the definition of  $\tilde{L}$  from Eq:4.62. For the derivative  $\dot{\tilde{L}}$  its reasonable to assume the dynamics of the physical disturbance  $\vec{L}$  are far slower than the time constant of the control system, or that  $\dot{\tilde{L}} \approx \vec{0}$ . Then it follows:

$$\dot{\tilde{L}} = \dot{\vec{L}} - \dot{\hat{L}} \approx \vec{0} - \dot{\hat{L}} = -\dot{\hat{L}} \quad (4.65)$$

Then, substituting that estimation error rate back into the derivative  $\dot{V}_{ABC}$ , which expands upon Eq:4.54, yields:

$$\begin{aligned} \dot{V}_{ABC}(\vec{q}_e, z_1, \tilde{L}) &= \vec{q}_e^T (z_1 - \Gamma_1 \vec{q}_e) + z_1^T \Gamma_1^{-1} \left( \mathbb{I}_b^{-1} (-\vec{\omega}_b \times \mathbb{I}_b \vec{\omega}_b + \vec{\tau}_Q + \vec{\tau}_g + \vec{Q} + \vec{L} + \mu \vec{\tau}) \right. \\ &\quad \left. + \frac{\Gamma_1}{2} ([\vec{q}_e]_\times + q_0 \mathbb{I}_{3 \times 3}) \vec{\omega}_b \right) - \tilde{L}^T \Gamma_L^{-1} \dot{\hat{L}} \end{aligned} \quad (4.66a)$$

And using a similar control law to  $\mu \vec{\tau}_{IBC}$ , which has a disturbance estimate compensation term:

$$\mu \vec{\tau}_{ABC} = \vec{\omega}_b \times \mathbb{I}_b \vec{\omega}_b - \vec{\tau}_Q - \vec{\tau}_g - \vec{Q} - \hat{L} - \mathbb{I}_b \Gamma_1 \vec{q}_e - \frac{\Gamma_1 \mathbb{I}_b}{2} ([\vec{q}_e]_\times + q_0 \mathbb{I}_{3 \times 3}) \vec{\omega}_b - \mathbb{I}_b \Gamma_2 z_1 \quad (4.67a)$$

Which reduces the energy function's derivative to:

$$\dot{V}_{ABC} = -\vec{q}_e^T \Gamma_1 \vec{q}_e - z_1^T \Gamma_2 z_1 + z_1^T \Gamma_1^{-1} \left( \mathbb{I}_b^{-1} (\vec{L} - \hat{L}) \right) - \tilde{L}^T \Gamma_L^{-1} \dot{\hat{L}} \quad (4.67b)$$

$$= -\vec{q}_e^T \Gamma_1 \vec{q}_e - z_1^T \Gamma_2 z_1 + z_1^T (\Gamma_1^{-1} \mathbb{I}_b^{-1}) \tilde{L} - \tilde{L}^T \Gamma_L^{-1} \dot{\hat{L}} \quad (4.67c)$$

$$= -\vec{q}_e^T \Gamma_1 \vec{q}_e - z_1^T \Gamma_2 z_1 + \tilde{L}^T \Gamma_L^{-1} (\Gamma_1^{-1} \Gamma_L \mathbb{I}_b^{-1} z_1 - \dot{\hat{L}}) \quad (4.67d)$$

The decision then needs to be made as to how the disturbance estimate is going to be updated, or what  $\dot{\hat{L}}$  is defined as. The clear choice would be to compensate for the final term in the LCF, making it purely negative definite:

$$\dot{\hat{L}} = \Gamma_1^{-1} \Gamma_L \mathbb{I}_b^{-1} z_1 = \Gamma_1^{-1} \Gamma_L \mathbb{I}_b^{-1} \vec{\omega}_b - \Gamma_L \mathbb{I}_b^{-1} \vec{q}_e \quad (4.68)$$

The disturbance is therefore compensated for and the estimate error is ensured to have asymptotic stability seeing that  $V_{ABC}$  is positive definite.

$$\dot{V}_{ABC} = -\vec{q}_e^T \Gamma_1 \vec{q}_e - z_1^T \Gamma_2 z_1 < \vec{0} \quad \forall (\vec{q}_e, z_1, \tilde{L}) \quad (4.69)$$

Exponential stability for the plant however cannot be proven with the above control and disturbance laws, there is no non-zero estimate error coefficient in the LCF derivative. A lot of work has been done on the statistical nature of disturbance approximation and how best to adapt a non-linear control system to the influence of unwanted disturbances. An interesting approach would be to use the previous disturbance estimate,  $\vec{L} = \hat{L}_{n-1}$ , such that:

$$\tilde{L}' = \vec{L} - \hat{L} = (\hat{L}_{n-1} - \hat{L}_n) \quad (4.70a)$$

$$\dot{\tilde{L}'} = \Gamma_1^{-1} \Gamma_L \mathbb{I}_b^{-1} z_1 + \tilde{L}' \quad (4.70b)$$

$$\dot{\hat{L}} = \Gamma_1^{-1} \Gamma_L \mathbb{I}_b^{-1} \vec{\omega}_b - \Gamma_L \mathbb{I}_b^{-1} \vec{q}_e + (\hat{L}_{n-1} - \hat{L}_n) \quad (4.70c)$$

$$\therefore \dot{V}'_{ABC} = -\vec{q}_e^T \Gamma_1 \vec{q}_e - z_1^T \Gamma_2 z_1 - \tilde{L}'^T \Gamma_L^{-1} (\hat{L}_{n-1} - \hat{L}_n) \quad (4.70d)$$

Given that the starting estimate  $\hat{L}_0 = \vec{0}$  and that the change of disturbance over a single control cycle is going to be small once the approximator has settled, its fair to assume the following:

$$\lim_{t \rightarrow \infty} \tilde{L}' = (\hat{L}_{n-1} - \hat{L}_n) \rightarrow \tilde{L} \quad (4.71)$$

Then, it leads to the following LCF derivative which can then prove exponential stability. It clear that a coefficient  $\dot{V}_{ABC} \leq \alpha V_{ABC}$  exists and can be found:

$$\dot{V}_{ABC}(\vec{q}_e, z_1, \tilde{L}) = -\vec{q}_e^T \Gamma_1 \vec{q}_e - z_1^T \Gamma_2 z_1 - \tilde{L}^T \Gamma_L^{-1} \tilde{L} \quad (4.72)$$

The assumption in Eq:4.71 is going to need to be tested in simulation later in Chapter:5; the adaptive gain matrix  $\Gamma_L$  is something that will similarly need to be designed. For control coefficients a separate optimization loop will be run, later disturbance will be introduced and the adaptive gain will independently be attained.

## 4.5 Position Control

Only two control laws for position control are proposed. Due to the nature of Coriolis cross-coupling, an attitude plant can be dealt with independently from the position plant, the inverse is however not true. A basic Proportional-Derivative control structure is presented as the reference case, thereafter a more complicated adaptive backstepping control algorithm is derived...

The dynamics for position control, Eq:3.60b, include a coupled angular velocity element.

$$\dot{\vec{v}}_b = m^{-1}(-\vec{\omega}_b \times m\vec{v}_b + Q_b^* \otimes m\vec{G}_I \otimes Q_b + \mu\vec{F}) \in \mathcal{F}^b \quad (4.73)$$

Typically, given the standard operating conditions of a quadrotor, it's assumed that  $\vec{\omega}_b \approx \vec{0}$ . As such the inherent angular velocity coupled dynamics are negligible;  $\vec{\omega}_b \times m\vec{v}_b \approx 0$ . If the entire state vector, both attitude and position  $\mathbf{x}(t) = [\mathcal{E}, Q_b]^T$ , of the plant is known then it's easy to compensate for those dynamics rather than making assumptions about their influence on the system given particular operating conditions. That plant dependency can be introduced in the control force  $\mu\vec{F}$ .

The translational velocity,  $\vec{v}_b$ , defined in the body frame is related to the inertial frame through a quaternion transformation:

$$\dot{\mathcal{E}} = Q_b \otimes \vec{v}_b \otimes Q_b^* \in \mathcal{F}^I \quad (4.74)$$

The difference in reference frames is an important distinction between the position and attitude control loops. Position error is calculated purely as a subtractive term:

$$\mathcal{E}_e = \mathcal{E}_d - \mathcal{E}_b \in \mathcal{F}^I \quad (4.75)$$

With  $\mathcal{E}_d(t)$  being some desired position designed by the trajectory generation system. Translational velocity error can be similarly calculated but, in the same way angular velocity  $\vec{\omega}_d = \vec{0}$ , the desired translational velocity is zero.

$$\dot{\mathcal{E}}_e = \dot{\mathcal{E}}_d - \dot{\mathcal{E}}_b = -\dot{\mathcal{E}}_b|_{\dot{\mathcal{E}}_d=\vec{0}} \quad (4.76)$$

The objective for position setpoint tracking is analogous to that of the attitude setpoint tracking. In particular the aim is to produce a stabilizing control law that ensures the position tracking error asymptotically tends to  $\vec{0}$ :

$$\mu\vec{F} = g(\mathcal{E}_e, \dot{\mathcal{E}}_e) \text{ such that } \lim_{t \rightarrow \infty} \mathcal{E}_e = \vec{0} \quad (4.77)$$

Where  $\mu\vec{F}$  is the control force to effect Eq:4.73  $\in \mathcal{F}^b$ .

#### 4.5.1 PD Controller

Starting with a simple PD structure to use as a reference case. A plant dependent controller designs the net force proportional to both the position error and the first derivative velocity error<sup>11</sup>.

$$\mu\vec{F}_{PD} = K\dot{\mathcal{E}}_e + \alpha\mathcal{E}_e + \vec{\omega}_b \times \vec{v}_b - \vec{G}_b \in \mathcal{F}^b \quad (4.78)$$

For the stability proof the error states must be transformed to the body frame  $\mathcal{F}^b$  such that the control input and error states all act in a common frame. So defining an error state in the body frame  $X_e$ :

$$X_e = Q_b^* \otimes (\mathcal{E}_d - \mathcal{E}_b) \otimes Q_b \quad (4.79a)$$

$$\dot{X}_e = Q_b^* \otimes (\dot{\mathcal{E}}_d - \dot{\mathcal{E}}_b) \otimes Q_b = -Q_b^* \otimes \dot{\mathcal{E}}_b \otimes Q_b = -\vec{v}_b \quad (4.79b)$$

As such the control law from Eq:4.78, despite being  $\in \mathcal{F}^b$  has arguments  $\in \mathcal{F}^I$ , and so must similarly transform to:

$$\mu\vec{F}_{PD} = K\dot{X}_e + \alpha X_e + \vec{\omega}_b \times m\vec{v}_b - \vec{G}_b \quad (4.80a)$$

$$= -K\vec{v}_b + \alpha X_e + \vec{\omega} \times m\vec{v}_b - \vec{G}_b \quad (4.80b)$$

Then using a Lyapunov candidate function:

$$V_{PD}(X_e, \dot{X}_e) = \frac{\alpha}{2} X_e^T X_e + \frac{m}{2} \dot{X}_e^T \dot{X}_e = \frac{\alpha}{2} X_e^T X_e + \frac{m}{2} \vec{v}_b^T \vec{v}_b \quad (4.81)$$

---

<sup>11</sup>The same P and D coefficient symbols are used for continuity.

Then calculating the LCF derivative with the PD control law substituted:

$$\dot{V}_{PD} = \alpha X_e^T \dot{X}_e + \vec{v}_b^T m \dot{\vec{v}}_b = -\alpha X_e^T \vec{v}_b + \vec{v}_b^T m \dot{\vec{v}}_b \quad (4.82a)$$

$$= -\alpha X_e^T \vec{v}_b + \vec{v}_b^T (-\vec{\omega}_b \times m \vec{v}_b + \vec{G}_b + \mu \vec{F}_{PD}) \quad (4.82b)$$

$$= -\alpha X_e^T \vec{v}_b + \vec{v}_b^T (-K \vec{v}_b + \alpha X_e) \quad (4.82c)$$

$$\Rightarrow \dot{V}_{PD} = -K \vec{v}_b^T \vec{v}_b < 0 \quad \forall (X_e, \dot{X}_e) \quad (4.82d)$$

It then follows that the following asymptotically<sup>12</sup> stabilizing limits exist:

$$\lim_{t \rightarrow \infty} X_e = Q_b^* \otimes (\mathcal{E}_d - \mathcal{E}_b) \otimes Q_b = \vec{0} \quad (4.83a)$$

$$\therefore \lim_{t \rightarrow \infty} \mathcal{E}_b = \mathcal{E}_d \quad (4.83b)$$

$$\lim_{t \rightarrow \infty} \dot{X}_e = Q_b^* \otimes (\dot{\mathcal{E}}_d - \dot{\mathcal{E}}_b) \otimes Q_b = -\vec{v}_b = 0 \quad (4.83c)$$

#### 4.5.2 Adaptive Backstepping Controller

An adaptive backstepping algorithm, similar the attitude controller derived previously in Sec:4.4.3, is now applied to position control. The disturbance term,  $\vec{D} \in \mathcal{F}^b$ , introduced to the differential Eq:4.73 represents drag and wind forces encountered by the body which weren't quantified numerically in Sec:3.3.3. The backstepping iterations of the position control loop first need to stabilize the position error and then compensate for disturbances...

$$\dot{\vec{v}}_b = m^{-1} (-\vec{\omega}_b \times m \vec{v}_b + \vec{G}_b + \vec{D}_b + \mu \vec{F}) \in \mathcal{F}^b \quad (4.84)$$

Obviously the compensation for  $\vec{D}$  is going to be an approximation of that disturbance term;  $\hat{D}$ . Beginning the backstepping process for position with the position tracking error state:

$$z_1 = \mathcal{E}_d - \mathcal{E}_b \quad (4.85)$$

Which then has a derivative:

$$\dot{z}_1 = \dot{\mathcal{E}}_d - \dot{\mathcal{E}}_b = Q_b \otimes (\vec{0} - \vec{v}_b) \otimes Q_b^* = -Q_b \otimes \vec{v}_b \otimes Q_b^* \quad (4.86)$$

Transforming that error,  $z_1$ , to the body frame  $\mathcal{F}^b$ , in the same way as Eq:4.79a, makes the stability proof more concise. The transformation doesn't affect the Lie derivative as the energy function's gradient depends on its partial derivative w.r.t it's trajectory, namely  $\mathcal{E}_e(t)$ .

$$\hat{z}_1 = X_e = Q_b^* \otimes z_1 \otimes Q_b = Q_b^* \otimes (\mathcal{E}_d - \mathcal{E}_b) \otimes Q_b \quad (4.87a)$$

$$\therefore \dot{\hat{z}}_1 = Q_b^* \otimes \dot{z}_1 \otimes Q_b = Q_b^* \otimes (\dot{\mathcal{E}}_d - \dot{\mathcal{E}}_b) \otimes Q_b = -\vec{v}_b \quad (4.87b)$$

Then proposing the first positive definite LCF  $V_1$  in terms of that tracking error:

$$V_1(\hat{z}_1) = \frac{1}{2} \hat{z}_1^T \hat{z}_1 \quad (4.88a)$$

$$\Rightarrow \dot{V}_1 = \hat{z}_1^T \dot{\hat{z}}_1 = -\hat{z}_1^T \vec{v}_b \quad (4.88b)$$

Then the first stabilizing velocity function<sup>13</sup>,  $\Omega_d$ , and its associated error,  $\hat{z}_2$ , can be defined as:

$$\vec{v}_b \Rightarrow \Omega_d = \Gamma_1 \hat{z}_1 \quad (4.89a)$$

---

<sup>12</sup>Not exponentially stabilizing however.

<sup>13</sup>Using  $\Omega_d$  to differentiate from  $\vec{v}_d$  which would otherwise be the translational velocity produced from the desired trajectory...

$$\hat{z}_2 = \Omega_d - \vec{v}_b = \Gamma_1 \hat{z}_1 - \vec{v}_b \quad (4.89b)$$

$$\therefore \vec{v}_b = \Gamma_1 \hat{z}_1 - \hat{z}_2 \quad (4.89c)$$

So that second error state  $\hat{z}_2$  has a derivative:

$$\dot{\hat{z}}_2 = \dot{\Omega}_d - \dot{\vec{v}}_b = \Gamma_1 \dot{\hat{z}}_1 - m^{-1}(-\vec{\omega}_b \times m\vec{v}_b + \vec{G}_b + \vec{D}_b + \mu\vec{F}) \quad (4.90a)$$

$$= -\Gamma_1 \vec{v}_b - m^{-1}(-\vec{\omega}_b \times m\vec{v}_b + \vec{G}_b + \vec{D}_b + \mu\vec{F}) \quad (4.90b)$$

So introducing that second error to a new LCF  $V_2$ :

$$V_2(\hat{z}_1, \hat{z}_2) = V_1(\hat{z}_1) + \frac{1}{2} \hat{z}_2^T \hat{z}_2 = \frac{1}{2} \hat{z}_1^T \hat{z}_1 + \frac{1}{2} \hat{z}_2^T \hat{z}_2 \quad (4.91)$$

Which has a derivative:

$$\dot{V}_2 = \hat{z}_1^T \dot{\hat{z}}_1 + \hat{z}_2^T \dot{\hat{z}}_2 = -\hat{z}_1^T \vec{v}_b + \hat{z}_2^T \dot{\hat{z}}_2 \quad (4.92a)$$

$$= -\hat{z}_1^T \vec{v}_b + \hat{z}_2^T \left( -\Gamma_1 \vec{v}_b - m^{-1}(-\vec{\omega}_b \times m\vec{v}_b + \vec{G}_b + \vec{D}_b + \mu\vec{F}) \right) \quad (4.92b)$$

And substituting Eq:4.89c into only the first energy term of the LCF derivative:

$$= -\hat{z}_1^T (\Gamma_1 \hat{z}_1 - \hat{z}_2) + \hat{z}_2^T \left( -\Gamma_1 \vec{v}_b - m^{-1}(-\vec{\omega}_b \times m\vec{v}_b + \vec{G}_b + \vec{D}_b + \mu\vec{F}) \right) \quad (4.92c)$$

$$= -\hat{z}_1^T \Gamma_1 \hat{z}_1 + \hat{z}_2^T \left( -\hat{z}_1 - \Gamma_1 \vec{v}_b - m^{-1}(-\vec{\omega}_b \times m\vec{v}_b + \vec{G}_b + \vec{D}_b + \mu\vec{F}) \right) \quad (4.92d)$$

An ideal backstepping control law, with the assumption that  $\vec{D}_b$  is known, is then:

$$\mu\vec{F}_{IBC} = \vec{\omega}_b \times m\vec{v}_b - \vec{G}_b - \vec{D}_b - m\hat{z}_1 - m\Gamma_1 \vec{v}_b + m\Gamma_2 \hat{z}_2 \quad (4.93a)$$

$$= \vec{\omega}_b \times m\vec{v}_b - \vec{G}_b - \vec{D}_b + (\Gamma_1 \Gamma_2 - m)\hat{z}_1 - m(\Gamma_1 + \Gamma_2)\vec{v}_b \quad (4.93b)$$

$$\Rightarrow \dot{V}_{IBC} = \dot{V}_2 = -\hat{z}_1^T \Gamma_1 \hat{z}_1 - \hat{z}_2^T \Gamma_2 \hat{z}_2 \leq \vec{0} \quad \forall (\hat{z}_1, \hat{z}_2) \& \forall (z_1, z_2) \quad (4.93c)$$

Which obviously leads to asymptotic (*extended to exponential*) stability under the assumption that the disturbance term  $\vec{D}_b$  is known and can be compensated for well. In the controller both  $\Gamma_1$  &  $\Gamma_2$  are P.D symmetric control coefficients to be determined later...

Adjusting the backstepping rule and proposed LCF to include a disturbance approximation  $\hat{D}$ , similar to the adaptive backstepping attitude controller in Sec:4.4.3. That approximation leads to an error state and adjusted control law respectively, once again assuming the true disturbance derivative  $\dot{\vec{D}}_b$  is far slower than the control dynamics,  $\dot{\vec{D}}_b \approx \vec{0}$ .

$$\tilde{D} = \vec{D}_b - \hat{D} \quad (4.94a)$$

$$\dot{\tilde{D}} = \dot{\vec{D}}_b - \dot{\hat{D}} = \vec{0} - \dot{\hat{D}} \quad (4.94b)$$

$$\rightarrow \mu\vec{F}_{ABC} = \vec{\omega}_b \times m\vec{v}_b - \vec{G}_b - \hat{D} - m\hat{z}_1 - m\Gamma_1 \vec{v}_d + m\Gamma_2 \hat{z}_2 \quad (4.94c)$$

$$= \vec{\omega}_b \times m\vec{v}_b - \vec{G}_b - \hat{D} + (\Gamma_1 \Gamma_2 - m)\hat{z}_1 - m(\Gamma_1 + \Gamma_2)\vec{v}_b \quad (4.94d)$$

Then proposing an LCF which incorporates that disturbance estimation error  $\tilde{D}$ .

$$V_{ABC} = \frac{1}{2} \hat{z}_1^T \hat{z}_1 + \frac{1}{2} \hat{z}_2^T \hat{z}_2 + \frac{1}{2} \tilde{D}^T \Gamma_D^{-1} \tilde{D} \quad (4.95a)$$

$$\Rightarrow \dot{V}_{ABC} = \hat{z}_1^T \dot{\hat{z}}_1 + \hat{z}_2^T \dot{\hat{z}}_2 + \tilde{D}^T \Gamma_D^{-1} \dot{\tilde{D}} \quad (4.95b)$$

$$= -\hat{z}_1^T \Gamma_1 \hat{z}_1 + \hat{z}_2^T \left( -\hat{z}_1 - \Gamma_1 \vec{v}_b - m^{-1}(-\vec{\omega}_b \times m\vec{v}_b + \vec{G}_b + \vec{D}_b + \mu\vec{F}_{ABC}) \right) - \tilde{D} \Gamma_D^{-1} \dot{\tilde{D}} \quad (4.95c)$$

$$= -\hat{z}_1^T \Gamma_1 \hat{z}_1 + \hat{z}_2^T \left( -\Gamma_2 \hat{z}_2 - m^{-1} (\vec{D}_b - \hat{D}) \right) - \tilde{D}^T \Gamma_D^{-1} \dot{\hat{D}} \quad (4.95d)$$

$$= -\hat{z}_1^T \Gamma_1 \hat{z}_1 - \hat{z}_2^T \Gamma_2 \hat{z}_2 - \hat{z}_2^T m^{-1} \tilde{D} - \tilde{D}^T \Gamma_D^{-1} \dot{\hat{D}} \quad (4.95e)$$

$$= -\hat{z}_1^T \Gamma_1 \hat{z}_1 - \hat{z}_2^T \Gamma_2 \hat{z}_2 - \tilde{D}^T \Gamma_D^{-1} (m^{-1} \Gamma_D \hat{z}_2 + \dot{\hat{D}}) \quad (4.95f)$$

Then, an obvious choice for the disturbance update law would be;  $\dot{\hat{D}} = -m^{-1} \Gamma_D \hat{z}_2$ , which would ensure asymptotic stability. Expanding on that, an interesting option which could potentially enforce exponential stability would be to use  $\hat{D}_{n-1}$  as a disturbance estimate:

$$\dot{\hat{D}} = -m^{-1} \Gamma_D \hat{z}_2 + (\hat{D}_{n-1} - \hat{D}) \quad (4.96a)$$

$$\therefore \dot{V}_{ABC} = -\hat{z}_1^T \Gamma_1 \hat{z} - \hat{z}_2^T \Gamma_2 \hat{z}_2 - \tilde{D}^T \Gamma_D^{-1} (\hat{D}_{n-1} - \hat{D}_n) \quad (4.96b)$$

$$\approx -\hat{z}_1^T \Gamma_1 \hat{z}_1 - \hat{z}_2^T \Gamma_2 \hat{z}_2 - \tilde{D}^T \Gamma_D^{-1} \tilde{D} \quad (4.96c)$$

Similarly to the suggested exponentially stable adaptive backstepping controller for the attitude plant, using  $\hat{D}_{n-1}$  for an existing disturbance estimate will need to be simulated in order to ascertain if it's a suitable conjecture. Note here that adaptive control laws refer to adaptability to unknown disturbances and not plant model uncertainty which would take a different approach to the backstepping algorithm.

## 4.6 Controller Allocation

Following the higher level control laws, a distribution algorithm is needed to *allocate* out the desired virtual control inputs,  $\vec{v}_d = [\mu \vec{F} \mu \vec{r}]^T$ , to commanded actuator positions,  $u_c \in \mathbb{U}$ . The allocator block,  $B^\dagger(\mathbf{x}, \vec{v}_d, t)$ , from the control loop, Fig:4.1, constructs physical actuator positions from the virtual control input. For regular, unconstrained control allocation the solution is posed as an optimization<sup>14</sup> problem; aiming to minimize deviation between the virtual and commanded control inputs,  $\vec{v}_d$  &  $\vec{v}_c$  respectively.

$$\min_{u \in \mathbb{U}^{12}, s \in \mathbb{R}^6} (||Q_s||) \text{ such that } \vec{v}_d - \vec{v}_c = h(\mathbf{x}_e, t) - B(\mathbf{x}, t, u) = s \quad (4.97)$$

Where  $Q_s$  is some cost function to prioritize the slack variable,  $s$ , requirements. Typically that cost function will just be the  $L_2$  norm of the slack. In the over-actuated case, there exists an entire set of suitable actuator positions  $u$  which are all solutions to Eq:4.97. The allocation rule is then to introduce a secondary cost function,  $J(\mathbf{x}, t, u)$  into the optimization problem of Eq:4.97.

$$\min_{u \in \mathbb{U}^{12}, s \in \mathbb{R}^6} (||Q_s|| + J(\mathbf{x}, u, t)) \text{ such that } h(\mathbf{x}_e, t) - B(\mathbf{x}, u, t) = s \quad (4.98)$$

That secondary control objective  $J(\mathbf{x}, t, u)$  and an associated solution to Eq:4.98 is the subject of control allocation. Not much work has been done on over-allocation for aerospace vehicles outside the field of satellite attitude control (Section:1.2.2 for examples). Often satellites are over actuated for the sake of fault tolerance and redundancy [6,65]. Actuator rate constraints can be further introduced such that  $u$  is limited by  $\Delta u$ , constraining sequential actuator position changes.

$$\therefore \min_{u \in \mathbb{U}^{12}, s \in \mathbb{R}^6} (||Q_s|| + J(\mathbf{x}, u, t)) \text{ s.t } h(\mathbf{x}_e, t) - B(\mathbf{x}, u, t) = s \\ \text{subject to } u = u_{n-1} + \Delta u, \Delta u \in \mathbb{C} \quad (4.99)$$

Most control allocation paradigms all assume a linear, multiplicative relationship with the effectiveness function, hence the abstraction layer which was introduced previously in Eq:4.7. The allocator effectiveness function can be abstracted to a matrix multiplication relationship:

$$\vec{v}_d = h(\mathbf{x}_e, t) \iff B(\mathbf{x}, u, t) = B(\mathbf{x}, t)u = \vec{v}_c \quad (4.100)$$

---

<sup>14</sup>Control Allocation by Johansen, et al. [2012] [50] and Control allocation for over actuated systems by Oppenheimer, et al. [2006] [80] both detail the nature of generalized nonlinear allocation loops.

With  $\vec{\nu} \in \mathbb{R}^n$ ,  $u \in (U) \in \mathbb{R}^m$ ,  $B \in \mathbb{R}^{m \times n}$ . That assumption makes addressing the allocation conceptually simpler, accommodating use of inversion laws (Section:4.6.1,4.6.2,4.6.3). That abstraction to a multiplicative relationship was suggested in Eq:4.7 however the subsequent rotation "inversion" function,  $R^\dagger(\mathbf{x}, \vec{F}_i, t)$ , to solve for physical actuator positions  $(\Omega_i, \lambda_i, \alpha_i)$  is as yet undefined.

Assuming for the moment there is some allocation rule that, from  $\vec{\nu}_d$ , designs well four stabilizing 3-dimensional thrust vectors  $\vec{T}_{1 \rightarrow 4}$ . It then follows that each of those four vectors then relate<sup>15</sup> to their individual associated actuator positions through a quaternion transformation:

$$\vec{T}_i = Q_z(-\sigma_i)Q_y(-\alpha_i)Q_x(-\lambda_i) \otimes \vec{T}(\Omega_i) \otimes Q_x^*(-\lambda_i)Q_y^*(-\alpha_i)Q_z^*(-\sigma_i) \quad \in \mathcal{F}^b \quad (4.101a)$$

$$\vec{T}(\Omega_i) = \begin{bmatrix} 0 \\ 0 \\ T(\Omega_i) \end{bmatrix} = \begin{bmatrix} 0 \\ 0 \\ C_T(J)\rho\Omega_i^2 D^4 \end{bmatrix} \quad \in \mathcal{F}^{M_i} \quad (4.101b)$$

Where  $\sigma_i$  is the orthogonal  $\hat{Z}$  transformation from  $\mathcal{F}^b \rightarrow \mathcal{F}^{M_i}$  from Eq:2.9a. The thrust function  $T(\Omega_i)$  is the BEM theory equation using thrust coefficients, Eq:3.62a, in the  $\hat{Z}_{M_i}$  direction.

Seeing that quaternion rotation (*transformation*) operators change the reference frame whilst retaining the vector operand's magnitude, it follows that  $T(\Omega_i)$ , and by extension the propeller speed,  $\Omega_i$ , can be solved as:

$$|\vec{T}_i| = \sqrt{||[T_x \ T_y \ T_z]^T||} = \sqrt{T_x^2 + T_y^2 + T_z^2} = |T(\Omega_i)| = |C_T(J)\rho\Omega_i^2 D^4| \quad (4.102a)$$

$$\Rightarrow \Omega_i = \sqrt{\frac{|\vec{T}_i|}{C_T(J)\rho D^4}} = \sqrt{\frac{\sqrt{T_x^2 + T_y^2 + T_z^2}}{C_T(J)\rho D^4}} \quad (4.102b)$$

Then attempting to undo and reverse the transformation from motor module to body frame in Eq:4.101a:

$$\vec{T}(\Omega_i) = Q_z^*(-\sigma_i)Q_y^*(-\alpha_i)Q_x^*(-\lambda_i) \otimes \vec{T}_i \otimes Q_x(-\lambda_i)Q_y(-\alpha_i)Q_z(-\sigma_i) \quad \in \mathcal{F}^{M_i} \quad (4.103a)$$

$$\rightarrow \vec{T}(\Omega_i) = Q_{M_i}^* \otimes \vec{T}_i \otimes Q_{M_i} \quad \in \mathcal{F}^{M_i} \quad (4.103b)$$

Knowing only  $\vec{T}(\Omega_i)$  and  $\vec{T}_i$  in the motor frame and body frame respectively requires solving for a quaternion which relates the two. If both vectors are of unit length,  $\hat{T}_i$  &  $\hat{T}(\Omega_i)$ ; then the following relationship can be exploited:

$$\hat{T}_i = \frac{\vec{T}_i}{|\vec{T}_i|} = \frac{\vec{T}_i}{\sqrt{T_x^2 + T_y^2 + T_z^2}} \quad \in \mathcal{F}^b \quad (4.104a)$$

$$\hat{T}(\Omega_i) = \frac{\vec{T}(\Omega_i)}{|\vec{T}(\Omega_i)|} = \frac{\vec{T}(\Omega_i)}{|C_T(J)\rho\Omega^2 D^4|} = [0 \ 0 \ 1]^T \quad \in \mathcal{F}^{M_i} \quad (4.104b)$$

$$Q_{M_i} = \begin{bmatrix} q_0 \\ \vec{q} \end{bmatrix} = \begin{bmatrix} 1 + \hat{T}_i \cdot \hat{T}(\Omega_i) \\ -\hat{T}_i \times \hat{T}(\Omega_i) \end{bmatrix} \quad (4.104c)$$

Where Eq:4.104c is an extension of the inherent quaternion definition which rotates a vector around a single Euler axis, Eq:3.21b, when applied to unit vectors. That quaternion can indeed be used to solve for relative pitch, roll and yaw Euler angles (Appendix:A.3). The difficulty is that Eq:4.104c solves for the most direct path rotation from one vector to another and, in most cases, a sequenced Z-Y-X rotation is by no means the shortest possible path.

<sup>15</sup>Using the quaternion analogue of Eq:2.9a

The associated  $[\phi, \theta, \psi]^T$  solutions to Eq:A.15 are then of no consequence in trying to solve for sequence of rotation angles<sup>16</sup>  $[\lambda_i, \alpha_i, \sigma_i]^T$ . Furthermore, when considering a sequenced Z-Y-X quaternion, no further insight can be extracted without applying cumbersome trigonometry inversions;

$$Q_b = \begin{bmatrix} \cos \frac{\psi}{2} \\ 0 \\ 0 \\ \sin \frac{\psi}{2} \end{bmatrix} \otimes \begin{bmatrix} \cos \frac{\theta}{2} \\ 0 \\ \sin \frac{\theta}{2} \\ 0 \end{bmatrix} \otimes \begin{bmatrix} \cos \frac{\phi}{2} \\ \sin \frac{\phi}{2} \\ 0 \\ 0 \end{bmatrix} \quad (4.105a)$$

$$= \begin{bmatrix} \cos \frac{\psi}{2} \cos \frac{\theta}{2} \cos \frac{\phi}{2} + \sin \frac{\psi}{2} \sin \frac{\theta}{2} \sin \frac{\phi}{2} \\ \cos \frac{\psi}{2} \cos \frac{\theta}{2} \sin \frac{\phi}{2} - \sin \frac{\psi}{2} \sin \frac{\theta}{2} \cos \phi 2 \\ \cos \frac{\psi}{2} \sin \frac{\theta}{2} \cos \phi 2 + \sin \frac{\psi}{2} \cos \frac{\theta}{2} \sin \frac{\phi}{2} \\ \sin \frac{\psi}{2} \cos \frac{\theta}{2} \cos \frac{\phi}{2} - \cos \frac{\psi}{2} \sin \frac{\theta}{2} \sin \frac{\phi}{2} \end{bmatrix} = \begin{bmatrix} q_0 \\ q_x \\ q_y \\ q_z \end{bmatrix} = \begin{bmatrix} q_0 \\ \vec{q} \end{bmatrix} \quad (4.105b)$$

$$\Rightarrow \vec{T}_i = \begin{bmatrix} \cos \frac{\psi}{2} \cos \frac{\theta}{2} \cos \frac{\phi}{2} + \sin \frac{\psi}{2} \sin \frac{\theta}{2} \sin \frac{\phi}{2} \\ \cos \frac{\psi}{2} \cos \frac{\theta}{2} \sin \frac{\phi}{2} - \sin \frac{\psi}{2} \sin \frac{\theta}{2} \cos \phi 2 \\ \cos \frac{\psi}{2} \sin \frac{\theta}{2} \cos \phi 2 + \sin \frac{\psi}{2} \cos \frac{\theta}{2} \sin \frac{\phi}{2} \\ \sin \frac{\psi}{2} \cos \frac{\theta}{2} \cos \frac{\phi}{2} - \cos \frac{\psi}{2} \sin \frac{\theta}{2} \sin \frac{\phi}{2} \end{bmatrix} \otimes \vec{T}(\Omega_i) \otimes \begin{bmatrix} s \frac{\psi}{2} s \frac{\theta}{2} s \frac{\phi}{2} + c \frac{\psi}{2} c \frac{\theta}{2} c \frac{\phi}{2} \\ s \frac{\psi}{2} s \frac{\theta}{2} c \frac{\phi}{2} - c \frac{\psi}{2} c \frac{\theta}{2} s \frac{\phi}{2} \\ -c \frac{\psi}{2} s \frac{\theta}{2} c \frac{\phi}{2} - s \frac{\psi}{2} c \frac{\theta}{2} s \frac{\phi}{2} \\ c \frac{\psi}{2} s \frac{\theta}{2} s \frac{\phi}{2} - s \frac{\psi}{2} c \frac{\theta}{2} c \frac{\phi}{2} \end{bmatrix} \quad (4.105c)$$

Instead, returning to rotation matrices and reiterating that  $[\phi, \theta, \psi]^T \Rightarrow [\lambda_i, \alpha_i, \sigma_i]^T$ , then:

$$\vec{T}_i = \begin{bmatrix} c\sigma & -s\sigma & 0 \\ s\sigma & c\sigma & 0 \\ 0 & 0 & 1 \end{bmatrix} \begin{bmatrix} c\alpha & 0 & s\alpha \\ 0 & 1 & 0 \\ -s\alpha & 0 & c\alpha \end{bmatrix} \begin{bmatrix} 1 & 0 & 0 \\ 0 & c\lambda & -s\lambda \\ 0 & s\lambda & c\lambda \end{bmatrix} \quad (4.106a)$$

$$\Rightarrow \vec{T}_i = \begin{bmatrix} c\sigma c\alpha & c\sigma s\alpha \lambda - s\sigma c\lambda & c\sigma s\alpha \lambda + s\sigma s\lambda \\ s\sigma c\alpha & s\sigma s\alpha \lambda + c\sigma c\lambda & s\sigma s\alpha \lambda - c\sigma s\lambda \\ -s\alpha & c\alpha s\lambda & c\alpha c\lambda \end{bmatrix} \begin{bmatrix} 0 \\ 0 \\ T(\Omega_i) \end{bmatrix} \quad (4.106b)$$

$$\Rightarrow \begin{bmatrix} T_x \\ T_y \\ T_z \end{bmatrix} = \begin{bmatrix} s\sigma s\lambda + c\sigma s\alpha \lambda \\ s\sigma s\alpha \lambda - c\sigma s\alpha \\ c\alpha c\lambda \end{bmatrix} T(\Omega_i) \quad (4.106c)$$

When  $\sigma$  is an orthogonal multiple which rotates the vector about the  $\hat{Z}_b$  axis, then Eq:4.106c simplifies even further:

$$\begin{bmatrix} T_x \\ T_y \\ T_z \end{bmatrix} = \left[ \begin{bmatrix} s\alpha c\lambda \\ -s\alpha \\ c\alpha c\lambda \end{bmatrix}, \begin{bmatrix} s\lambda \\ s\alpha c\lambda \\ c\alpha c\lambda \end{bmatrix}, \begin{bmatrix} -s\alpha c\lambda \\ s\alpha \\ c\alpha c\lambda \end{bmatrix}, \begin{bmatrix} -s\lambda \\ -s\alpha c\lambda \\ c\alpha c\lambda \end{bmatrix} \right] T(\Omega_i) \quad \text{for } i \in [1, 2, 3, 4] \quad (4.107)$$

Then it becomes a simple case of inverse trigonometry to solve for both  $\lambda_i$  and  $\alpha_i$  respectively, for the case of  $i = 1$ , the following holds true. Using  $T(\Omega_i) = \|T_i\|$  and  $\arctan 2(x, y)$  for both solutions to get full quadrature results:

$$\alpha = -\arctan 2(T_x, T_z \|T_i\|) \quad (4.108a)$$

$$\lambda = \arctan 2(T_x^2, \|T_i\| \sqrt{\|T_i\|^2 - T_x^2}) \quad (4.108b)$$

Therefore, the secondary component of the control allocation block,  $R^\dagger(\mathbf{x}, \vec{T}_i, t)$  from Fig:4.2 is then:

$$\begin{bmatrix} \Omega_i \\ \lambda_i \\ \alpha_i \end{bmatrix} = R^\dagger(\mathbf{x}, \vec{T}_i, t) = \begin{bmatrix} (\sqrt{T_x^2 + T_y^2 + T_z^2} / C_T(J)\rho D^4)^{\frac{1}{2}} \\ \arctan 2(T_x^2, \|T_i\| \sqrt{\|T_i\|^2 - T_x^2}) \\ -\arctan 2(T_x, T_z \|T_i\|) \end{bmatrix} \quad (4.109)$$

Further simplifications could be from the definitions of each element included in Eq:4.109, but it would just be superfluous. At this stage the only remaining undefined component of the entire control block is the abstracted allocation algorithms,  $B^\dagger(\mathbf{x}, \vec{\nu}_d, t)$ , which are now addressed...

<sup>16</sup> $\sigma_i$  is already known to be an orthogonal multiplicate...

**4.6.1 Pseudo Inverse Allocator****4.6.2 Weighted Pseudo Inverse Allocator****4.6.3 Priority Norm Inverse Allocator****4.6.4 Non-linear Plant Control Allocation****4.6.5 Online Optimized Secondary Goal Allocator**

# **Chapter 5**

## **Simulations & Results**

### **5.1 Controller Tuning**

#### **5.1.1 Partical Swarm Based Optimization**

#### **5.1.2 Performance Metric**

#### **5.1.3 Global & Local Minima**

#### **5.1.4 Fmincon Differences**

### **5.2 Simulation Block**

### **5.3 State Estimation**

### **5.4 Optimized Controller Comparisons**

#### **5.4.1 Allocator Performance**

#### **5.4.2 Attitude Control Results**

#### **5.4.3 Autopilot Outcome**

## Chapter 6

# Prototype Flight Results

# Chapter 7

## Conclusion

- Lagrange dynamics for multibody system could have produced a more concise model etc . . .
- Particle multibody dynamics with interactions could provide a more verbose simulation environment rather than the very newtonian simulation loop constructed
- Implicit equation dynamics in simulation may improve optimization loops in PSO algorithm

# Appendix A

## Expanded Equations

### A.1 Standard Quadrotor Dynamics

Following the 6-DOF fundamental derivations in Section:3.1.1, the common reductions typically applied for a generic "+" configuration quadrotor are now presented. Reiterating those four differential equations, Eq:3.9, which describe a rigid body's motion (using rotation matrices and not quaternions):

$$\dot{\vec{\mathcal{E}}} = \mathbb{R}_b^I(-\eta)\vec{v}_b \quad \in \mathcal{F}^I \quad (\text{A.1a})$$

$$\dot{\vec{v}}_b = m^{-1} [ -\vec{\omega}_b \times m\vec{v} + m\mathbb{R}_I^b(-\eta)\vec{G}_I + \vec{F}_{net} ] \quad \in \mathcal{F}^b \quad (\text{A.1b})$$

$$\dot{\vec{\eta}} = \Psi(\eta)\vec{\omega}_b \quad \in \mathcal{F}^{v2}, \mathcal{F}^{v1}, \mathcal{F}^I \quad (\text{A.1c})$$

$$\dot{\vec{\omega}}_b = \mathbb{I}_b^{-1} [ -\vec{\omega}_b \times \mathbb{I}_b \vec{\omega}_b + \vec{\tau}_{net} ] \quad \in \mathcal{F}^b \quad (\text{A.1d})$$

With the Euler matrix,  $\Psi(\eta)$ , defined in Eq:2.5e. The net lift force produced by motors  $i = [1 : 4]$ , bound perpendicularly to the  $\hat{Z}_b$  axis, is given by:

$$\vec{T} = \sum_{i=1}^4 F_i \hat{k} \quad \in \mathcal{F}^b \quad (\text{A.2a})$$

The simplified relationship between the thrust force  $\vec{F}_i$  and the propellers rotational speed  $\Omega_i$  is approximately quadratic:

$$\vec{F}_i = k_1 \Omega_i^2 \quad (\text{A.2b})$$

Similarly the aerodynamic torque opposing each rotating propeller is:

$$Q = k_2 \Omega_i^2 \quad (\text{A.3})$$

Coefficients  $k_1$  &  $k_2$  are typically determined from physical test results. The control pitch and roll torques,  $\tau_\phi$  &  $\tau_\theta$  respectively, are generated by opposing differential lift forces. Lastly the yaw torque is generated as a net response to the rotational aerodynamic propeller torques. The control torque inputs are then defined as:

$$\tau_\phi = \vec{L}_{arm}(\vec{F}_1 - \vec{F}_3) \quad (\text{A.4a})$$

$$\tau_\theta = \vec{L}_{arm}(\vec{F}_2 - \vec{F}_4) \quad (\text{A.4b})$$

$$\tau_\psi = \sum_{i=1}^4 (-1)^i k_2 \Omega_i \quad (\text{A.4c})$$

Then expanding the linear translational position and attitude differentials, Eq:A.1b & Eq:A.1d, to their component forms:

$$\begin{pmatrix} \dot{u} \\ \dot{v} \\ \dot{w} \end{pmatrix} = \begin{pmatrix} rv - qw \\ pw - ru \\ qu - pv \end{pmatrix} + \begin{pmatrix} -g\sin(\theta) \\ g\cos(\theta)\sin(\phi) \\ g\cos(\theta)\cos(\phi) \end{pmatrix} + \frac{1}{m} \begin{pmatrix} 0 \\ 0 \\ T \end{pmatrix} \in \mathcal{F}^b \quad (\text{A.5a})$$

$$\begin{pmatrix} \dot{p} \\ \dot{q} \\ \dot{r} \end{pmatrix} = \begin{pmatrix} \frac{\mathbb{I}_y - \mathbb{I}_z}{\mathbb{I}_x} qr \\ \frac{\mathbb{I}_z - \mathbb{I}_x}{\mathbb{I}_y} pr \\ \frac{\mathbb{I}_x - \mathbb{I}_y}{\mathbb{I}_z} pq \end{pmatrix} + \mathbb{I}_b^{-1} \begin{pmatrix} \tau_\phi \\ \tau_\theta \\ \tau_\psi \end{pmatrix} \in \mathcal{F}^b \quad (\text{A.5b})$$

Considering the size of the average angular velocity  $\omega_b \approx \vec{0}$ , the gyroscopic and Coriolis effects on the body (namely both cross product terms) are depreciated and can be regarded as negligible. Assuming too that the body has a (*roughly*) diagonal inertial matrix. Then:

$$\begin{pmatrix} rv - qw \\ pw - ru \\ qu - pv \end{pmatrix} \approx \vec{0} \quad \text{and} \quad \begin{pmatrix} \frac{\mathbb{I}_y - \mathbb{I}_z}{\mathbb{I}_x} qr \\ \frac{\mathbb{I}_z - \mathbb{I}_x}{\mathbb{I}_y} pr \\ \frac{\mathbb{I}_x - \mathbb{I}_y}{\mathbb{I}_z} pq \end{pmatrix} \approx \vec{0} \quad (\text{A.6})$$

As a result, equations from Eq:A.5 then simplify to:

$$\begin{pmatrix} \dot{u} \\ \dot{v} \\ \dot{w} \end{pmatrix} = \begin{pmatrix} -g\sin(\theta) \\ g\cos(\theta)\sin(\phi) \\ g\cos(\theta)\cos(\phi) \end{pmatrix} + \frac{1}{m} \begin{pmatrix} 0 \\ 0 \\ T \end{pmatrix} \quad \text{and} \quad \begin{pmatrix} \dot{p} \\ \dot{q} \\ \dot{r} \end{pmatrix} = \begin{pmatrix} \frac{1}{\mathbb{I}_x} \tau_\phi \\ \frac{1}{\mathbb{I}_y} \tau_\theta \\ \frac{1}{\mathbb{I}_z} \tau_\psi \end{pmatrix} \quad (\text{A.7})$$

Similarly, around the origin and at hovering conditions,  $\Psi(\eta) \approx \vec{1}$  for  $\eta \approx \vec{0}$  and so from Eq:A.1c, then  $\dot{\eta} \approx \omega_b$ . Or in component form:

$$\begin{pmatrix} \dot{p} \\ \dot{q} \\ \dot{r} \end{pmatrix} \approx \begin{pmatrix} \ddot{\phi} \\ \ddot{\theta} \\ \ddot{\psi} \end{pmatrix} \quad (\text{A.8})$$

As such, the differential equations Eq:A.5 are then simplified to the following six SISO controllable plants:

$$\ddot{x} = (-\cos(\phi)\sin(\theta)\cos(\psi) - \sin(\phi)\sin(\psi)) \frac{1}{m} T \quad (\text{A.9a})$$

$$\ddot{y} = (-\cos(\phi)\sin(\theta)\sin(\psi) + \sin(\phi)\cos(\psi)) \frac{1}{m} T \quad (\text{A.9b})$$

$$\ddot{z} = g - (\cos(\phi)\cos(\theta)) \frac{1}{m} T \quad (\text{A.9c})$$

$$\ddot{\phi} = \frac{1}{\mathbb{I}_x} \tau_\phi \quad (\text{A.9d})$$

$$\ddot{\theta} = \frac{1}{\mathbb{I}_y} \tau_\theta \quad (\text{A.9e})$$

$$\ddot{\psi} = \frac{1}{\mathbb{I}_z} \tau_\psi \quad (\text{A.9f})$$

Typically, the simplified states in Eq:A.9 are abstracted to what is termed as an "augmented pilot control system". As such the controllable inputs are abstracted to  $T$ ,  $\dot{\phi}$ ,  $\dot{\theta}$ ,  $\dot{\psi}$ . Wherein the pilot can dictate the attitude and net heave thrust of the quadrotor, mostly with various flavours of PID control.

## A.2 Blade-Element Momentum Expansion

Expanding on the Blade-Element Momentum equations from Eq:3.52 & Eq:3.53a. Reiterating the equations, they are:

$$dT = \rho 4\pi r v_\infty (1+a) a dr \quad (\text{A.10a})$$

$$dT = \frac{1}{2} a_L b c \rho (\Omega r)^2 \left( \theta - \frac{v_\infty + v_i}{\Omega r} \right) dr \quad (\text{A.10b})$$

Equating the two and defining an inflow ratio term  $\lambda = \frac{v_\infty + v_i}{\Omega r} = \frac{v_\infty (1+a)}{\Omega r}$  yields the following quadratic equation:

$$\lambda^2 + \left( \frac{\sigma a_L}{8} + \lambda_c \right) \lambda - \frac{\sigma a_L}{8} \theta \frac{r}{R} = 0 \quad (\text{A.11})$$

Where  $\lambda_c$  is the nominal free-stream inflow ratio when  $v_i = 0$ . Another term,  $\sigma$ , is defined as the propeller solidity and is given by:

$$\sigma = \frac{bc}{\pi R} \quad (\text{A.12})$$

Then, solving Eq:A.11 for  $\lambda$ :

$$\lambda = \sqrt{\left( \frac{\sigma a_L}{16} - \frac{\lambda_c}{2} \right)^2 + \frac{\sigma a_L}{8} \theta \frac{r}{R}} - \left( \frac{\sigma a_L}{16} - \frac{\lambda_c}{2} \right) \quad (\text{A.13})$$

So then the inflow ratio can be solved as a function of the propeller element's aerofoil profile and its static inflow factor. In static conditions, the inflow factor is:

$$\lambda = \frac{v_i}{\Omega r} = \sqrt{\frac{C_{T0}}{2}} \quad (\text{A.14})$$

Then substituting  $\lambda$  back into Eq:3.53a and solving the integral produces an instantaneous thrust value. The difficulty of solving the blade-element momentum integrals is knowing the exact chord profile and local angle of attack.

## A.3 Euler-Angles from Quaternions

Then, noting that the transformation from the body frame to each motor frame follows the Z-Y-X sequence, and using an inversion solution adapted from [102], where the transformation to quaternions is based on Shoemake's [100] definition. Each quaternion can be constructed from sequenced Euler angles, as in Eq:3.27. Then, solving for each euler angle using simultaneous solutions and inverse trigonometry:

$$\begin{bmatrix} \phi \\ \theta \\ \psi \end{bmatrix} = \begin{bmatrix} \arctan2(2(q_0 q_x + q_y q_z), 1 - 2(q_x^2 + q_y^2)) \\ \arcsin(2(q_0 q_y - q_x q_z)) \\ \arctan2(2(q_0 q_z + q_x q_y), 1 - 2(q_y^2 + q_z^2)) \end{bmatrix} \quad (\text{A.15})$$

Where  $\arctan2(x, y)$  is the four-quadrant tangent inverse [31], producing the principle argument of the complex operands;

$$\arctan2(x, y) = PR \arg(x + y\hat{i}) = Arg(x + y\hat{i}) \quad (\text{A.16})$$

## Appendix B

# Design Bill of Materials

### B.1 Parts List

Part Name	No. Used	Unit Weight[g]
Electronics		
SPRacing F3 Deluxe Flight Controller	1	8
OrangeRx 615X 2.4 GHz 6CH Receiver	1	9.8
Signal Converter SBUS-PPM-PWM	1	5.0
STLink-V2 Debugger	1	3
RotorStar Super Mini S-BEC 10A	1	30
128x96" OLED Display	1	7
XBee-Pro S1	2	4
HobbyWing XRotor 20A Opto ESC	4	15
OrangeRX RPM Sensor	4	2
HobbyKing Multi-Rotor Power Distribution Board	1	49
Motors		
Corona DS-339MG	8	32
Cobra 2208 2000KV Brushless DC	4	44.2
Frame Components		
APM Flight Controller Damping Platform	1	7
HobbyKing SK450 Replacement Arm (2 pcs)	2	51
SK450 Extended Landing Skid	1	23.25
Alloy Servo Arm (FUTABA)	8	4
10X18X6 Radial Ball Bearing	8	5
80g Damping Ball	32	≈ 0
Plastic Retainers for Damping Balls	32	≈ 0
3/5mm Aluminum Prop Adapter	4	≈ 1
6x4.5 Gemfam 3-Blade Propeller	4	6
M3 6mm Hex Nylon Spacer	8	≈ 0
M3 16mm Hex Nylon Spacer	32	≈ 0
M3 25mm Nylon Screw	128	≈ 0.08
M2.5x10mm Socket Head Cap Screw	36	≈ 0.2
M2.5x25mm Socket Head Cap Screw	20	≈ 0.6
M2.5 A-Lok Nut	16	≈ 0

Table B.1: Parts List

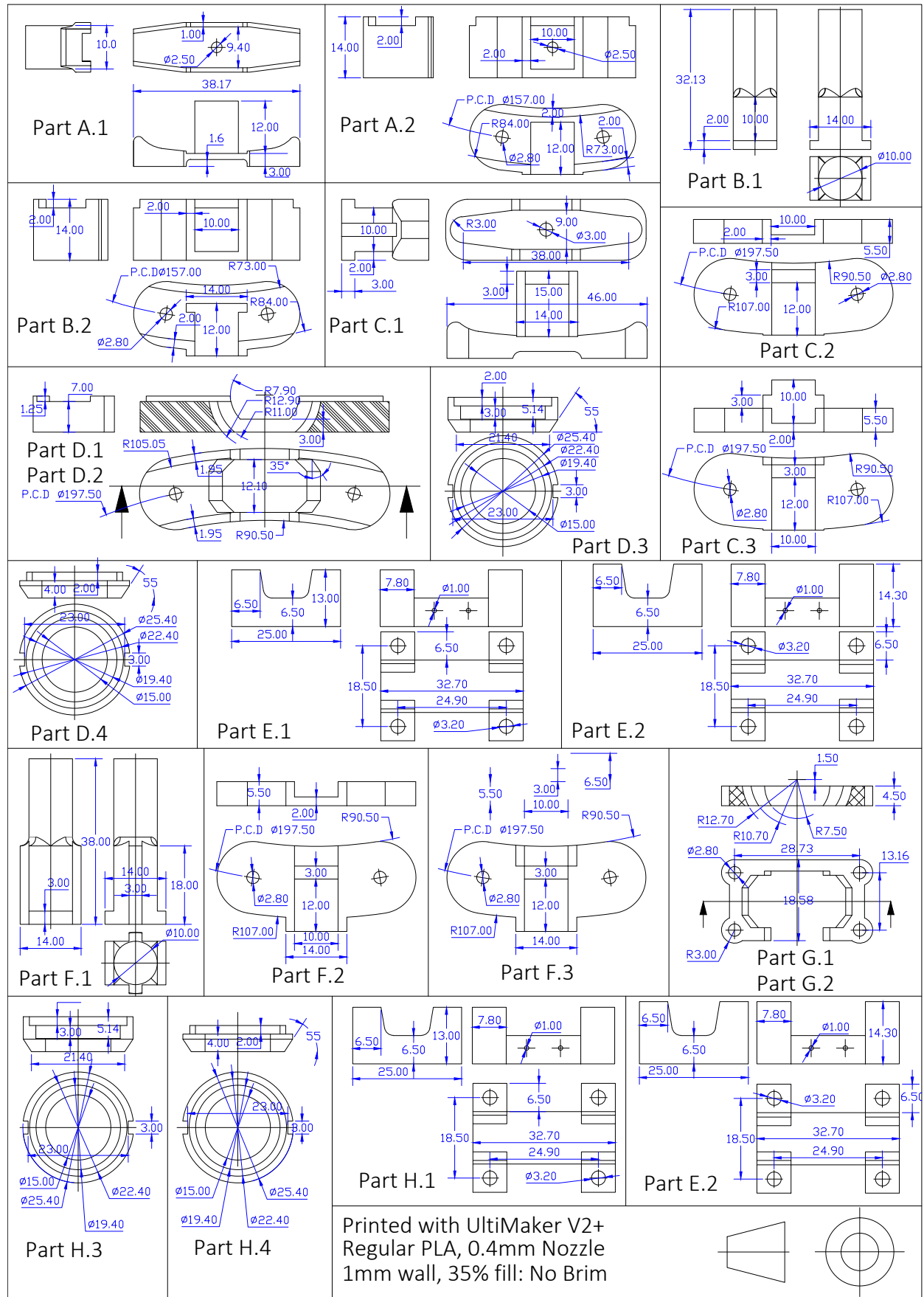
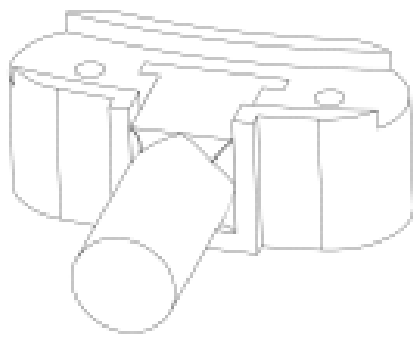
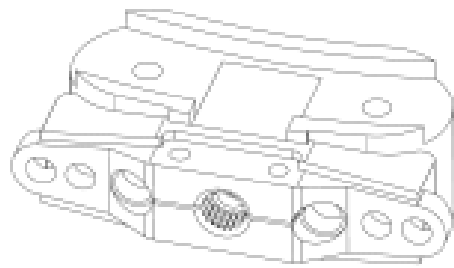


Table B.2: 3D Printed Parts

## Bracket Assemblies 2



**Figure B.1:** Bearing Bracket Inner Ring Assembly  
Parts: A.1, A.2



**Figure B.2:** Servo Bracket Inner Ring Assembly  
Parts: B.1, B.2, M3 Servo Horn

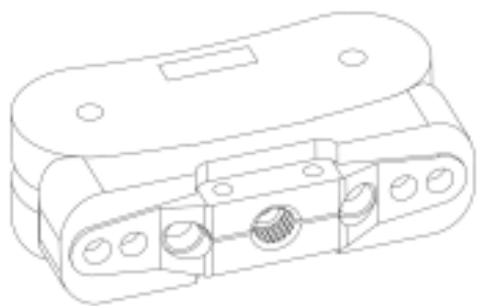


**Figure B.3:** Servo Bracket Middle Ring Assembly  
Parts: C.1, C.2, C.3, M3 Servo Horn



**Figure B.4:** Bearing Holder Middle Ring Assembly  
Parts: D.1, D.2, D.3, D.4, 18-10 Bearing

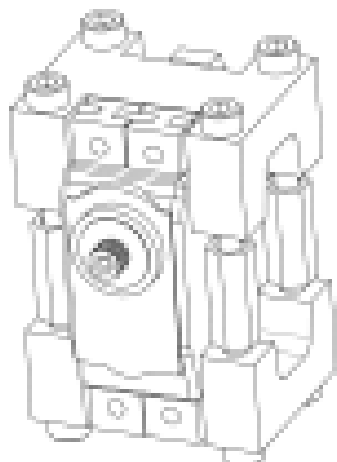


**Figure B.5:** Servo Mount Middle Ring Assembly  
Parts: E.1, E.2, Corona Servo & Fasteners



**Figure B.6:** Bearing Shaft Middle Ring Assembly  
Parts: F.1, F.2, F.3

**Table B.3:** Inner & Middle Ring Assemblies

## Bracket Assemblies 2

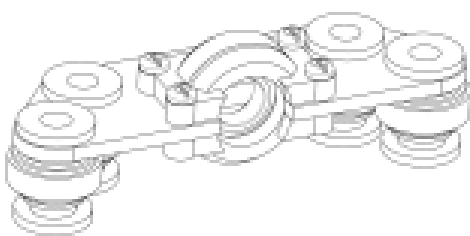


**Figure B.7:** Bearing Holder Damping Assembly  
Parts: G.1, G.2, G.3, G.4, 18-10 Bearing, 80g Damping Balls, Bearing Holder Damping Bracket

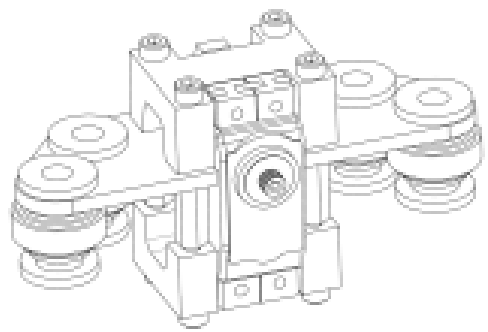


**Figure B.8:** Servo Mount Damping Assembly  
Parts: H.1, H.2, Corona Servo & Fasteners, 80g Damping Balls, Servo Mount Damping Bracket

**Table B.4:** Damping Assemblies

## Laser Cut Brackets

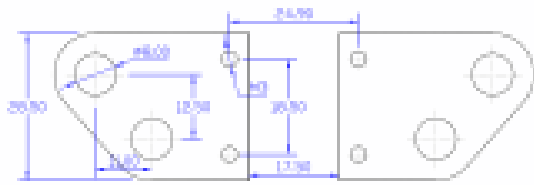


**Figure B.9:** Servo Mount Damping Bracket

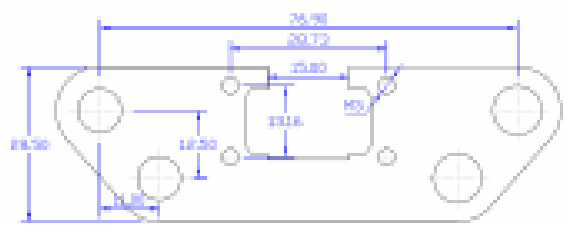


**Figure B.10:** Bearing Holder Damping Bracket

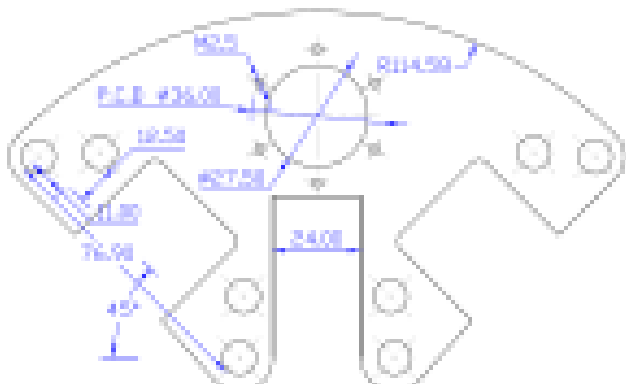


**Figure B.11:** Arm Mount Damping Bracket

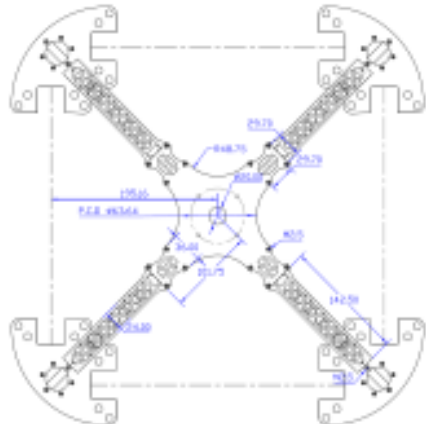


**Figure B.12:** Frame Brackets

**Table B.5:** Laser Cut Damping Brackets

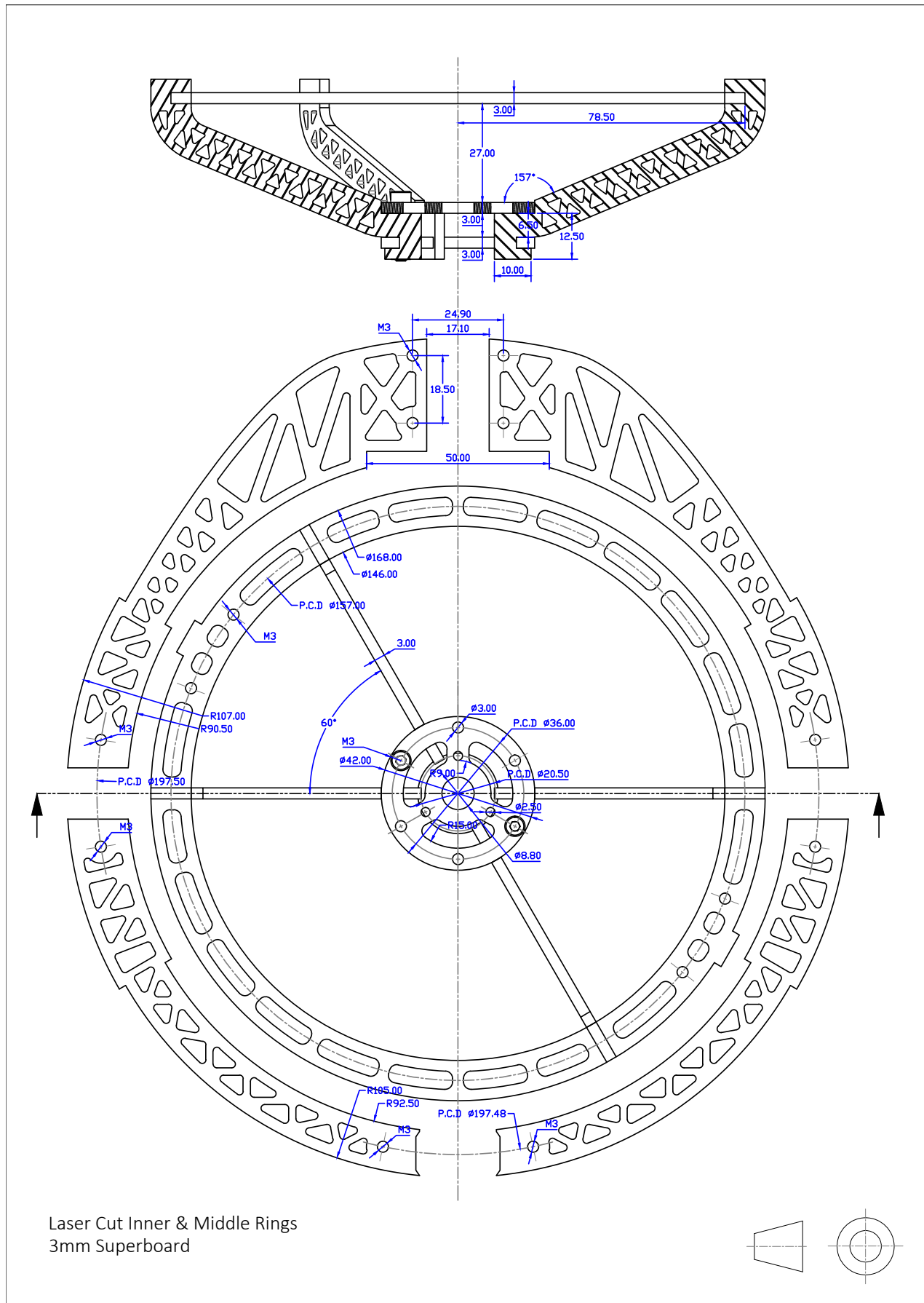


Table B.6: Laser Cut Parts

## B.2 F3 Deluxe Schematic Diagram

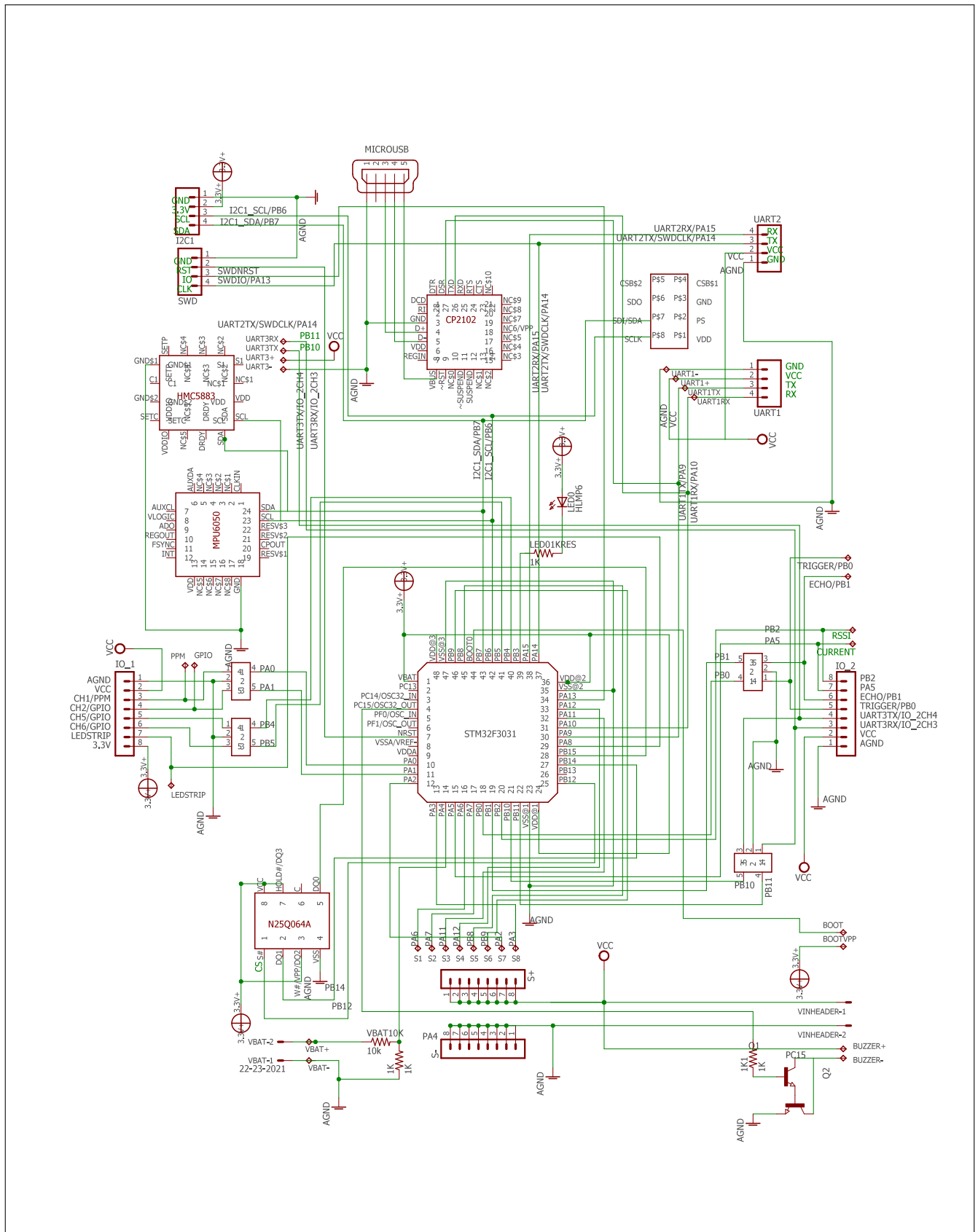
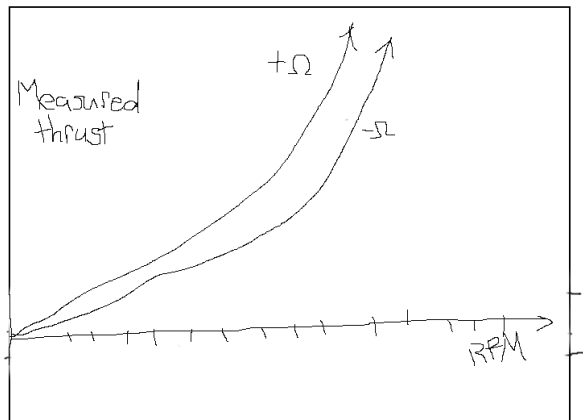


Figure B.13: F3 Deluxe Flight Controller Hardware Schematic

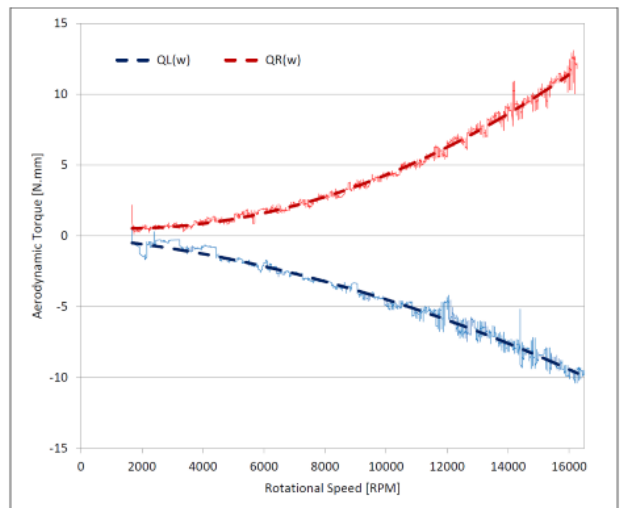
## Appendix C

# System ID Test Data

### C.1 Thrust and Torque Test Data



(a) Thrust tests



(b) Torque tests

**Figure C.1:** Clockwise and counterclockwise rotation tests

## C.2 Cobra CM2208-200KV Thrust Data

Cobra CM-2208/20 Motor Propeller Data										
Magnets 14-Pole	Motor Wind 20-Turn Delta	Motor Kv 2000 RPM/Volt		No-Load Current $I_o = 0.77$ Amps @ 10v	Motor Resistance $R_m = 0.076$ Ohms		I Max 20 Amps	P Max (3S) 220 W		
Stator 12-Slot	Outside Diameter 27.7 mm, 1.091 in.	Body Length 24.0 mm, 0.945 in.		Total Shaft Length 45.2 mm, 1.780 in.	Shaft Diameter 3.17 mm, 0.125 in.		Motor Weight 44.2 gm, 1.56 oz			
Test Data From Sample Motor		Input	6.0 V	8.0 V	10.0V	12.0V	Measured Kv value	Measured Rm Value		
		$I_o$ Value	0.59 A	0.67 A	0.77 A	0.87 A	1988 RPM/Volt @ 10v	0.076 Ohms		
Prop Manf.	Prop Size	Li-Po Cells	Input Voltage	Motor Amps	Input Watts	Prop RPM	Pitch Speed in MPH	Thrust Grams	Thrust Ounces	Thrust Eff. Grams/W
APC	5.25x4.75-E	3	11.1	13.34	148.1	17,507	78.7	451	15.91	3.05
APC	5.5x4.5-E	3	11.1	13.67	151.7	17,388	74.1	456	16.08	3.01
APC	6x4-E	3	11.1	14.87	165.1	17,003	64.4	630	22.22	3.82
APC	7x4-SF	3	11.1	21.82	242.2	13,985	53.0	840	29.63	3.47
APC	7x5-E	3	11.1	24.02	266.6	13,272	62.8	797	28.11	2.99
FC	5x4.5	3	11.1	8.66	96.1	19,061	81.2	428	15.10	4.45
FC	5x4.5x3	3	11.1	12.38	137.4	17,825	76.0	534	18.84	3.89
FC	6x4.5	3	11.1	15.47	171.7	16,792	71.6	721	25.43	4.20
GemFan	5x3	3	11.1	6.67	74.0	19,801	56.3	374	13.19	5.05
HQ	5x4	3	11.1	7.13	79.1	18,182	68.9	373	13.16	4.71
HQ	5x4x3	3	11.1	9.25	102.7	17,401	65.9	449	15.84	4.37
HQ	5x4.5-BN	3	11.1	11.17	124.0	16,902	72.0	487	17.18	3.93
HQ	6x3	3	11.1	7.34	81.5	18,128	51.5	419	14.78	5.14
HQ	6x4.5	3	11.1	13.53	150.2	16,206	69.1	645	22.75	4.29
HQ	6x4.5x3	3	11.1	17.60	195.4	15,137	64.5	762	26.88	3.90
HQ	7x4	3	11.1	20.71	229.9	14,250	54.0	850	29.98	3.70
HQ	7x4.5	3	11.1	20.31	225.4	14,351	61.2	865	30.51	3.84
Prop Manf.	Prop Size	Li-Po Cells	Input Voltage	Motor Amps	Input Watts	Prop RPM	Pitch Speed in MPH	Thrust Grams	Thrust Ounces	Thrust Eff. Grams/W
APC	5.25x4.75-E	4	14.8	17.29	255.9	20,560	92.5	603	21.27	2.36
APC	5.5x4.5-E	4	14.8	17.87	264.5	20,436	87.1	635	22.40	2.40
APC	6x4-E	4	14.8	20.15	298.2	19,829	75.1	837	29.52	2.81
FC	5x4.5	4	14.8	10.89	161.2	22,511	95.9	588	20.74	3.65
FC	5x4.5x3	4	14.8	16.43	243.2	20,828	88.8	718	25.33	2.95
FC	6x4.5	4	14.8	20.09	297.3	19,809	84.4	998	35.20	3.36
HQ	4x4.5-BN	4	14.8	10.45	154.7	22,661	96.6	477	16.83	3.08
HQ	5x3	4	14.8	6.88	101.8	23,580	67.0	442	15.59	4.34
HQ	5x4	4	14.8	10.22	151.3	22,739	86.1	589	20.78	3.89
HQ	5x4x3	4	14.8	13.26	196.2	21,763	82.4	710	25.04	3.62
HQ	5x4.5-BN	4	14.8	16.10	238.3	20,899	89.1	744	26.24	3.12
HQ	6x3	4	14.8	11.06	163.7	22,512	64.0	679	23.95	4.15
HQ	6x4.5	4	14.8	19.62	290.4	19,948	85.0	982	34.64	3.38

Figure C.2: Official Test Results for Cobra Motors

## Appendix D

### Inertias

$$\mathbb{I}_{prop} \quad (\text{D.1a})$$

$$\mathbb{I}_{inner} \quad (\text{D.1b})$$

$$\mathbb{I}_{middle} \quad (\text{D.1c})$$

$$\mathbb{I}_{body} \quad (\text{D.1d})$$

# Bibliography

- [1] Parrot AG. Parrot ar drone 2.0. <https://www.parrot.com/fr/drones/parrot-ardrone-20-elite-edition#technical>, 2016. [Accessed:2017-01-16].
- [2] Yazan Al-Rihani. *Development of a dual axis tilt rotorcraft uav: Design, prototyping and control.*, volume 1. Cranfield University: School of Engineering, 2012.
- [3] N. Amiri, A. Ramirez-Serrano, and Davies R. Modelling of opposed lateral and longitudinal tilting dual-fan unmanned aerial vehicle. *International Federation of Automatic Control*, pages 2054–2059, September 2011.
- [4] APMCopter. Arducopter main page. Website: <http://www.arducopter.co.uk/>, 6 2016. Arducopter (APM) Official Website.
- [5] E. Balasubramanian and R. Vasantharaj. Dynamic modelling and control of quadrotor. *International Journal of Engineering and Technology*, pages 63–39, February 2013.
- [6] P. Baldi, B. Mogens, P. Castaldi, N Mimmo, and S. Simani. Adatpive ftc based on control allocation and fault accomodation for satellite reaction wheels. In *Conference on Control and Fault-Tolerant Systems*, volume 3, pages 1–6, 9 2016.
- [7] M. Bangura and R. Mahony. Non-linear dynamic modelling for high performance control of a quadrotor. In *Australasian Conference on Robotics and Automation, Victoria University of Wellington*. Victoria University of Wellington, 12 2012. Published in Conference Proceedings.
- [8] M. Bangura, M Melega, R. Naldi, and R. Mahony. Aerodynamics of rotorblades for quadrotors. Report, Colaboration: Australian National University & University of Bologna, 1 2016. ArXiv Published:<https://arxiv.org/abs/1601.00733>.
- [9] Mohd Ariffanan Basri, Abdul R. Husain, and Kumeresan A. Danapalasingam. Intelligent adaptive backstepping control for mimo uncertain non-linear quadrotor helicopter systems. *Institute of Measurement Control Transactions*, pages 1–17, 2014.
- [10] BetaFlight. Betaflight fc4 repo. Forked from the CleanFlight repo,<https://github.com/betaflight/betaflight>, 2016. [Accessed:2016-9-17].
- [11] BLHeli. Blheli master branch (silabs). <https://github.com/bitdump/BLHeli/tree/master/SiLabs>, 2016. [Accessed:2016-11-05].
- [12] Charles Blouin and Eric Lanteigne. Pitch control on an oblique active tilting bi-rotor. *International Conference on Unmanned Aircraft Systems*, pages 791–799, May 2014.
- [13] R. Bodrany, W. Steyn, and M. Crawford. In-orbit estimation of the inertia matrix and thruster parameters of uosat-12. In *Conference on Small Satellites*, volume 14, pages 1–11. American Institute of Aeronautics and Astronautics, 2000.
- [14] Hossein Bolandi, Mohammed Rezaei, Rezo Mohsenipour, Hossein Nemati, and Seed Majid Smailzadeh. Attitude control of a quadrotor with optimized pid. *Intelligent Control and Automation*, pages 335–342, August 2013.

- [15] S. Bouabdallah and R. Siegwart. Full control of a quadrotor. *IEEE International Conference on Intelligent Robots and Systems*, pages 153–158, 11 2007. Written for Autonomous Systems Lab at Swiss Federal Institute of Technology.
- [16] Samir Bouabdallah, Andre Noth, and Roland Siegward. Pid vs lq control techniques applies to an indoor micro quadrotor. *IEEE International Conference on Intelligent Robots and Systems*, pages 2451–2456, 9 2004.
- [17] A.R.S Bramwell, D. Balmford, and G. Done. *Bramwell's Helicopter Dynamics*, chapter 1-3, pages 1–144. Elsevier Ltd, 2 edition, 1999.
- [18] J. Brandt, R. Deters, G. Ananda, and M. Selig. Uiuc propeller data site. University of Illinois Urbana-Champaign; Department of Aerospace Engineering: <http://www.steadidrone.com/>, 2008. [Accessed:2016-13-12].
- [19] J. Brandt and M. Selig. Propeller performance data at low reynolds numbers. *American Institute of Aeronautics and Astronautics Sciences Meeting, 49th*, pages 1–18, January 2011.
- [20] D. Brescianini, M. Hehn, and R D'Andrea. Nonlinear quadrocopter attitude control. Technical report, Institute for Dynamic Systems and Control, ETH Zurich, 10 2013.
- [21] Jian Chen, Aman Behal, and Darren M. Dawson. Adaptive output feedback control for a class of mimo nonlinear systems. In *Proceedings of the American Control Conference*, pages 5300–5306, Minneapolis, Minnesota, US, 6 2006. American Control Conference.
- [22] Arindam B. Chowdhury, Anil Kulhare, and Guarav Raina. A generalized control method for tilt-rotor uav stabilization. *IEEE International Conference on Cyber Technology in Automation, Control and Intelligent Systems*, pages 309–314, May 2012.
- [23] CleanFlight. Cleanflight repo. <https://github.com/cleanflight/cleanflight>, 2016. [Accessed:2016-11-13].
- [24] Dominic Clifton. Spracing f3 deluxe flight controller. <http://seriouslypro.com/spracingf3>, 2015. [Accessed:2016-10-04].
- [25] R.F. de Olivera, F.T. de Salvi, and E.M. Belo. Dynamic modelling, simulation and control of an autonomous quadcopter aircraft. *International Congress of Mechanical Engineering*, pages 1–9, November 2009.
- [26] Innov8tive Designs. Cobra cm2208/2000 motors. <http://innov8tivedesigns.com/cobra-cm-2208-20-motor-kv-2000>, 2016. [Accessed:2016-06-10].
- [27] Chen Diao, Bin Xian, Qiang Yin, Wei Zeng, Haotao Li, and Yungao Yang. A nonlinear adaptive control approach for quadrotor uavs. In *Asian Control Conference Proceedings*, volume 8, pages 223–228, Kaohsiung, Taiwan, 5 2011. Asian Control Conference.
- [28] DJI Drones. Dji inspire one. <http://www.dji.com/product/inspire-1>, 2016. [Accessed:2016-07-10].
- [29] DJI Drones. Dji phantom. <http://www.dji.com/products/phantom>, 2016. [Accessed:2016-06-12].
- [30] Honeywell Solid State Electronics. Hmc5833 magnetometer datasheet. Advanced Information Data Sheet, 10 2010. Available From:<https://strawberry-linux.com/pub/HMC5833L.pdf>.
- [31] Internation Organization for Standardization/International Electrotechnical Commission. Programming language c. Open PDF for Library:<http://www.open-std.org/jtc1/sc22wg14/www/docs/n1124.pdf>, 2005. Section 7.12.4.4:The atan2 functions, Page 219.

- [32] Emil Fresk and George Nikolakopoulos. Full quaternion based attitude control for a quadrotor. *European Control Conference*, pages 3864–3869, 6 2013.
- [33] Pau. S Gasco. *Development of a Dual Axis Tilt Rotorcraft UAV: Modelling, Simulation and Control*, volume 1. Cranfield University: School of Engineering, 2012.
- [34] J. Gertler. V-22 osprey tilt-rotor aircraft: Background and issues for congress. Report, Congressional Research Service, 3 2011.
- [35] HiSystems GmbH. Mikrokopter quadroxl. <http://www.mikrokopter.de/en/products/kits>, 2016. [Accessed:2016-06-13].
- [36] Basile Graf. Quaternions and dynamics. Publication for Mathematics - Dynamical Systems, 2 2007.
- [37] Gary R. Gress. Lift fans as gyroscopes for controlling compact vtol air vehicles: Overview and development status of oblique active tilting. In *American Helicopter Society Annual Forum*, volume 63, Virginia Beach, 5 2007. American Helicopter Society, American Helicopter Society Inc. Forum Proceedings.
- [38] Gary R. Gress. *Passive Stabilization of VTOL Aircraft Having Obliquely Tilting Propellers*. University of Calgary, Department of Mechanical Engineering, Calgary, Alberta, 2014.
- [39] Karsten Groekatthfer and Zizung Yoon. Introduction into quaternions for spacecraft attitude representation. *Technical University of Berlin: Department of Astronautics and Aeronautics*, pages 1–16, May 2012.
- [40] N. Guenard, T. Hamel, and V. Moreau. Dynamic modelling and control strategy for an x4-flyer. *International Conference on Control and Automation*, pages 141–146, June 2005.
- [41] Drone HiTech. Xrotor 20a esc. [http://dronehitech.com/wp-content/uploads/2016/04/IMG\\_0524.jpg](http://dronehitech.com/wp-content/uploads/2016/04/IMG_0524.jpg), 2016. [Accessed:2016-11-05].
- [42] HobbyKing. Orangerx rpm sensor. [http://www.hobbyking.com/hobbyking/store/\\_61511\\_Orange\\_RPM\\_Sensor.html](http://www.hobbyking.com/hobbyking/store/_61511_Orange_RPM_Sensor.html), 2016. [Accessed:2016-10-09].
- [43] HobbyKing. Rotorstar super mini s-bec. [http://www.hobbyking.com/hobbyking/store/\\_33987\\_RotorStar\\_Super\\_Mini\\_S\\_BEC\\_6S\\_10A.html](http://www.hobbyking.com/hobbyking/store/_33987_RotorStar_Super_Mini_S_BEC_6S_10A.html), 2016. [Accessed:2016-10-08].
- [44] HobbyKing. Signal converter module sbus-ppm-pwm. [http://www.hobbyking.com/hobbyking/store/\\_88384\\_Signal\\_Converter\\_Module\\_SBUS\\_PPM\\_PWM\\_S2PW\\_.html](http://www.hobbyking.com/hobbyking/store/_88384_Signal_Converter_Module_SBUS_PPM_PWM_S2PW_.html), 2016. [Accessed:2016-10-09].
- [45] HobbyKing.com. Hobby king: The ultimate hobby experience. <http://www.hobbyking.com/hobbyking/store/index.asp>, 2016. [Accessed:2016-06-12].
- [46] G. Hoffmann, H. Huang, S. Waslander, and C. Tomlin. Quadrotor helicopter flight dynamics and control: Theory and experiment. In *Guidance, Navigation and Control Conference and Exhibit*, pages 1–19, Hilton Head, South Carolina, 8 2010. American Institute of Aeronautics and Astronautics, American Institute of Aeronautics and Astronautics. Derivation of advanced aerodynamic affects on STARMAC Quadrotor Prototype.
- [47] InvenSense Inc. Mpu6050 6-axis gyroscope/accelerometer datasheet. Product Specification Data Sheet, 8 2013. Available From:[https://www.cdiweb.com/datasheets/invensense/MPU-6050\\_DataSheet\\_V3%204.pdf](https://www.cdiweb.com/datasheets/invensense/MPU-6050_DataSheet_V3%204.pdf).
- [48] Digi International. Xbee/xbee pro rf modules. Technical Data Sheet, 9 2009. Available From:<https://www.sparkfun.com/datasheets/Wireless/Zigbee/XBee-Datasheet.pdf>.

- [49] W. Jia, Z. Ming, Y. Zhiwei, and L. Bin. Adaptive back-stepping lpv control of satellite attitude maneuvers with sum of squares. In *World Congress on Intelligent Control and Automation*, volume 8, pages 1747–1752. IEEE, 7 2010.
- [50] Tor A. Johansen and Thor I. Fossen. Control allocation - a survey. *Automatica*, 45:10871103, 11 2012. Prepared for: Department of Engineering Cybernetics - Norwegian University of Science and Technology.
- [51] Tor A. Johansen, Thor I. Fossen, and Petter Tondel. Efficient optimal constraint control allocation via multi-parametric programming. White paper, Department of Engineering Cybernetics, Nowegian University of Science and Technology, N/A 2005.
- [52] Tor A. Johansen and Johannes Tjnns. Adaptive control allocation. White paper, Department of Engineering Cybernetics, Nowegian University of Science and Technology, N/A 2008.
- [53] S.M Joshi, A.G Keklar, and J.T Wen. Robust attitude stabilization of spacecraft using nonlinear feedback. *IEEE Transactions on Automatic Control*, pages 1800–1803, October 1995.
- [54] C. Karen Liu and S. Jain. Tutorial on multibody dynamics. Georgia Institute of Technology: Online Course Content, N/A, 10 2012. Available at: [http://www.cc.gatech.edu/~karenliu/Home\\_files/dynamics\\_1.pdf](http://www.cc.gatech.edu/~karenliu/Home_files/dynamics_1.pdf).
- [55] Farid Kendoul, Isabelle Fantoni, and Rogelio Lozano. Modeling and control of a small autonomous aircraft having two tilting rotors. *IEEE Conference on Decision and COntrol*, pages 8144–8149, December 2005.
- [56] A. Koshkouei, A. Zinober, and K. Burnham. Adaptive sliding mode backstepping control of nonlinear systems with unmatched uncertainty. *Asian Journal of Control*, pages 447–453, 12 2004.
- [57] P. Krishnamurthy and F. Khorrami. Adaptive backstepping and theta-d based controllers for a tilt-rotor aircraft. *Mediterranean Conference on Control and Automation*, pages 540–545, June 2011.
- [58] Raymond Kristiansen and Per J. Nicklasson. Satellite attitude control by quaternion-based backstepping. *American Control Coference*, N/A:907–912, 6 2005. Published by Department of Computer Science, Electrical Engineering and Space Technology; Narvik University College.
- [59] Jack B. Kuipers. *Quaternions and Rotation Sequences: A Primer with Application to Orbital Aerospace and Virtual Reality*, pages 127–143. Princeton University Press, September 2002. Used for Quaternion and Rotation Matrix reference.
- [60] Peter Lambert. Nakazawa, banton and jin, bai x. Technical Report N/A, Computer and Electrical Engineering: University of Victoria, Victoria, Canada, 12 2013.
- [61] Prof Allan J. Laub. The moore-penrose pseudo inverse. UCLA Math33A Course Content, UCLA, Los Angeles, 3 2008. Course Notes cited from <http://www.math.ucla.edu/~laub/33a.2.12s/mppseudoinverse.pdf>.
- [62] Jang-Ho Lee, Byoung-Mun Min, and Eung-Tai Kim. Autopilot design of tilt-rotor uav using particle swarm optimization method. *International COnference on Control, Automation and Systems*, pages 1629–1633, October 2007.
- [63] LibrePilot. Openpilot/librepilot wiki. Website: <http://opwiki.readthedocs.io/en/latest/index.html>, 5 2016. Information wiki page for LibrePilot/OpenPilot firmware.
- [64] Hyon Lim, Jaemann Park, Daewon Lee, and H.J. Kim. Build your own quadrotor. *IEEE ROBOTICS & AUTOMATION MAGAZINE*, pages 33–45, 9 2012. Publication on Opensource Autopilot systems.

- [65] C. Liu, B. Jiang, X. Song, and S. Zhang. Fault-tolerant control allocation for over-actuated discrete-time systems. *Journal of The Franklin Institute*, 352:2297–2313, 3 2015. Research output by Nanjing College of Automation Engineering, University of Aeronautics and Astronautics.
- [66] Kilowatt Classroom LLC. Vfd fundamentals. Report, Kilowatt Classroom LLC, 2 2003.
- [67] SteadiDrone PTY LTD. Steadidrone home. <http://www.steadidrone.com/>, 2016. [Accessed:2016-06-08].
- [68] Teppo Luukkonen. Modelling and control of a quadcopter. Master’s thesis, Aalto University: School of Science, Eepso, Finland, 8 2011. Independent research project in applied mathematics.
- [69] Tarek Madani and Abdelaziz Benallegue. Backstepping control for a quadrotor helicopter. *International Conference on Intelligent Robots and Systems*, pages 3255–3260, October 2006.
- [70] I. Mandre. Rigid body dynamics using euler’s equations, rungekutta and quaternions. Unpublished, 2 2006.
- [71] Carlos J. Mantas and Jose M. Puche. Artificial neural networks are zero-order tsk fuzzy systems. In *IEEE Transactions on Fuzzy Systems*, volume 16, pages 630–644, 6 2008.
- [72] Christopher G. Mayhew, Ricardo G. Sanfelice, and Andrew R. Teel. On quaternion based attitude control and the unwinding phenomenon. *American Control Conference*, pages 299–304, June 2011.
- [73] A. Megretski. Dynamics on nonlinear systems: Finding lyapunov functions. Technical report, Department of Electrical Engineering and Computer Sciences: Massachusetts Institute of Technology, 7 2003.
- [74] Ashfaq A. Mian and Wang Daoboo. Modelling and backstepping-based nonlinear control of a 6dof quadrotor helicopter. *Chinese Journal of Aeronautics*, 21:261–268, 3 2008. Simulated Backstepping Control.
- [75] Svein Rivli Napsholm. Prototype of a tiltrotor helicopter. Master’s thesis, Norwegian University of Science and Technology: Department of Engineering Cybernetics, Norway, 1 2013.
- [76] A. Nemati and M. Kumar. Modeling and control of a single axis tilting quadcopter. *American Control Conference*, pages 3077–3082, June 2014.
- [77] Kenzo Nonami, Farid Kendoul, Satoshi Suzuki, Wei Wang, and Daisuke Nakazawa. *Autonomous Flying Robots: Unmanned Aerial Vehicles and Micro Aerial Vehicles*, chapter 2, pages 44–48. Springer Japan, 1 edition, 2010. References to Cyclic-Pitch Control relevant subsections.
- [78] Kenzo Nonami, Farid Kendoul, Satoshi Suzuki, Wei Wang, and Daisuke Nakazawa. *Autonomous Flying Robots: Unmanned Aerial Vehicles and Micro Aerial Vehicles*, chapter 8, page 166. Springer Japan, 1 edition, 2010.
- [79] Gustavo P. Oliveira. Quadcopter civil applications. Master’s thesis, Informatics and Computer Engineering: University of Portugal, Portugal, 2 2014.
- [80] M. Oppenheimer, D. Doman, and M. Bolender. Control allocation for over-actuated systems. In *Mediterranean conference on Control and Automation*, volume 14, page 1, 6 2006.
- [81] OrangeRx. Orangerx r615x receiver. User Manual, 10 2014. Available From:<http://www.hobbyking.com/hobbyking/store/uploads/672761531X1606554X18.pdf>.
- [82] M. Orsag and S. Bogdan. Influence of forward and descent flight on quadrotor dynamics. Report, Department of Control and Computer Engineering, University of Zagreb, Croatia, 2 2012.

- [83] Christos Papachristos, Kostas Alexis, and Anthony Tzes. Design and experimental attitude control of an unmanned tilt-rotor aerial vehicle. *International Conference on Advanced Robotics*, pages 465–470, June 2011.
- [84] Parth N. Patel, Malav A. Patel, Rahul M. Faldu, and Yash R. Dave. Quadcopter for agricultural surveillance. In *Advance in Electronic and Electrical Engineering*, volume 3, India, 2013.
- [85] J. Peraire and S. Widnall. 3d rigid body dynamics: Euler angles. Lecture notes for Dynamics Course, 2009. Dynamics course notes, fall 2007.
- [86] J. Peraire and S. Widnall. 3d rigid body dynamics: The inertia tensor. Lecture notes for Dynamics Course, 2009. Dynamics course notes, fall 2007.
- [87] D. Peters. Eighth amendment of the civil aviation regulations. Goverment Gazette Notice, 5 2015. In Amendment to the Civil Aviation Act, 2009 (Act No.13 of 2009).
- [88] Jean-Baptiste Pomet and Laurent Praly. Adaptive nonlinear regulation: Estimation from the lyupanov equation. In *IEEE Transactions on Automatic Control*, volume 37, pages 729–740. IEEE, 6 1992.
- [89] P. Pounds, R. Mahony, P. Hynes, and J. Roberts. Design of a four-rotor aerial robot. *Australasian Conference on Robotics and Automation*, pages 145–150, November 2002.
- [90] Dmitry Prof. Garanin. Rotational motion of rigid bodies. Analytical Dynamics Course Notes, 11 2008. Content for City University of New York.
- [91] F. Ramponi and J. Lygeros. Lecture notes on linear system theory. Technical report, Department of Information Engineering, University of Brescia, 1 2015. Course Notes cited from: [http://home.mit.bme.hu/~virosztek/docs/mt\\_literature/LectureNotes.pdf](http://home.mit.bme.hu/~virosztek/docs/mt_literature/LectureNotes.pdf).
- [92] Beard Randal. Quadrotor dynamics and control. Report, Brigham Young University, 2 2008. Part of the Electrical and Computer Engineering Commons.
- [93] O. Rawashdeh, H.C. Yang, R. AbouSleiman, and B. Sababha. Microraptor: A low cost autonomous quadrotor system. *International Design Engineering Technical Conferences & Computers and Information in Engineering Conference*, pages 1–8, August 2009.
- [94] Anastasia Razinkove, Igor Gaponov, and Hyun-Chan Cho. Adaptive control over quadcopter uav under disturbances. *International Conference on Control, Automation and Systems*, pages 386–390, October 2014.
- [95] M.K. Rwigema. Propeller blade element momentum theory with vortex wake deflection. *International Congress of the Aeronautical Sciences, 27th*, pages 1–9, January 2010.
- [96] M. Ryll, H. Bulthoff, and P. Robuffo Giordano. Modelling and control of a quadrotor uav with tilting propellers. *IEEE International Conference on Robotics and Automation*, pages 4606–4613, May 2012.
- [97] M. Ryll, H. Bulthoff, and P. Robuffo Giordano. First flight tests of a quadrotor uav with tilting propellers. *IEEE International Conference on Robotics and Automation*, pages 295–302, May 2013.
- [98] A. Sanchez, J. Escareo, O. Garcia, and R. Lozano. Autonomous hovering of a noncyclic tiltrotor uav: Modeling, control and implementation. *The International Federation of Automatic Control*, pages 803–808, July 2008.
- [99] J. Seddon. *Basic Helicopter Aerodynamics*, chapter 2-5, pages 4–66. BSP Professional Books, 1 edition, 1990.

- [100] K. Shoemake. Quaternions. Siggraph course lecture notes, Department of Computer and Information Science; University of Pennsylvania, N/A 1987.
- [101] Puneet Singla, Daniele Mortari, and John L. Junkins. How to avoid singularity when using euler angles? *Advances in the Astronautical Sciences*, pages 1409–1426, January 2005.
- [102] G. Slabaugh. Computing euler angles from a rotation matrix. Lecture notes, City University, London, 5 1999.
- [103] Measurement Speacialties. Ms5611 barometric pressure sensor. Technical Data Sheet, 10 2012. Available From:[http://www.amsys.info/sheets/amsys.en.ms5611\\_01ba03.pdf](http://www.amsys.info/sheets/amsys.en.ms5611_01ba03.pdf).
- [104] STMicroElectronics. St-link/v2 in circuit debugger/programmer for stm32.
- [105] STMicroElectronics. Rm0316 reference manual. Online Micro-Controller Reference Manual, 3 2016. Available From:[http://www.st.com/content/st\\_com/en/products/microcontrollers/stm32-32-bit-arm-cortex-mcus/stm32f3-series/stm32f303.html?querycriteria=productId=LN1531](http://www.st.com/content/st_com/en/products/microcontrollers/stm32-32-bit-arm-cortex-mcus/stm32f3-series/stm32f303.html?querycriteria=productId=LN1531).
- [106] Prof S. Tavoularis. Reynolds transportation theorem. Course Notes on MCG3350 - Fluid Mechanics 1, 2008. Fluid Mechanics notes, fall 2008, [http://web.mit.edu/1.63/www/Lec-notes/chap1\\_basics/1-3trans-thm.pdf](http://web.mit.edu/1.63/www/Lec-notes/chap1_basics/1-3trans-thm.pdf).
- [107] Abdelhamid Tayebi and Stephen McGilvray. Attitude stabilization of a vtol quadrotor aircraft. *IEEE Transactions on Control Systems Technology*, pages 562–571, May 2006.
- [108] B. Theys, G. Dimitriadis, P. Hendrick, and J. De Schutter. Influence of propeller configuration on propulsion system efficiency of multi-rotor unmanned aerial vehicles. In *International Conference on Unmanned Aircraft Systems*, pages 195–201, Arlington, Virginia, 6 2016. IEEE, IEEE 2016.
- [109] Stephen T. Thornton and Jerry B. Marion. *Classical Dynamics of Particles and Systems*, chapter 7, pages 228–289. Thompson Brooks/Cole, 5 edition, 2003.
- [110] John Ting-Yung Wen and Kenneth Kreutz-Delgado. The attitude control problem. *IEEE Transactions on Automatic Control*, pages 1148–1162, October 1991.
- [111] David Tong. Lagrange formalism. Lectures of Classic Dynamics, Course Notes, 2005. Classical Mechanics Notes.
- [112] P. Tsotras, M. Corless, and J.m Longuski. A novel approach to the attitude control of axisymmetric spacecraft. *Automatica*, 31:1099–1112, 3 1995. Control Automatica, Printed in Great Britan.
- [113] Ultimaker. Ultimaker v2+ product page. <https://ultimaker.com/en/products/ultimaker-2-plus#volume>, 2016. [Accessed:2016-9-11].
- [114] E. van Kampen and M. M. van Paassen. Ae4301: Automatic flight control system design. Delft Centre for Systems and Control; MSc Notes, 1 2008. Course Notes cited from: <http://aerostudents.com/master/advancedFlightControl.php>.
- [115] Ronny Votel and Doug Sinclair. Comparison of control moment gyros and reaction wheels for small earth-observing satellites. In *Conference on Small Satellites*, volume 26, pages 1–7. Utah State University, 8 2012. Open access on AIAA conference website.
- [116] Tao Wang, Tao Zhao, Du Hao, and Mingxi Wang. Transformable aerial vehicle, 09 2014.
- [117] A. Witkin and D. Baraff. Physically based modeling: Principles and practice. CMU: Online Siggraph Course notes, N/A, 9 1997. Course Notes cited from <http://www.cs.cmu.edu/~baraff/sigcourse/>.

- [118] X. Xiaozhu, L. Zaozhen, and C. Weining. Intelligent adaptive backstepping controller design based on the adaptive particle swarm optimization. *Chinese Control and Decision Conference*, pages 13–17, September 2009.
- [119] Song Xin and Zou Zaojian. A fuzzy sliding mode controller with adaptive disturance approximation for an underwater robot. In *International Asia Conference on Informatics in Control, Automation and Robotics*, volume 2, pages 50–53, 10 2010.